Simulations of Lock and Key Colloids

Law, Clement

Award date:
2015

Awarding institution:
University of Bath

Simulations of Lock and Key Colloids

Clement Law

A thesis submitted for the degree of
Doctor of Philosophy

University of Bath
Department of Physics
November 2014

Dedication

I dedicate this thesis to my Lord and Saviour, who also brought my wonderful wife into my life.

"For the foolishness of God is wiser than human wisdom, and the weakness of God is stronger than human strength."

1 Corinthians 1:25

Acknowledgements

Firstly, to my God without whom I would have nothing.

This work is the culmination of a large fraction of my academic and personal life. It would not have been possible without the patience of many people. Thanks to Rob Jack and Nigel Wilding for putting up with my sometimes naive questions and being generally supportive, whatever time of day or night. In alphabetical order, thanks to Douglas Ashton, Ryan Curtis, Chris Fullerton, James Grant, Ian Thompson, Rhys Wheater, Ying Wu. Thanks to my family and friends (you know who you are), and my amazing wife. Thanks also extend to the University of Bath for providing the full funding for these three years.

This whole experience has been completely formative, and I am indebted to you all.

Contents

List of Figures

Declaration

No portion of the work referred to in this thesis has been submitted in support of an application for another degree or qualification of this or any other university or other institution of learning. Where the work of others has been reproduced it is clearly stated and references provided.

Abstract

We introduce the concept of self-assembly and describe how it can explored with a system of colloids. We introduce the lock and key colloid, and describe how it can be useful probe for exploring a specific, geometry-centric, type of colloidal self-assembly called the depletion interaction.

We illustrate some of the problems with simulating the lock and key colloid, and introduce a novel simulation method to side-step many of these problems.

Using this simulation technique, and derived theoretical thermodynamic apparatus, we show a methodology for parametrising the depletion drive self-assembly of colloids. This parametrisation allows us to avoid explicitly modelling the nanoparticles that mediate depletion-driven self-assembly and thereby speeds up any subsequent simulations by an order of magnitude compared to the novel simulation technique. Using our parametrisation, we repeat some measurements of explicitly modelled lock and key simulations and find good agreement.

As a small aside, we also simulate a sedimenting, lock-only system in the same spirit as a published work. In this work, the authors find an interesting decrystallisation over time from a solid to liquid-like phase. We do not observe this in our experiment but instead note that we can induce a liquid-solid phase transition by varying the depth of the lock mouth.

To end, we discuss the quality of our findings and what future avenues of work they may lead to.

Chapter 1

Introduction

In this chapter, we discuss the general idea of self-assembly and how it underpins many disparate things in the world. We then show how its nature can be better understood through the use of a class of particles called colloids. We explain that lock and key particles belong to this class of particle, and how it is a good candidate to explore a type of self-assembly interaction called the 'depletion interaction'.

1.1 Self-assembly

The concept of self-assembly underpins many disparate things in life. It is the idea that a disordered system can, through simple interacting local rules coalesce into an organised structure. We can view the creation of a baby in a mother's womb as a long reaching result of the simple interactions between DNA base pairs. On a grander scale, we can view galaxies as self-assemblies of stars, and the stars as self-assemblies of their constituent atoms, which are themselves a self-assembly of protons, neutrons and electrons.

In the hands of human-kind, one could employ the idea of self-assembly to create materials and devices of desired function and purpose. Indeed, this is what has recently been investigated, with the creation of photonic crystals with a designated band gap [2]. The power of this idea can perhaps be grasped if we consider the intricate, involved, multi-step process of *two-dimensional* CPU manufacture [3] which, some would say, is the antithesis of self-assembly [4]. Additionally, with the commercial pressure of matching Moore's Law[1] there has been an increasing drive towards *three-dimensional circuitry* [5]. Classic, top-down human fabrication therefore becomes increasingly difficult. However, there has been process in this area of self-assembled integrated circuitry too, with self-assembled three-dimensional circuitry [6].

Simply put, the better we understand the mechanisms of self-assembly, the more able we are to tune and design constituent components to create desired materials and devices.

[1] Moore's Law is an *empirical* observation that "the level of chip complexity that can be manufactured for minimal cost is an exponential function [...] of time [and that the] minimal cost of manufacturing a chip is decreasing [at an] inversely proportional rate [to the] number of components" [5, p. 12]

1.2 Colloids as a Model for Self-Assembly

A good way of elucidating the nature of self-assembly is through the sub-field of colloidal self-assembly. In order to discuss this, we must first define what a colloid is. We will then discuss a way of classifying their interactions by consideration of some basic physical principles. In contrast to this, we will also show how the development of exotically shaped colloids proceeds hand-in-hand with studies of self-assembly. Finally, we will show that the lock and key colloidal is a relatively simple example of anisotropic colloidal self-assembly.

We can define a particle as a colloid if it has visible Brownian motion. For a particle's motion to be defined as Brownian and visible[2], we set the criterion that a particle's sedimentation length - a ratio between the thermal energy imparted to and the gravitational force due to the particle -

$$l = \frac{k_{\mathrm{B}}T}{mg}, \tag{1.1}$$

should be larger than its radius.

A simple calculation illustrates the size of a colloid: shop-bought milk from the United Kingdom has a density of 1030 kg/m^3 of which approximately 13% is composed of buttermilk colloids, suspended in water [7, p. 438]. Hence, assuming our buttermilk colloids are approximately spheres, we can equate its mass to the volume times the buttermilk density. If we also allow the sedimentation length to be roughly the radius of the colloid, at room temperature of 300 K, the radius of the buttermilk colloid should be $\sim$2 μm. This back-of-the-envelope calculation is in line with the standard definition of colloid as a particle roughly in the range of nm and μm [8, p. 295]. The term colloid is often used as a synonym for a colloid suspended in a fluid [9, pp. 192-193].

We now go on to categorise colloids in two different ways, before showing that the lock and key colloid is a good candidate for exploring one type of self-assembly.

[2]Typically, we refer to 'visible' colloids as visible to confocal microscopy

1.2.1 Electrostatic Interaction

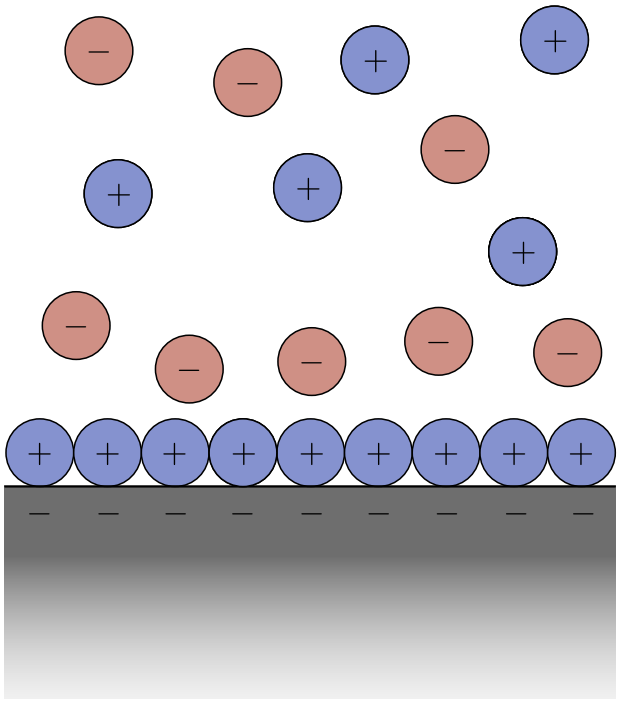

Figure 1.1: The double layer effect due to the electrostatic interaction. Here a negatively charged colloid is immersed in a fluid of ions. The surface of our colloid is negatively charged, leading to a build up of positively charged ions on its surface, which in turns leads up to a further build up of negatively charged ions. This is, then, the origin of the term *double layer*, where there is a double layer of oppositely charged ions.

If a colloid is somehow charged, through the embedding of positive or negative ions into its surface or otherwise, and subsequently suspended in an aqueous solution of disassociated ions, a phenomenon known as the double layer effect occurs (fig. 1.1). This effect is mediated by the electrostatic interaction. A layer of oppositely charged ions are attracted to the surface of the colloid. The aqueous solution between any two of these colloids will therefore have a different charge density to the bulk fluid, leading to a charge imbalance and the development of a repulsive, osmotic pressure. The electrostatic interaction, through the manifestation of the double layer effect is principally responsible for the acid-activated coagulation of buttermilk colloids in milk. Specifically, milk does not coagulate naturally to butter due to a layer of charged ion around every buttermilk colloid. The introduction of dissociated acid ions neutralises the ions in the aqueous solution, leading to the self-assembly of butter [10, p. 50].

1.2.2 Van der Waals Interaction

Any colloid suspended in a fluid will also experience van der Waals interactions, due to the cooperative oscillation of electron clouds around every molecule that make up the colloidal particle. Any instantaneous fluctuation of an electron cloud will then attract or repel any nearby electron cloud, leading to collective attractive and repulsive behaviour of entire colloids. Together with electrostatic interactions, a more accurate description of

interacting colloidal suspensions is given by DLVO theory - so named after Derjaguin and Landau [11] and Verwey and Overbeek [12].

We have in mind that the electrostatic interaction is very short-ranged[3] that the colloid is suspended in - so for future discussion, we are going to neglect both these forces and assume that the colloids act as hard particles.

1.2.3 Depletion Interaction

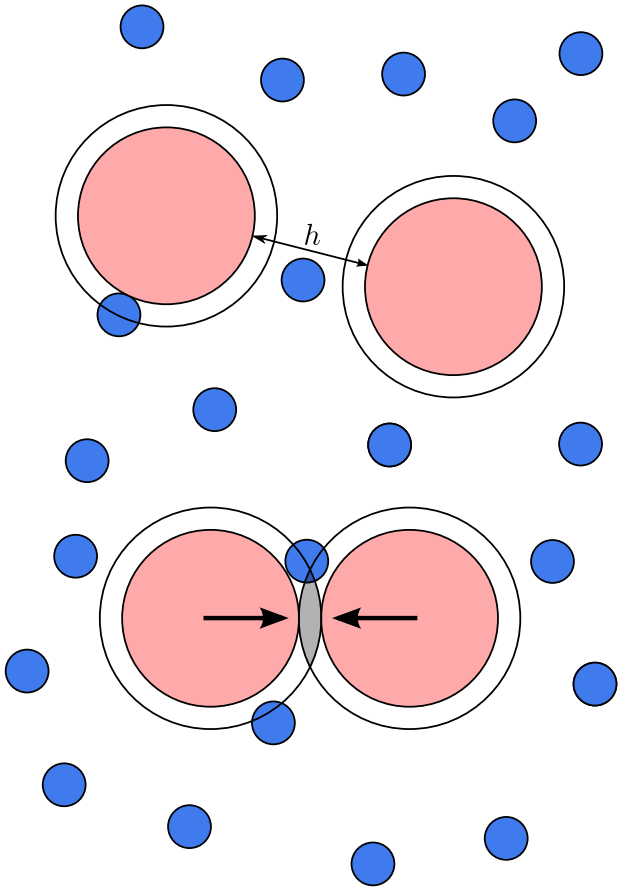

Figure 1.2: Demonstration of the depletion interaction between spheres. The two lower spheres being closer together than the radius of a nanoparticle leads to an osmotic pressure that forces them together. This is known as the depletion interaction. The lines drawn around the colloids indicate the regions forbidden to a colloid, i.e., their exclusion volumes. The shaded region between the two lower colloids is then the *difference* in exclusion volumes, ΔV, and can be described as the volume excluded from the *centre* of a nanoparticle for two close spherical colloids. With foresight, we also define h to be the distance of closest approach between two spheres. For two spheres, this will always lie on the line joining the centre of the two spheres.

The results in this work are relevant for colloids interacting by depletion forces. As well as immersion in a solution, colloids can also be present with nanoparticles, named as such because they are generally on the order of a nanometre in size. Importantly, they *do not* adsorb either to each other or to the larger colloids themselves. This is sometimes termed the 'hard particle criterion'. The depletion interaction can be described succinctly

[3]This is due to electrostatic screening. For example, the salt added to the fluid dissociates into charged ions that screen out long ranged electrostatic interactions.

with thermodynamic vocabulary as a colloidal and nanoparticle suspension seeking to minimise its Gibbs free energy by maximising its entropy. This competition gives rise to the surprising phenomenon of depletion mediated self-assembly, whereby clusters of colloids are preferred to isolated colloids. Despite the loss of entropy due to isolated colloids, the gain in entropy to the suspension, and thereby the whole closed system, is greater. Viewed from another angle, when two or more colloids are closer than the radius of a nanoparticle in the suspension, an osmotic pressure - due to local imbalanced nanoparticle concentrations - pushes the colloids together (fig. 1.2). For two hard spheres suspended in a solution of smaller (nanoparticle) spheres of radius δ, the depletion potential is written as [13]

$$W_{\mathrm{d}}(h) = \begin{cases} \infty & h < 0 \\ -P\Delta V_{\mathrm{hs}} & 0 \leq h \leq 2\delta \\ 0 & h \geq 2\delta \end{cases} \tag{1.2}$$

where P is the (ideal gas) osmotic pressure, h is the distance from the closest point of the two spheres (see fig. 1.2). The region of forbidden approach for nanoparticles is demonstrated by the lines drawn around the colloids in fig. 1.2. The *difference* in *exclusion* volumes for two spheres is represented as ΔV. For two close together colloidal spheres ($0 \leq h \leq 2\delta$ regime), ΔV resembles the volume formed from the intersection of two overlapping spheres situated at the centres of the two colloids. For $h = 0$, these spheres are of radius $R + \delta$. As h increases to 2δ, this ΔV shrinks to a point as the overlap intersection decreases. Equation (1.2) shows that the depletion potential between two spherical colloids, in the range of the diameter of a nanoparticle, depends only on the ideal gas osmotic pressure and the excluded volume. Later on, we will find that this relation is approximately true for a lock and key colloid, save that the excluded volume is different (and larger) than the lock and key, such the depletion potential is greater.

1.2.4 Anisotropic Colloids

One can also classify colloids in terms of various measures of anisotropy [14, 15]. Glotzer and Solomon [14] give one such classification, where they have chosen some general properties of anisotropic particles (fig. 1.3). The anisotropic properties of these particles mean that they have a tendency to self-assemble, via one or more of the mechanisms mentioned in the previous section. Choosing just two categories, we have 1. *branched* colloids such as octapod colloids that form hexagonal 'ballerina networks' [16] or gold tetrapod nanocrystals [17], 2. *faceted polyhedra* such as silver cubes that self-assemble into close-packed 2D arrays [18] or polymer triangular prisms [19].

A 'patchy' particle is a subset of the 'patterned' colloid criteria in fig. 1.3. Patchy particles [20] can be spheres (though rods also exist) that interact through patches on a typically symmetrical geometry. The mechanisms by which these patchy particles interact varies greatly. They include DNA-mediated 'patches' [21, 22] or hydrophobic-hydrophobic attraction [23] ('Janus' spheres [24, 25]). With DNA base pair interactions one can tune

for a specific lattice or structure. With hydrophobic interactions, one congregates colloids by exploiting their adversity to water.

Patchy particles have been used as a simpler model to study more complicated phenomena. Two examples include the glass forming nature of the vitrimer polymer [26] and the mapping of tetrahedral patches to silicon and liquid water [27]. There is an arguably larger body of work that studies patchy colloids on their own merit. Some examples include the optimisation of monodisperse self-assembling icosahedral structures [28], novel Monte Carlo simulation affirmations of candidate patchy particle structures [29] and design guidelines for constructing Archimedean tilings [30].

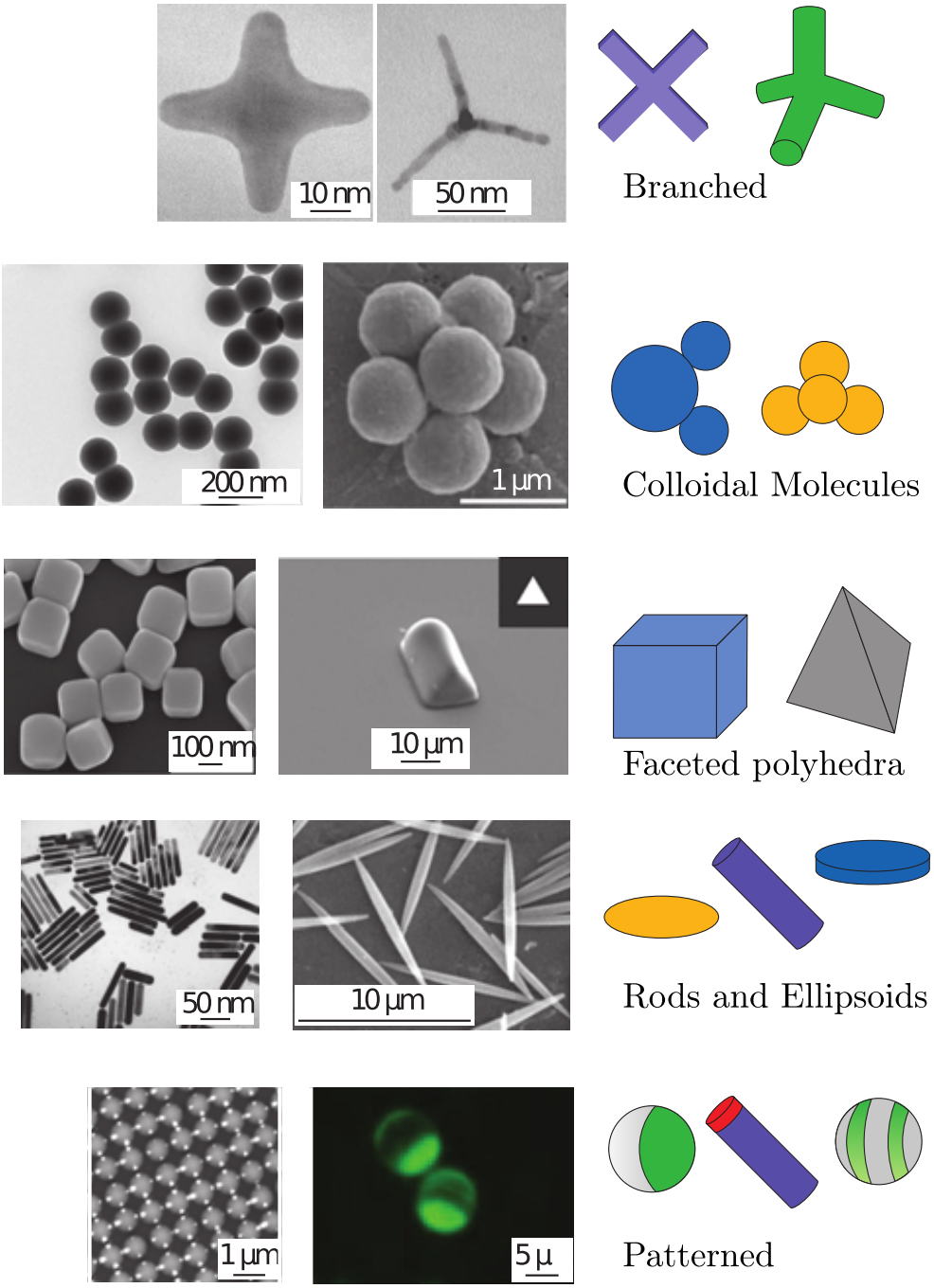

Figure 1.3: Adapted from [14]. Demonstrating a wide variety of anisotropic colloids. Their anisotropy gives them a tendency towards self-assembled clusters. From top to bottom, left to right, we have: *branched particles*, examples of which are gold [17] and CdTe tetrapods [31], *colloidal molecules* such as silica dumb-bells [32] and fused clusters [33], *faceted polyhedra* such as silver cubes [18] and polymer triangular prisms [19], *rod-like and ellipsoidal* particles made of gold [34] and polymer latex [35], and *patterned* particles such as spheres with valence-enabled 'patchiness' [36] and Janus spheres [37].

1.2.5 Lock and Keys & the Depletion Interaction

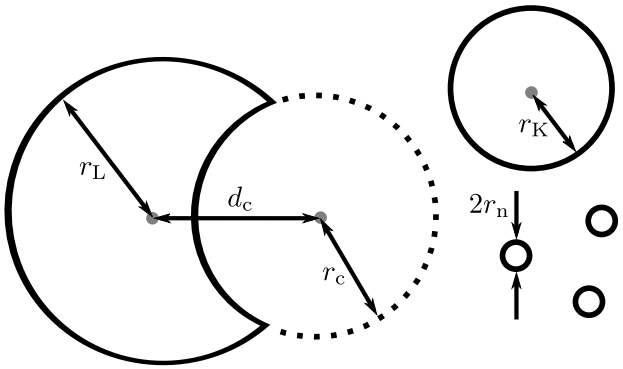

Figure 1.4: Important geometrical parameters of the lock and key and nanoparticle. r_{K} and r_{n} are the radii of a key and nanoparticle, whilst r_{L} is the radii of a lock if it were a complete sphere. r_{c} describes the radius of a sphere a distance d_{c} away from the centre of a lock. Taken together, r_{L}, r_{c} and d_{c} completely describe the geometry of a lock. In this thesis, we typically match r_{K} to r_{L}, $r_{\mathrm{n}} = {}^{r_{\mathrm{L}}}/_{10}$, and finally set $r_{\mathrm{L}} = {}^{1}/_{2}$.

Having discussed the importance of understanding self-assembly and how it can be studied with (anisotropic) colloids, we go on to define the anisotropic lock and key colloid and how it is a useful, relatively simple, tool to study depletion-mediated self-assembly.

A lock is a spherical colloid with a spherical indentation into which a spherical key colloid (key) can fit (fig. 1.4). As mentioned previously, for depletion mediated self-assembly to occur nanoparticles must be present in the fluid suspension of lock and keys. In experiments, to ensure that a lock and key particle obey the hard particle criterion, hydrophilic polymers are grafted on to the surface such that there is a "short range, nearly hard-sphere [...] repulsion" [38].

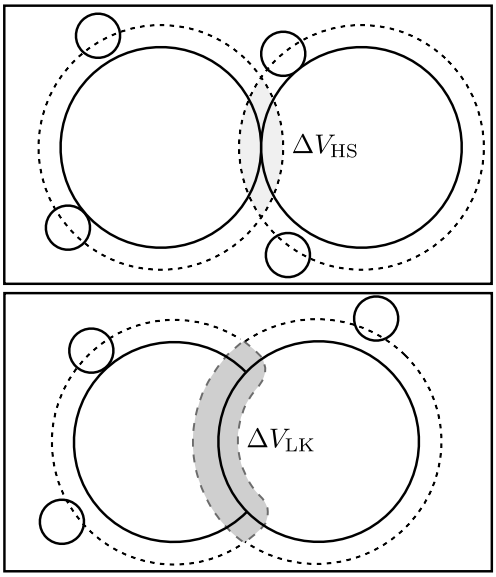

Figure 1.5: This two-dimensional representation of a lock and key colloid in a box of volume V shows that the *difference* in exclusion volumes of a lock and key colloid, ΔV_{LK} is *greater than* that of two hard spheres, ΔV_{HS} in the same size box. We emphasise that the exclusion volume is the volume inaccessible to the centres of the nanoparticles, such that there is an osmotic pressure that forces the two larger particles together. If the exclusion volume is bigger for a lock and key, then the osmotic pressure is greater and so the depletion potential and the connected self-assembly phenomena are enhanced.

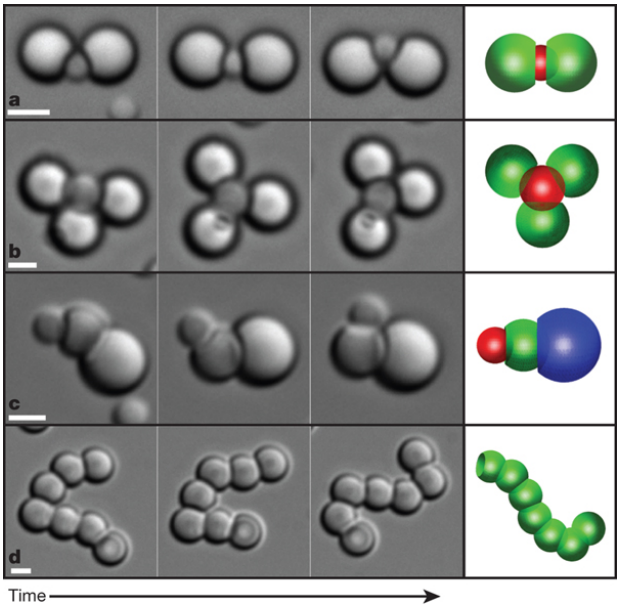

Figure 1.6: Reproduced from the work of Sacanna et al. [38]. Time-lapse (forward in time from left to right) optical microscopy images of different structures that are possible through depletion mediated lock and key self-assembly. These locks and keys have been confined to two dimensions on an optical slide. Each scale bar is 2μm.

A lock and key colloid can self-assemble into 'caterpillar' (fig. 1.7), 'snowman' and 'flower'-like aggregates (fig. 1.6). This self-assembly is mediated by the depletion interaction in the same manner as hard spheres, but, importantly, the volume excluded from nanoparticles due to a key bound to a lock's 'mouth', ΔV_{LK}, is greater than that of two spheres, ΔV_{HS} (eq. (1.2)). This comparison can be visualised in fig. 1.5. Therefore the

associated depletion potential is greater for a lock and key colloid and so the self-assembly characteristics are naturally enhanced. From now on, for brevity, ΔV refers to ΔV_{LK}.

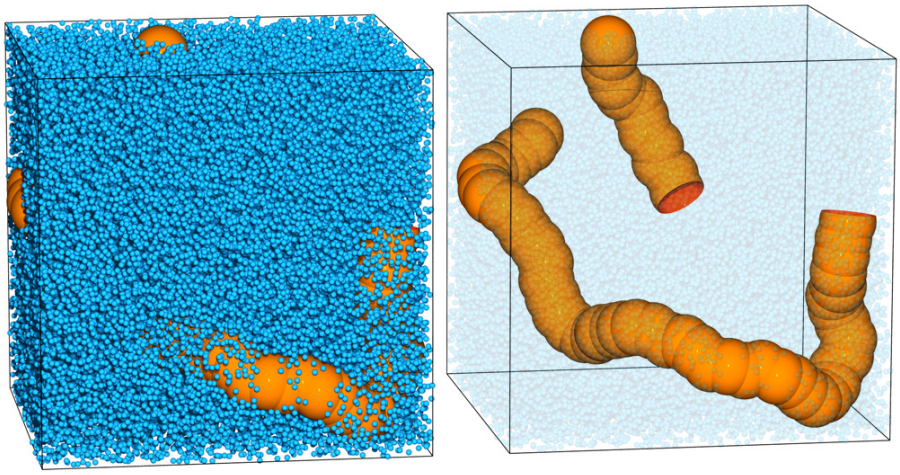

Figure 1.7: Reproduced with permission from [1]. This figure demonstrates one of the possible computer simulated lock-lock structures produced from a system of locks with hard sphere nanoparticles. The LHS is a good visual cue as to the population of nanoparticles required for self-assembly, and the RHS has the same nanoparticles faded out to highlight the two lock-lock chains that span the whole system.

The exact nature of the lock and key depletion potential is more complicated than the hard sphere case. There have been several attempts to elucidate the depletion potential. The first instance was through the use of (statistical mechanical) density functional theory (DFT). DFT methods use the idea that one can somehow approximate the intrinsic Helmholtz free energy functional of a classic fluid - in this case of the lock and key and nanoparticles - from which one takes derivatives to obtain the microscopic structure [39]. This is possible as the Helmholtz free energy depends on the density of the fluid. Roth et al. [40] in 1999 used DFT to calculate the depletion potential due to hard nanoparticles between a *curved* wall and a spherical particle. They performed this calculation to provide a theoretical grounding to the work of Dinsmore et al. who observed that a large colloid, immersed in a sea of smaller colloids and trapped in a lipid vesicle, preferred the curved regions of the vesicle walls [41]. This is reasonable as the particle will prefer a position where - in the language of the depletion interaction - the exclusion volume is greatest.

The work of Dinsmore et al. [41] and Roth et al. [40] pre-dates the seminal work of Sacanna et al. [38] - the ancestor of this thesis - in which Sacanna et al. demonstrate for the first time that a lock and key colloid exhibits real time self-assembly (fig. 1.6). Prior to their work, we see that Kinoshita and Oguni [42] employed the hypernetted-chain (HNC) equations solved on a discrete three-dimensional grid to calculate the depletion potential due to hard particles between what is essentially a colloidal key and a lock with a cubic, rather than a spherical, body [42]. This study is important because it is the first to explicitly mention the lock and key by name. HNC theory is a method that lets one determine the density profile of a classic hard fluid (see, e.g., [43] and [44, p. 89]), from which one can calculate the depletion interaction between a lock and a key. Nine years after Roth et al. [40], König et al. also used DFT to produce a depletion potential of a lock

and key system. Again, their lock is not spherical, but with more sophisticated techniques and collaboration with Kinoshita and Oguni [42], they are able to study an ellipsoidal key and its preferred docking motion to a lock. In context of their work, the spherical lock and key is a subset.

Importantly, the first explicit Monte Carlo simulation study on the lock and key colloid was performed by Odriozola et al. [46], two years before Sacanna et al. [38]. These authors were also able to calculate for the first time the two-dimensional depletion interaction between a lock and key. A major proportion of this thesis is to parametrise this two-dimensional depletion interaction. We highlight, also, the recent work by Ashton et al. [1] in which they simulated the "polymerisation" of a lock and nanoparticle only colloid into chains and offered a good theoretical description of this chaining phenomenology. We point to fig. 1.7 for a good example of the chaining they observed. Looking forward, this thesis ultimately hopes to produce self-assembled aggregates from a simplified interaction between lock and key colloids.

We have seen, therefore, that the inception of the lock and key colloid can be traced to as far back as a curved lipid vesicle moderated depletion. From this, there have been numerous, increasingly complicated attempts at theoretically describing the depletion potential of systems that look similar to the lock and key. The first completely Monte Carlo based simulation was only performed in 2008, two years before the self-assembly of lock and key colloids was shown in experiment by Sacanna et al.. We note that all attempts to calculate the depletion potential of a lock and key colloid - barring explicit simulation - have been good *analytical* approximations. This thesis will present some depletion potentials generated from novel Monte Carlo simulation techniques that are able to rapidly produce lock and key configurations that are distributed in a thermally equilibrated way. As such, given a long enough time period, one can be fairly confident that the depletion potentials generated are a good representation of a real lock and key colloid.

The lock and key colloid and its models are a good probe to use for the exploration of depletion-moderated self-assembly. This is because - as will be seen - the locks and keys synthesized in a laboratory are to a good approximation hard. To reiterate, 'hard' particles do not overlap or chemically adsorb each other. There also exist effective methods, one of which we use in this thesis, to simulate large size-asymmetric lock and key systems. Therefore, due to the good match between reality and theoretic models, a simulationist can work hand-in-hand with an experimentalist, informing each other of promising regimes for lock and key study. More generally, as the lock and key demonstrate a stronger self-assembly characteristic than hard spheres, we can use them to explore some more general questions. An example of such a question could be: what conditions are needed for optimal self-assembly [47–53]? Furthermore, we could explore whether a lock and key are actually the best matching shapes for depletion-mediated self-assembly or whether there exists a 'better' set of shapes.

Our work takes the first step in enabling the answer for such questions by parametrising the depletion potential between a lock and key colloid. The general idea is to simplify the depletion mediated self-assembly in a lock and key colloid. The most important step in

this process is to avoid the simulation of the nanoparticles themselves but to *preserve* their influence.

Lock and Key Synthesis Methods

What follows now is a summary of the main methods of synthesising lock and key shaped colloids.

The actual creation of locks in the laboratory, due to Sacanna et al. [38], post-dates their earliest mention in models - Kinoshita and Oguni [42] - by eight years. They were first created by nucleating monodisperse silicon oil droplets. These oil droplets were then consistently deformed to produce lock-like shapes. Depending on the type of oil used to form these droplets, different surface morphologies were created. The use of 3-methacryloxypropyltrimethoxysilane (TPM) as the nucleating oil produced the closest match to theoretical descriptions of locks fig. 1.4 in terms of sharp, well defined edges. Using 3- (methacryloxypropyl)methyldimethoxy silane (DPM) formed structures similar to the 'colloidal rocks' studied by Zhang [54]. A year later, Datta et al. published a study on exploiting large shell asymmetry in a spherical capsule of oil to induce buckling into a lock-like shape. In the same year, Ma et al. [56] released the details of a novel micro-fluidic method to create locks.

1.3 Outline of Thesis

In this thesis, the lock and key colloid is treated both theoretically and simulated in a computer.

Chapter 2 introduces the novel simulation method used to model the self-assembly of lock and keys. Chapter 3 develops the mathematical framework needed to make various predictions about a lock and key colloid, firstly from a single lock and a single key, and then to the more complicated two lock system. We present evidence of a successful parametrisation of the one lock-key and two lock system in chapter 4. As an interesting aside, we study sedimenting locks (with no nanoparticles) as a simulation analogue of Ivell et al. [57] in chapter 6. Finally, we provide concluding remarks and suggest further lines of work in chapter 7.

Chapter 2

Simulation Methods

In order to parametrise the lock and key effective potential, we will need some method to generate sufficient data to produce correlation functions that are correctly equilibrated. This is important because without sufficient data, the error bars on any interpolations or extrapolations of unexplored parametrisation will be too large. We are interested in equilibrium correlation functions which demonstrate how a typical two lock or lock and key colloid are distributed. Later on, we will discover that adequate correlation functions to this purpose will be at least three-dimensional and provide a method to systematically deal with this. These correlation functions will turn out to be crucial to producing a parametrised potential.

To calculate equilibrium correlation functions, one might use a conventional Monte Carlo simulation in which one proposes small displacements and rotations of the colloids and nanoparticles and accepts/rejects with a Metropolis criterion (see, e.g., [58, 59]). Given sufficient simulation time, this guarantees accurate estimates. At the nanoparticle densities sufficient to observe depletion-mediated self-assembly, one problem is 'caging' whereby a colloid is *trapped* by a cage of nanoparticles for long times such that the algorithm is unable to produce equilibrium correlation functions for practical simulation time scales (on the order of, at the most, days).

The effective simulation of the lock and key colloid requires a more sophisticated technique than the conventional, small move, Monte Carlo. We stress that this new technique - the geometric cluster algorithm or GCA - like its original ancestor, produces a Boltzmann distribution of system configurations by satisfying detailed balance. We begin by presenting the impetus that drove the development of novel Monte Carlo schemes like the GCA, before describing the move sets needed to satisfy ergodicity for spheres and anisotropic particles.

2.1 Geometric Cluster Algorithm

2.1.1 History

In 1995, Dress and Krauth developed a novel cluster algorithm [60] in response to the long ongoing difficulty of thermally equilibrating hard-sphere liquids with computer simulation

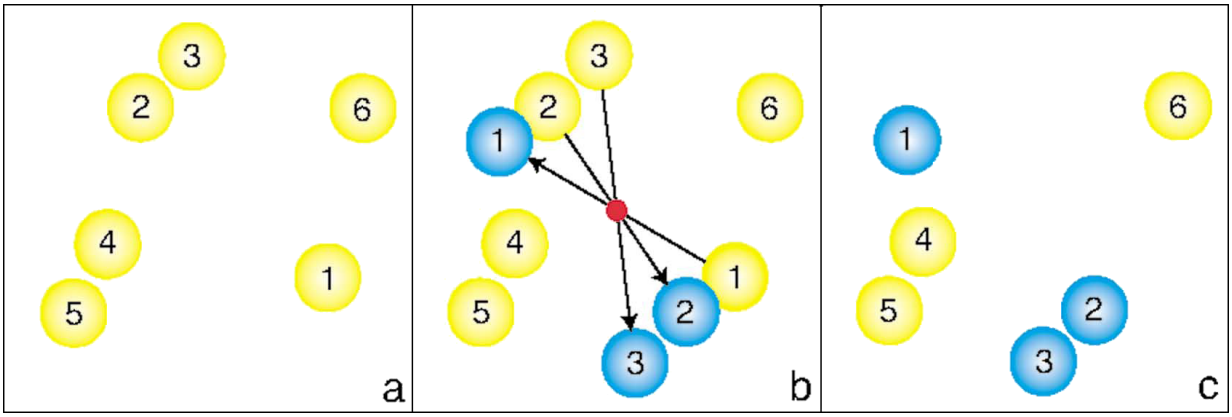

Figure 2.1: Reproduced from [62]. A two dimensional illustration of the GCA. The small circle is a randomly chosen pivot point upon which our larger circles (or colloids) translate through. The lighter coloured particles represent colloids in their original position. Some of the lighter coloured particles in a) are chosen to reflect through the pivot point in b), leading to a distinctly different configuration in c).

(a problem documented from at least as far back as 1957 by Alder and Wainwright [61]). The basic idea of their algorithm is to randomly choose points in a hard-sphere liquid around which the entire system is rotated a random amount. Particles (if any) that overlap between the new system and the old system are exchanged, the end result of which is to achieve dissimilar configurations of hard spheres whose occurrence upon successive applications of the algorithm samples the Boltzmann distribution. In 2004, Liu and Luijten proposed the geometric cluster algorithm (GCA) [62] - 'the first general rejection-free cluster algorithm for off-lattice systems' - a spiritual child of Dress and Krauth's novel off-lattice cluster algorithm and Wolff's improvement [63] of Swendsen and Wang's cluster updating lattice algorithm [64]. Liu and Luijten went on to propose two methods to generalise the GCA for anisotropic particles [66]. The first method used hyperspherical boundary conditions in order to keep the rejection-free aspect of the GCA intact (i.e., every cluster identified is always point translated). The second method sacrificed some identified clusters, but allowed standard periodic boundary conditions to be used. This thesis uses the second method, as expounded by Ashton et al. to simulate the lock and key colloid system [1].

2.1.2 Description of GCA for Spheres

The GCA is a method, applicable to a system of particles with arbitrary potential, that allows the rapid sampling of configuration space through coordinated updates of large groups, or clusters, of said particles. For a system of spheres, the GCA moveset proposed by Liu and Luijten proceeds as follows. A random particle is point reflected through a random pivot point. Keeping the same notation as Liu and Luijten [62], a more general description for spheres with a pair potential, $V(r)$, can be described as follows. A random sphere i at position $\boldsymbol{r}_i$ is point reflected through a random pivot point to a new position, $\boldsymbol{r}_i'$. After the point reflection, we can then identify two categories of spheres: a) spheres that interact with i in its new position, $\boldsymbol{r}_i'$ and b) spheres that have interacted with i in

its original position, $\boldsymbol{r}_i$. We label spheres in both categories j. These spheres, j, are either left in their original positions or reflected through the same point pivot. The probability that they are reflected is

$$p_{ij} = \max\left[1 - \exp\left(-\beta\Delta_{ij}\right), 0\right] \tag{2.1}$$

where

$$\Delta_{ij} = V(|\boldsymbol{r}_i' - \boldsymbol{r}_j|) - V(|\boldsymbol{r}_i - \boldsymbol{r}_j|) \tag{2.2}$$

and $\beta = 1/k_{\mathrm{B}}T$. In other words, the cluster addition probability depends only on the relative distances between the point reflected sphere i and j. If sphere j has been moved, all its interactive neighbours are considered for inclusion too - in the same fashion as a) and b) - with the cluster addition probability criterion. A cluster is complete when this algorithm iterates through all possible interacting pairs. For a hard sphere case, eq. (2.2) will either be 0 (no overlap upon point reflection) or ∞ (overlap) so that the eq. (2.1) is unity whenever there is overlap. This whole procedure is illustrated in fig. 2.1. The initially chosen particle was particle 1, and when this particle was reflected, it interacted with particle 2. After testing the probability in eq. (2.1), particle 2 was also moved, after which it was found to interact with particle 3. After another test of eq. (2.1), particle 3 was also moved. At this stage, no further interactions remain to be considered so the configuration shown in fig. 2.1(c) is accepted as the next configuration for the MC method.

There are two central requirements for any Monte Carlo scheme:

- *detailed balance*, which ensures that the Boltzmann probability distribution is generated and that the simulation will be the same forwards or backwards in time
- *ergodicity*, where our scheme should make it possible to reach any state from any other state, given a long enough run time

It is reasonable to assume that the GCA is ergodic by realising that there is a finite probability of obtaining a one particle cluster that reflects through an arbitrarily close pivot - with respect to a particle - such that is possible to reach any system state from any other. We state that the GCA allows a hard sphere system to sample states at thermal equilibrium. For the proof of detailed balance, we refer to the work of Liu and Luijten [62].

2.1.3 GCA for Anisotropic Particles

For an anisotropic system, the point reflection operations of the hard-sphere GCA are not sufficient to satisfy ergodicity. One must be able to relax any orientational degrees of freedom. To this end, Sinkovits et al. added plane reflection to the GCA moveset [66]. Ashton et al. demonstrated this new plane reflection with lock shaped colloids [1]. We reproduce the corresponding moveset figure in fig. 2.2. In this plane reflection move, a random particle is chosen, which is reflected through a random plane. For hard spheres (b), an overlapped particle is automatically added to a cluster. For an arbitrary interaction potential, particles are considered for inclusion according to eq. (2.1). We can see that in (c), a plane reflection move can lead to efficient relaxation of chains of locks without

'breaking' them apart. Any cluster move that includes particles that interact with the periodic particle images are rejected [66]. With this addition, the GCA moveset now satisfies ergodicity. We can see this intuitively by imagining a reflection plane on a lock that allows for an arbitrarily small degree of rotation, such that it will be possible to reach any system state from any other. For proof of detailed balance, we refer to the work of Sinkovits et al. [66].

In this thesis, we simulate both hard colloids with hard nanoparticles and also systems of hard colloids with added "effective attraction potentials". Later on, it will be evident that these effective attraction potentials will refer to the parametrised versions of the potential due to depletion-driven self-assembly. In the case of an additional potential eqs. (2.1) and (2.2) become relevant as there will be a finite chance that a particle that is within range of interaction of another will *not* be added to our cluster. For the hard sphere, we restate that any overlapped particle will always be added to a cluster.

2.1.4 Initialisation of Lock and Key Colloid System

Before running the GCA, the system must be initialised. We achieve this by assigning random initial positions to a fixed number, N, of colloid particles. As the GCA proceeds, we also utilise grand-canonical ensemble Monte Carlo (see, e.g., [67, pp. 204–207]) insertion and deletion for the depletant. The Metropolis acceptance criterion for these insertion and deletion moves is at a specific chemical potential, such that one keeps the nanoparticles at a corresponding mean number density.

2.1.5 Limitations of GCA

Above a certain packing fraction threshold (dependent on system properties), cluster sizes produced by the GCA increases sharply leading to a drop in computational efficiency [62]. It should be evident that the number of particles within a cluster must be lower than the number of particles in the system, otherwise the whole system is simply flipped with no new information gained.

2.2 Concluding Remarks

We have discussed the history and described the geometric cluster algorithm in this chapter. The power of the GCA has been shown to be three-fold: 1. the exploration of dense systems that have traditionally bottle-necked traditional Monte Carlo algorithms 2. the application to arbitrarily shaped particles (provided an ergodic move set can be imagined) 3. the ability to use arbitrary potentials (such as patchy particles). Some main draw backs for the GCA are 1. complexity of implementation and 2. limited use at very dense systems.

This thesis treats the GCA as a way to generate valid, dissimilar configurations of lock and key colloids whose occurrence probability samples the Boltzmann distribution. It should become clear in later chapters that the techniques used to parametrise the self-

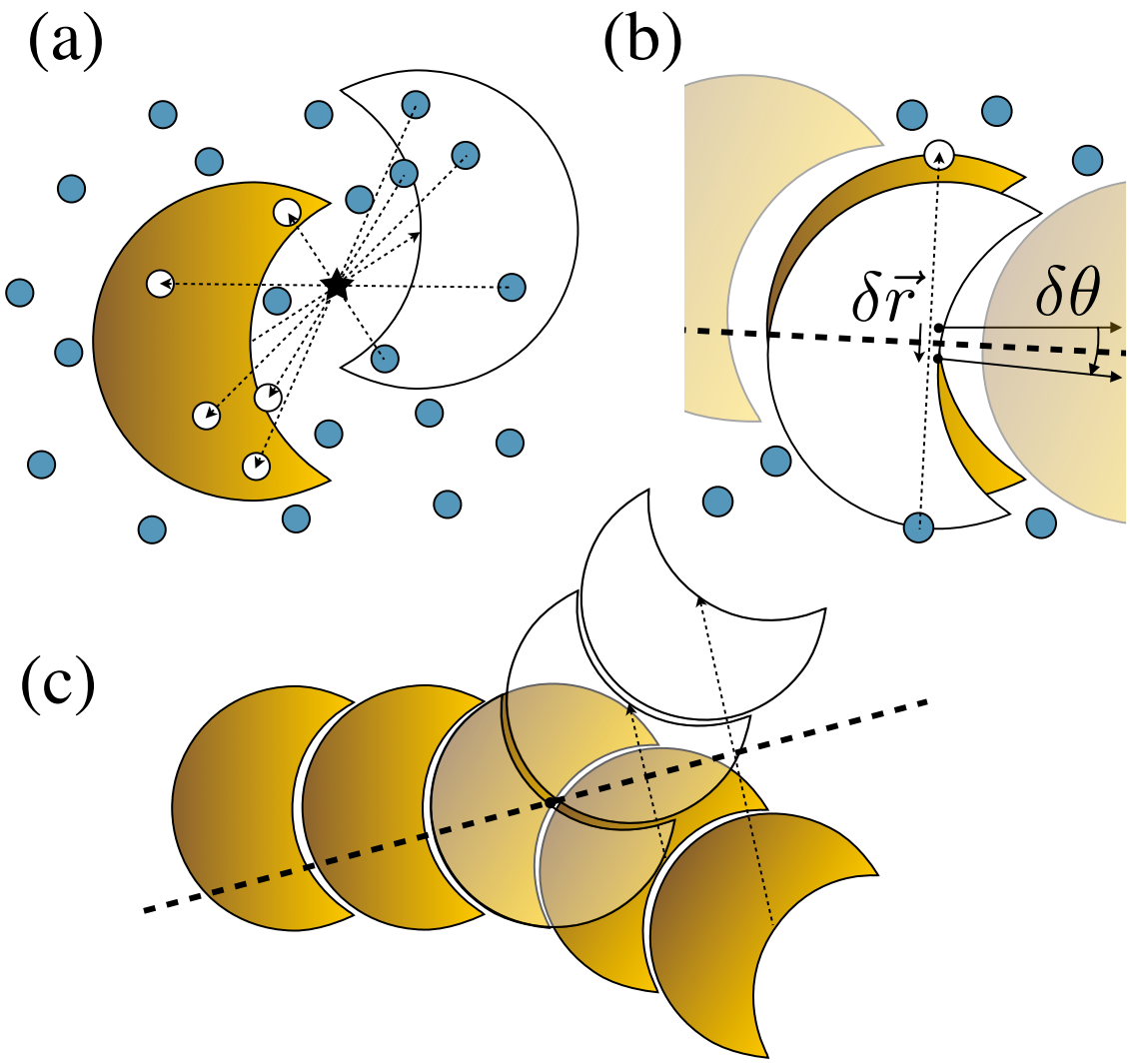

Figure 2.2: Taken with permission from Ashton et al. [1]. An ergodic GCA move set for lock and key colloids. (a) A lock can pivot reflect, through a randomly chosen point. Any particle that is overlapped is point reflected back through the pivot. (b) A lock can also plane reflect, section 2.1.3, where the lock is reflected through a randomly chosen plane such that its new position relative to its old one can be (partially) described through an angle of $\delta\theta$. In practice, one can choose a pivot plane so that the first colloid considered has a small positional, δr, and angular change, $\delta\theta$. This then allows the GCA moveset to model the *rotation* of a particle. (c) For a chain of locks, one can constrain plane reflections to intersect the centre of one of these locks, such that a chain can 'flex' and sample more degrees of freedom as a chain 'unit'.

assembling behaviour of the lock and key colloid is independent from the simulation - or indeed experimental - technique.

Chapter 3

Theory

3.1 Introduction

3.1.1 Depletion Potential

In 1954, Asakura and Oosawa described the immersion of two bodies in a 'solution of macroparticles' [13]. This landmark paper became the first theoretical prediction of the depletion force, in which they considered what were essentially two hard sphere colloids immersed in a solution of penetrable hard spheres (PHS).

For distances between the colloids of less than the diameter of the PHS, 2δ, an unbalanced osmotic pressure arises due to the *depleted* presence of PHS between the colloids. This pressure leads to an *effective* interaction potential which is sometimes called the depletion potential. This argument can be extended to arbitrarily shaped colloids and solutions. Literature generally refers to the particles that induce the osmotic pressure as the depletant, of which the PHS from Asakura and Oosawa - sometimes called AO particles - are a sub-type.

3.1.2 Lock and Key

After the landmark experiment of Sacanna et al. [38], it is clear that lock and key colloids self-assemble due to a depletion potential. It is also clear, see chapter 2, that simulating size asymmetric systems such as a lock and key colloid is generally difficult - be it with conventional small move Monte Carlo or state of the art Monte Carlo techniques like the GCA. Hence, any efforts made to study the quantitative behaviour of lock and key self assembly are hindered by the very thing that causes that self-assembly, namely, the nanoparticles.

Therefore, to eliminate the computational overhead of considering nanoparticles, we assume the existence of effective potentials composed solely of two body effects: between two keys [68], between one lock and one key and between two locks. We show that these two-body effective potentials can be suitably simplified, and when used in a suitable computer simulation, provide an excellent estimation of the self-assembling properties of a lock and key colloid. As well as providing an excellent estimation, the computation overhead

associated with the nanoparticles is completely avoided.

We first describe the general concept of an effective pair potential. Then we introduce the lock and key coordinate system, an important step in developing any other tools to concisely simplify the effective potential of a lock and key system. We then describe the probability distribution for the positions of the lock and key, we define the relation between the pair distribution function and the probability density of a dilute fluid, and then connect the pair distribution function with the effective potential of the same, general, system. These relations are then shown to be directly applicable to the lock and key system and thus provide an important tool in the parametrisation of the lock and key effective potential. We then introduce the equilibrium constant for studying the free energy of the lock and key effective potential.

We also derive the partition function for a lock and key system with ideal gas nanoparticles. We show how this partition function can be used with the equilibrium constant to predict the free energy of the lock and key system.

We show how the tools and arguments developed for the lock and key system generalise to a two lock system.

3.2 Asakara-Oosawa Effective Pair Potential

Our aim is to describe a system of hard locks in the presence of depletant by a system consisting only of interacting locks. The interactions among the locks mimic the effect of the depletant. We will assume that a pairwise interaction potential is sufficient for this purpose. Given these assumptions, for the previously described AO system, standard liquid state theory [44, p. 35] states that the radial distribution function, $g(r)$, of a large number of sparsely distributed, identical spherical colloids interacting with a large number of AO particles is related to the effective pair potential, $W^{\eta}(r)$, of the same fluid at an arbitrary density of AO particles, η, present:

$$\beta W^{\eta}(r) \equiv \lim_{\rho \to 0} -\ln[g^{\eta}(r)] \tag{3.1}$$

Henceforth, we set the inverse thermal energy factor, β, to be unity. The pair potential, $W^{\eta}(r)$, describes the potential between two hard spherical particles under the depletion forces of AO particles. The contribution due solely to AO particles can be represented as $\Delta W^{\eta}(r)$, which from now on we call the effective potential. With these two pieces, the hard particle contribution to the pair potential, $W^{0}(r)$, can be simply defined in terms of a contribution to $W^{\eta}(r)$:

$$\Delta W^{\eta}(r) \equiv W^{\eta}(r) - W^{0}(r). \tag{3.2}$$

3.3 Effective Potential

In the previous section, we discussed the effective pair potential of an AO system. By simply extending eq. (3.2) to a greater number of relevant coordinates, we find that we

will be able to completely describe the effective potential due to a lock and key (and nanoparticle) colloidal system. We first state that our one lock and one key exist in a cubic box of size L. We also note that from now on, the over-tilde signifies that the relevant quantity is calculated for just two particles in finite simulation boxes.

3.3.1 Lock and Key Coordinate System

To describe the interactions between a lock and key particle, we need to take into account the shape of the lock. This requires the definition of a suitable coordinate system. Figure 3.1 demonstrates such a coordinate system used to describe a one lock and one key system. Importantly, the direction vector, $\hat{\boldsymbol{n}}$, is a unit vector and always points *away* from the lock. The radial vector, $\boldsymbol{r}$, also points away from the lock centre and towards the key centre. Note that $\boldsymbol{r}$ and $\hat{\boldsymbol{n}}$ form an angle, θ, i.e., $\cos\theta = \frac{\boldsymbol{r}.\hat{\boldsymbol{n}}}{r}$, where we write the magnitude of the radial vector as $r = |\boldsymbol{r}|$. For brevity, we will write $c \equiv \cos\theta$.

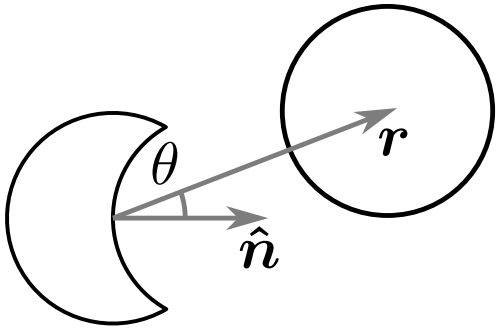

Figure 3.1: Demonstration of the coordinate system used to describe a single lock and single key system.

3.3.2 Probability Density

We now introduce a basic tool to analyse the lock and key effective potential. We represent the probability density of a system of one lock and one key at any nanoparticle density, η, with the following notation:

$$\tilde{\mathbb{P}}^{\eta}_{\mathrm{LK}}(r, \cos\theta_{\mathrm{r}}) \equiv \tilde{\mathbb{P}}^{\eta}_{\mathrm{LK}}(r, c). \tag{3.3}$$

We note that $\tilde{\mathbb{P}}^{\eta}_{\mathrm{LK}}$ is the probability density of a finite system. We can write expressions such as

$$\tilde{\mathbb{P}}^{\eta}_{\mathrm{LK}}(r) = \int_{-1}^{1} \mathrm{d}c\, \tilde{\mathbb{P}}^{\eta}_{\mathrm{LK}}(r, c), \tag{3.4}$$

where $\tilde{\mathbb{P}}^{\eta}_{\mathrm{LK}}(r)$ implies that we have integrated $\tilde{\mathbb{P}}^{\eta}_{\mathrm{LK}}(r, c)$ over all coordinates other than r. $\tilde{\mathbb{P}}^{\eta}_{\mathrm{LK}}(r)$ is an example of a *marginal* probability distribution.

3.3.3 Radial Distribution Function

The effective potential, $W(r)$, defined in eq. (3.2), requires $g(r)$ for a large system in the dilute limit. However, for low densities, the probability of three particles simultaneously

interacting with each other is very small. This means that $W(r)$ can be deduced from a simulations of two particle systems. We can then write the radial distribution function for a lock and key in a infinite sized system - such that the density of locks and keys, ρ, tends to 0 - at an arbitrary nanoparticle concentration, η, as a ratio of probability densities:

$$\lim_{\rho\to 0} g^{\eta}(r) = \lim_{L\to\infty} \frac{\mathbb{P}^{\eta}_{\mathrm{LK}}(r)}{\mathbb{P}^{\mathrm{IG}}_{\mathrm{LK}}(r)}, \tag{3.5}$$

where L is the size of the system in question. The two-dimensional pair distribution function (including the angular component) is written in an analogous way:

$$\lim_{\rho\to 0} g^{\eta}(r,c) = \lim_{L\to\infty} \frac{\mathbb{P}^{\eta}_{\mathrm{LK}}(r,c)}{\mathbb{P}^{\mathrm{IG}}_{\mathrm{LK}}(r,c)}. \tag{3.6}$$

Equation (3.5) can be thought of as the probability of finding a hard lock at a specific radius with respect to a hard key, normalised to the same probability measurement for two point particles, $\mathbb{P}^{\mathrm{IG}}_{\mathrm{LK}}(r)$. In the same way, eq. (3.6) is the probability of finding a lock at a specific radius and angle, c, with respect to a key, normalised to the same probability measurement for two point particles, $\mathbb{P}^{\mathrm{IG}}_{\mathrm{LK}}(r,c)$.

The radial distribution function, $g^{\eta}(r)$, should tend to unity as our system tends to an infinite size [44, p. 29]:

$$\lim_{r\to\infty} g(r) = 1. \tag{3.7}$$

In a finite system of size L, a measured pair distribution function - which we denote as $\tilde{g}$ - will deviate everywhere by a constant scale factor proportional to the value of $\tilde{g}(r = {}^{L}/_{2})$. One can then, in the same fashion as Ashton and Wilding [69], recover the true radial distribution function for an infinite sized system $g^{\eta}(r)$:

$$g(r) = \frac{\tilde{g}(r)}{\tilde{g}(r = {}^{L}/_{2})}. \tag{3.8}$$

Equivalently, one can recover the true two-dimensional pair distribution function for an infinite sized system $g(r,c)$:

$$g(r,c) = \frac{\tilde{g}(r,c)}{\tilde{g}(r = {}^{L}/_{2})}. \tag{3.9}$$

We use the value of $\tilde{g}$ at ${}^{L}/_{2}$ as this is the maximal distance at which $g(r)$ can be measured. One corrects any probability density, $\tilde{\mathbb{P}}^{\eta}_{\mathrm{LK}}$, sampled from a system of size L in an analogous way, e.g.,

$$\mathbb{P}^{\eta}_{\mathrm{LK}}(r) = \frac{\tilde{\mathbb{P}}^{\eta}_{\mathrm{LK}}(r)}{\tilde{g}^{\eta}(r = {}^{L}/_{2})} \tag{3.10}$$

and

$$\mathbb{P}^{\eta}_{\mathrm{LK}}(r,c) = \frac{\tilde{\mathbb{P}}^{\eta}_{\mathrm{LK}}(r,c)}{\tilde{g}^{\eta}(r = {}^{L}/_{2})}. \tag{3.11}$$

3.3.4 Connecting Probability Density to Effective Potential

From eq. (3.1) and eq. (3.5), it follows that the pair potential between a hard lock and key in an infinitely large, dilute fluid with arbitrary nanoparticle density, η, is

$$W^{\eta} = -\log\left(\frac{\mathbb{P}^{\eta}_{\mathrm{LK}}}{\mathbb{P}^{\mathrm{IG}}_{\mathrm{LK}}}\right). \tag{3.12}$$

The hard, non-overlapping, contribution to W^{η} is

$$W^{0} = -\log\left(\frac{\mathbb{P}^{\eta=0}_{\mathrm{LK}}}{\mathbb{P}^{\mathrm{IG}}_{\mathrm{LK}}}\right) \tag{3.13}$$

and therefore the nanoparticle contribution to W^{η}, ΔW, is

$$\Delta W^{\eta} = -\log\left(\frac{\mathbb{P}^{\eta}_{\mathrm{LK}}}{\mathbb{P}^{\eta=0}_{\mathrm{LK}}}\right). \tag{3.14}$$

We emphasise that these probability densities are already normalised by the value of $g^{\eta}(r)$ at $L/2$ and as such do *not* have an over-tilde. These equations will be used in later sections to estimate effective potentials from numerical data.

3.4 Partition Function

Now that we have developed some equations to connect the probability distribution of a lock and key system to an effective potential, it would also be useful to have a theoretical argument for predicting some thermodynamic quantities of our lock and key system. An important thermodynamic quantity quoted in the seminal lock and key paper by Sacanna et al. [38] is the binding free energy of a lock and key due to the depletion interaction. We will now derive the partition function for a lock and key colloid (both impenetrable, or hard) - in a sea of AO particles - from which we can produce an analytic expression of the binding free energy. We highlight that we are using AO particles as a depletant, but that the previous sections did *not* assume AO depletant. In our posited system the particles exist within a box of size V. We can write a very general partition, looking at configurations with respect to the nanoparticles:

$$\mathcal{Z} = \int \mathrm{d}\boldsymbol{R} \int \mathrm{d}\boldsymbol{r} \int \mathrm{d}\boldsymbol{\Omega}\, \psi(\boldsymbol{r}, \boldsymbol{\Omega}). \tag{3.15}$$

$\boldsymbol{R}$ represents the centre of mass coordinate between the lock and the key, $\boldsymbol{r}$ represents the relative position vector between the lock and the key and $\boldsymbol{\Omega}$ represents all possible angular orientations of the lock[1]. The integrals associated with these coordinates represent a summation over all possible degrees of freedom for the lock and key. If there were only locks and keys in our system, and they acted as an ideal gas, then our partition function would simply be $\mathcal{Z} = \int \mathrm{d}\boldsymbol{R} \int \mathrm{d}\boldsymbol{r} \int \mathrm{d}\boldsymbol{\Omega}$. However, we have the constraint that the locks and

[1] That is, the solid angle.

keys are hard and also nanoparticles that are AO particles. This constraint is introduced into our partition function as a sum over all possible states of nanoparticle [70, pp. 229-230]:

$$\psi(\boldsymbol{r}, \boldsymbol{\Omega}) = \sum_N \frac{\mathrm{e}^{-\mu N}}{N!} \left[v_{\mathrm{free}}(\boldsymbol{r}, \boldsymbol{\Omega})\right]^N \frac{1}{\Lambda^{3N}}. \tag{3.16}$$

N is the total number of nanoparticles in our system and this is specified by the chemical potential, μ, of our system such that we are now considering the nanoparticles as a grand canonical ensemble. We introduce the normalising factors of $N!$ and the Thermal de Broglie wavelength[2], $\Lambda = {}^{h}/\sqrt{2\pi m k_{\mathrm{B}} T}$, as our nanoparticles are indistinguishable. v_{free} is the volume accessible to the nanoparticles. We note that from now on, a lower case v refers to nanoparticles whilst a upper case V (with a relevant subscript) generally refers to the larger lock and/or key. We can make a few remarks about eqs. (3.15) and (3.16):

1. The probability of a state in the system with the coordinate vectors $\boldsymbol{R}$, $\boldsymbol{r}$ and $\boldsymbol{\Omega}$ is a ratio of eq. (3.16) to eq. (3.15), i.e.,

$$P(\boldsymbol{R}, \boldsymbol{r}, \boldsymbol{\Omega}) = \frac{\psi(\boldsymbol{r}, \boldsymbol{\Omega})}{\mathcal{Z}}, \tag{3.17}$$

   where we note that the effective potential W^η in eq. (3.12) comes from the negative logarithm of the ratio of $\psi(\boldsymbol{r}, \boldsymbol{\Omega})$ at an arbitrary nanoparticle concentration, η, and at zero concentration.

2. One can also see that eq. (3.16) is a power series that approximates an exponential function, i.e.,

$$\psi(\boldsymbol{r}, \boldsymbol{\Omega}) = \exp\left(\mathrm{e}^{-\mu} \frac{v_{\mathrm{free}}(\boldsymbol{r}, \boldsymbol{\Omega})}{\Lambda^3}\right), \tag{3.18}$$

   and thereby realise that any nanoparticle configuration is only dependent on μ, Λ, and the volume available to it, v_{free}.

3. From standard thermodynamics, one can also calculate the mean number of nanoparticles,

$$\langle N \rangle = -\frac{\partial}{\partial \mu} \ln \psi(\boldsymbol{r}, \boldsymbol{\Omega}) = \mathrm{e}^{-\mu} \frac{v_{\mathrm{free}}(\boldsymbol{r}, \boldsymbol{\Omega})}{\Lambda^3} \tag{3.19}$$

   and if we define the concentration of nanoparticles particles, n, as

$$n \equiv \frac{\langle N \rangle}{v_{\mathrm{free}}(\boldsymbol{r}, \boldsymbol{\Omega})}, \tag{3.20}$$

   that is, the mean number of nanoparticles per unit volume (accessible to the nanoparticles), we have

$$n = \frac{\mathrm{e}^{-\mu}}{\Lambda^3}. \tag{3.21}$$

   In other words, the concentration of nanoparticles is only dependent on μ and Λ.

[2]This comes from the quantum mechanical theory of the partition function, of which our derivation exists in the classical limit.

With the afore listed remarks, we can approximate eq. (3.16) - the probability of a lock-key pair inhabiting any state - as

$$\psi(\boldsymbol{r}, \boldsymbol{\Omega}) = \exp(n v_{\text{free}}(\boldsymbol{r}, \boldsymbol{\Omega})). \tag{3.22}$$

Having the lock-key probability distribution principally dependent on volume available to nanoparticle will prove fortuitous as we have shown that $\psi(\boldsymbol{r}, \boldsymbol{\Omega})$ will allow us to calculate the effective potential, W^{η}. In the upcoming discussion, we will decompose the partition function into two sections and show how one can obtain simple expressions for the volume available to the nanoparticle.

3.4.1 Decomposing the Lock and Key Partition Function

We first state that a lock and key pair is bound when the key is within a certain, small, distance of the lock mouth. This will be quantified later. An unbound key is then every position that is *not* bound.

It should be clear that general partition function that describes our system, eq. (3.15), can be decomposed into two distinct sections: states when our lock and key are bound, together $\mathcal{Z}_{\text{B}}$, and when they are unbound, $\mathcal{Z}_{\text{UB}}$:

$$\mathcal{Z} = \mathcal{Z}_{\text{B}} + \mathcal{Z}_{\text{UB}}. \tag{3.23}$$

From this, we can write straight away that the probability for a lock and key being bound and unbound are, respectively,

$$\mathbb{P}_{\text{B}} = \frac{\mathcal{Z}_{\text{B}}}{\mathcal{Z}} \tag{3.24}$$

and

$$\mathbb{P}_{\text{UB}} = \frac{\mathcal{Z}_{\text{UB}}}{\mathcal{Z}}. \tag{3.25}$$

For the states where the lock and key are unbound, the partition function of the unbound lock and key states can be written in a similar way to eq. (3.15):

$$\mathcal{Z}_{\text{UB}} = \int_{\text{UB}} \mathrm{d}\boldsymbol{R}\, \mathrm{d}\boldsymbol{r}\, \mathrm{d}\boldsymbol{\Omega} \psi_{\text{UB}}, \tag{3.26}$$

where we are considering all possible configurations that the nanoparticles could be in if the lock and key are unbound. We can simplify this partition function by noting that the integral can be separated from the nanoparticle probability function:

$$\int_{\text{UB}} \mathrm{d}\boldsymbol{R}\, \mathrm{d}\boldsymbol{r}\, \mathrm{d}\boldsymbol{\Omega} = 4\pi V (V - V_{\text{K,UB}}) \tag{3.27}$$

where $V_{\text{K,UB}}$ is the total volume *not* accessible to the centre of a hard key in an unbound system containing a single lock. We therefore assume that ψ_{UB} is independent of the location of an unbound lock and unbound key. The total volume available to the nanoparticles in an unbound state is the system volume, V, minus the volume of a single lock, V_L, and

that of a single key, V_K, i.e.,

$$v_{\mathrm{UB}} = V - V_{\mathrm{L}} - V_{\mathrm{K}}. \tag{3.28}$$

Piecing everything together, we can substitute eq. (3.28) into the general nanoparticle partition function (eq. (3.22)), and replace the integrand in eq. (3.26) with eq. (3.27) such that the total number of states that the system can assume when the lock and key are unbound is

$$\mathcal{Z}_{\mathrm{UB}} = \pi V (V - V_{\mathrm{K,UB}}) \exp\left[n \left(V - V_{\mathrm{L}} - V_{\mathrm{K}}\right)\right]. \tag{3.29}$$

For the states where the lock and key are bound, the partition function of the bound lock and key states can also be written in a similar way to eq. (3.15):

$$\mathcal{Z}_{\mathrm{B}} = \int_{\mathrm{B}} \mathrm{d}\boldsymbol{R}\, \mathrm{d}\boldsymbol{r}\, \mathrm{d}\boldsymbol{\Omega} \psi_{\mathrm{B}}. \tag{3.30}$$

We can approximate this partition function by, again, separating out the integral from the nanoparticle probability function. We can consider the volume that a key could possibly inhabit if it were in an bound state as

$$\int_{\mathrm{B}} \mathrm{d}\boldsymbol{R}\, \mathrm{d}\boldsymbol{r}\, \mathrm{d}\boldsymbol{\Omega} = 4\pi V V_{\mathrm{K,B}}, \tag{3.31}$$

where $V_{\mathrm{K,B}}$ represents the small region where a key would bind perfectly to a lock, as demonstrated in fig. 3.2. We make a note here that δ, when used with r, is a *number*, not a signifier that r is small. This is used, for example, in fig. 3.2. We assume that ψ_{B} is maximal within some small value of $V_{\mathrm{K,B}}$, and that this maximum function dominates over all other values of ψ_{B}. This is reasonable because the number of possible states that the nanoparticles can possess is greatest when a lock and key is bound. For a given increase in nanoparticle density, above a certain value, any possible *reduction* in $V_{\mathrm{K,B}}$ will be balanced by the statistical unlikelihood of a key docking into the lock mouth. Thus, we can also assume that at sufficiently high nanoparticle number densities ψ_{B} is a constant value regardless of a key's location *within the bound volume* and that $V_{\mathrm{K,B}}$ is itself independent of nanoparticle concentration.

However, for lower nanoparticle concentrations, there will be insufficient depletion force to confine a key into a lock mouth. This will mean that the $V_{\mathrm{K,B}}$ will begin to be sensitive to nanoparticle concentration, leading to a *variable* ψ_{B} as there could conceivably be unbound lock-key configurations that have similar free energy to a bound-lock key. Using this assumption, the precise volume available to the nanoparticles at perfect fit is

$$V_{\mathrm{K,B}} = V - V_{\mathrm{LK}} \tag{3.32}$$

so that

$$\mathcal{Z}_{\mathrm{B}} = (4\pi)^2 V V_{\mathrm{b}} \exp\left[n \left(V - V_{\mathrm{LK}}\right)\right]. \tag{3.33}$$

Looking back to the definition of the probability that a particle was bound or unbound (eqs. (3.24) and (3.25)), we can see very clearly that the depletion interaction depends very

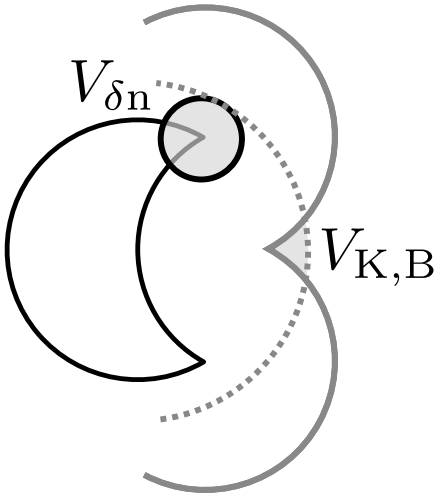

Figure 3.2: A two-dimensional figure that can be extended to demonstrate the volume available to a key in the *bound* state. This can be more precisely defined as the volume formed from the intersection of a sphere, of radius $r_{\mathrm{L}}+r_{\mathrm{n}}$ centred on the lock centre (dashed grey line), and two spheres of radius r_{K} (solid grey lines) centred on the two points (or edges, in 3D) of the lock mouth. For this particular geometry ($\delta = 2.0$), $V_{\mathrm{K,B}} \sim {}^{V_{\delta \mathrm{n}}}/_{4}$, where $V_{\delta \mathrm{n}}$ is a sphere of radius δr_{n}.

strongly on the exclusion volume, i.e., $\Delta V_{\mathrm{LK}} \equiv V_{\mathrm{L}} + V_{\mathrm{K}} - V_{\mathrm{LK}}$. This is very important, as we will go on to show how one can derive the binding free energy from the partition function of the lock and key colloid.

3.5 Equilibrium Constants

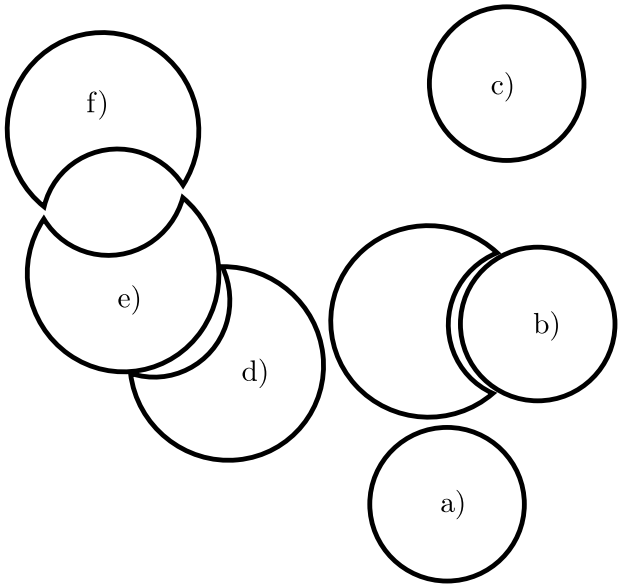

Figure 3.3: This figure demonstrates possible distinct configurations for a multiple lock-key configuration. With respect to the unlabelled lock, particle a) is called a touching key, b) is a bound key, c) is an unbound key, d) is a touching lock. With respect to lock d), e) is a bound lock. With respect to particle e), f) is a mouth-mouth lock. We make the simplifying assumption that configuration f) is rare enough to discount. This assumption is removed in later numerical studies.

So far, we have considered two distinct positions that a lock and key can be in, namely bound, i.e., a key that is docked with a lock mouth, and unbound, i.e., when a key and lock are completely separate. We choose to introduce one additional case, and we define it here as the back-back position, that is, when a key is touching the lock but not near the lock mouth. Before, the unbound category subsumed the back-back category. Later on, we introduce more possible categories if many locks and many keys are present (subsumed by the current definition of unbound). These are demonstrated in fig. 3.3. It should be clear that the exclusion volume for the back-back case is equivalent to the hard sphere case (ΔV_{HS}).

We call a particle bound if it is less than a distance r_{B} away from another particle. We say a particle is in the back-back regime if it satisfies the distance relation $r_{\mathrm{L}} \leq r \leq r + \delta r_{\mathrm{n}}$, where δ defines how tolerant we are of particles that are close to the surface of another. Later on, we write a full angular and radial distance relation that a particle must satisfy to be in the back-back regime, but for now, we use the simplifying assumption that the number of particles in a true back-back regime is much greater than the number that are in the 'shell' just above a lock mouth. We can finally say that an unbound particle is one that *is not* bound or in the touching regime.

We will now show that these three categorisations allow for a relatively simple prediction of associated free energies.

3.5.1 Separate and Bound

As a simple example, we first assume that a lock and key colloid can only exist in the states of completely bound or completely separate. We can represent a system of many locks and many keys undergoing self-assembly due to nanoparticles with a chemical equation:

$$\mathrm{L} + \mathrm{K} \rightleftarrows \mathrm{LK}. \tag{3.34}$$

Here, the double arrow signifies a continual binding/unbinding of locks and keys, stabilised at some equilibrium concentration of single locks, keys and bound lock-keys. The law of mass action [71, p. 112–113] predicts the number density, or concentration, of bound lock key pairs, ρ_{B}, as a product of single lock and single key number densities (ρ_{L} and ρ_{K} respectively), i.e.,

$$\rho_{\mathrm{B}} = \mathcal{K}_{\mathrm{B}} \rho_{\mathrm{L}} \rho_{\mathrm{K}}, \tag{3.35}$$

where $\mathcal{K}_{\mathrm{B}}$ is defined as the *equilibrium constant* of eq. (3.35). $\mathcal{K}_{\mathrm{B}}$ has units of volume. We note that each variable in eq. (3.35) depends upon multiple system parameters, e.g., η, lock and key geometry, etc., but do not write this explicitly for the sake of brevity.

The equilibrium constant, $\mathcal{K}_{\mathrm{B}}$, can be related to the probability that two particles are found in the bound state. As shown in Appendix B, this leads to the following definition:

$$\mathcal{K}_{\mathrm{B}} = \int_0^{r_{\mathrm{B}}} \mathrm{d}r \, 4\pi r^2 g(r). \tag{3.36}$$

where r_{B} is the maximum radial limit in which a key is defined as bound.

3.5.2 Separate, Back-back or Bound

We now extend the previous section's method to incorporate the possibility that a lock and key can bind in a back-back configuration (fig. 3.3). We can represent a system of many locks and many keys undergoing self-assembly as a constant state of flux between the bound, unbound and touching states. This can be described with another chemical equation:

$$\mathrm{LK_{BB}} \rightleftarrows \mathrm{L} + \mathrm{K} \rightleftarrows \mathrm{LK_{B}}, \tag{3.37}$$

where we refer to configurations of lock and key that touch but are not within the 'mouth' of the lock as 'back-back' (BB). There are now two equilibrium constants: $\mathcal{K}_{\mathrm{B}}$ which describes the relationship between the number densities of bound lock-keys and separate lock and separate keys and $\mathcal{K}_{\mathrm{BB}}$ which describes the relationship between the number densities of 'back-back' lock-keys and separate locks and separate keys. $\mathcal{K}_{\mathrm{B}}$ appears exactly as in eq. (3.35), whilst $\mathcal{K}_{\mathrm{BB}}$ involves the 'back-back' (BB) lock-key number densities:

$$\rho_{\mathrm{BB}} = \mathcal{K}_{\mathrm{BB}} \rho_{\mathrm{L}} \rho_{\mathrm{K}}. \tag{3.38}$$

We note that the total lock concentration (in whatever state) now obeys the relation:

$$\rho_{\mathrm{L}}^{\mathrm{tot}} = \rho_{\mathrm{L}} + \rho_{\mathrm{B}} + \rho_{\mathrm{BB}}. \tag{3.39}$$

Analogous to eq. (3.36), $\mathcal{K}_{\mathrm{BB}}$ can be expressed as an integral of the radial distribution function:

$$\mathcal{K}_{\mathrm{BB}} = \int_{r_{\mathrm{L}}}^{r_{\mathrm{L}}+\delta r_{\mathrm{n}}} \mathrm{d}r 4\pi r^2 g(r) \tag{3.40}$$

where BB indicates that $\mathcal{K}_{\mathrm{BB}}$ only includes the back-back region of the probability distribution.

3.5.3 Free Energies

As a helpful reference point for different lock and key systems, the equilibrium constants can then be viewed as free energies [8, p. 1436], such as the binding (or bound) free energy:

$$F_{\mathrm{B}} = -\ln\left(\frac{\mathcal{K}_{\mathrm{B}}}{V_\sigma}\right) \tag{3.41}$$

and the back-back free energy:

$$F_{\mathrm{BB}} = -\ln\left(\frac{\mathcal{K}_{\mathrm{BB}}}{V_\sigma}\right). \tag{3.42}$$

Note that the equilibrium constants have units of volume, so we normalise the equilibrium constant by the natural unit volume the system: $V_\sigma = {}^{4\pi\sigma^3}/_{24}$, where σ is the diameter of

a lock or key.

3.5.4 Free Energy Prediction

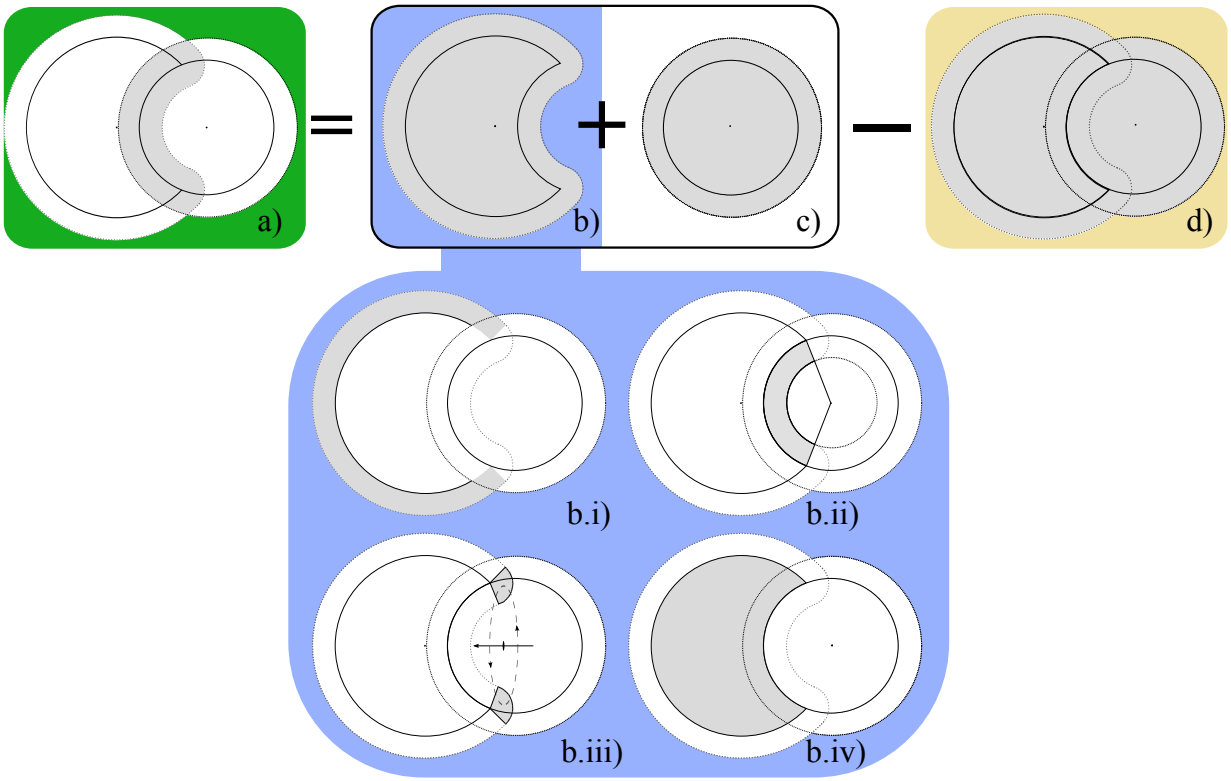

Figure 3.4: A two dimensional representation of the exclusion volumes (the grey shaded areas) of a lock and key colloid. When the two colloids are separate, b) & c), their exclusion volumes, V_{L} and V_{K}, are greater than when they *locked* together, V_{LK}, d). The exact volume remaining, a), is known as the overlap volume, $\Delta V = V_{\mathrm{L}} + V_{\mathrm{K}} - V_{\mathrm{LK}}$. The area of a) can be constructed by summing the individual grey areas from b.i) to c) and then from this sum subtracting d). These 2D arguments for area transform exactly into a 3D argument of volume. We note an approximate, simpler, calculation of ΔV in Appendix A. A helpful diagram for useful information needed to calculate the exact 3D ΔV is shown in fig. A.2.

We are now able to make a prediction for binding free energy utilising the partition functions for a lock and key system derived in section 3.4. We can rewrite $\mathcal{K}_{\mathrm{B}}$ in terms of partition functions:

$$\tilde{\mathcal{K}}_{\mathrm{B}} = \frac{\tilde{\mathcal{Z}}_{\mathrm{B}}}{\tilde{\mathcal{Z}}_{\mathrm{UB}}} V. \tag{3.43}$$

We repeat that the partition function subscripts refer to the bound and unbound states. The tildes signify a finite sized system. Substituting eq. (3.33) and eq. (3.29) into eq. (3.43), we obtain

$$\tilde{\mathcal{K}}_{\mathrm{B}}^{\mathrm{IG}} = \frac{V_{\mathrm{B}} \exp\left[n\left(V - V_{\mathrm{LK}}\right)\right]}{4\pi(V - V_{\mathrm{K,UB}}) \exp\left[n\left(V - V_{\mathrm{L}} - V_{\mathrm{K}}\right)\right]} V. \tag{3.44}$$

If we let the system volume tend to infinity, then we finally arrive at:

$$\lim_{V\to\infty} \mathcal{K}_{\mathrm{B}}^{\mathrm{IG}} = V_{\mathrm{B}} \exp\left(n\Delta V\right) \tag{3.45}$$

where the exclusion volume is

$$\Delta V = V_{\mathrm{L}} + V_{\mathrm{K}} - V_{\mathrm{LK}} \tag{3.46}$$

as shown in fig. 3.4. In more detail, fig. 3.4 demonstrates a two-dimensional reconstruction of how to calculate the three-dimensional exclusion volume of an exactly bound lock and key colloid. Specifically, the shaded region in fig. 3.4a) is ΔV, b) is V_{L}, c) is V_{K} and therefore d) is V_{LK}, so that one can use eq. (3.46) to calculate ΔV. An approximate, simpler, method to calculate ΔV is shown in Appendix A. A helpful diagram for useful information needed to calculate the exact 3D ΔV is shown in fig. A.2.

Normalising eq. (3.45) by V_σ then allows us to predict the binding free energy of a lock and key system with ideal gas nanoparticles in terms of various lock and key geometrical factors:

$$\Delta F_{\mathrm{B}}^{\mathrm{IG}} = -\ln\left(\frac{V_{\mathrm{B}}}{V_\sigma}\right) - n\Delta V. \tag{3.47}$$

where we can define the nanoparticle concentration, n, in terms of nanoparticle density, η:

$$n = \frac{\eta}{V_{\mathrm{n}}} \tag{3.48}$$

where $V_{\mathrm{n}} = {}^{4\pi r_{\mathrm{n}}^3}/_3$ is the volume of a nanoparticle with radius r_{n}.

3.6 Lock and Lock Coordinate System

We now develop the coordinate system for two locks, with the foresight of developing an effective potential for the same system in later sections. We will see that with the suitable choice of coordinate system, we are able to reuse much of the upcoming methodology of parametrising the lock and key coordinate system.

Figure 3.5 demonstrates a set of coordinates that are able to describe a two lock system. Unlike the lock and key coordinate system, a two lock system is distinguished by numerical labels. Importantly, $|\boldsymbol{r}_1 - \boldsymbol{r}_2| = r$. The angles between the directors and the radial vectors are calculated using the same process as section 3.3.1.

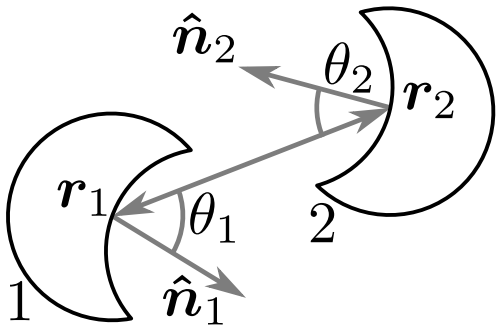

Figure 3.5: Demonstration of a set of coordinates that are able to describe a two lock system.

We can simplify fig. 3.5 through the following assignments:

$$\theta_{\mathrm{R}} = \min(\theta_1, \theta_2) \tag{3.49}$$

$$\theta_{\mathrm{I}} = \max(\theta_1, \theta_2), \tag{3.50}$$

where we decide, depending on the relative magnitudes of θ_1 and θ_2, on the most relevant, θ_{R} (and therefore also the most irrelevant, θ_{I}) angle formed between the radial vectors and the directors. We can see a demonstration of this in fig. 3.6, which shows that the range of orientations of lock 2 for which the combined locks' excluded volumes remain similar is much greater than for lock 1. Therefore, it is pertinent to assume that the smaller angle has a greater influence on the depletion potential. The identification of the relevant and irrelevant angles will be justified in chapter 5. If $\theta_1 = \theta_2$, we always choose $\theta_{\mathrm{R}} = \theta_1$. We can further simplify fig. 3.5 by taking the angle between the two director vectors,

$$\cos\varphi = \hat{\boldsymbol{n}}_1.\hat{\boldsymbol{n}}_2, \tag{3.51}$$

allowing us to describe a two lock system with four coordinates: $r, \theta_{\mathrm{R}}, \theta_{\mathrm{I}}, \varphi$, as depicted in fig. 3.7. For brevity, we write $\cos\theta_{\mathrm{R}} \equiv c_{\mathrm{r}}$, $\cos\theta_{\mathrm{I}} \equiv c_{\mathrm{i}}$ and $\cos\varphi \equiv c_{\varphi}$.

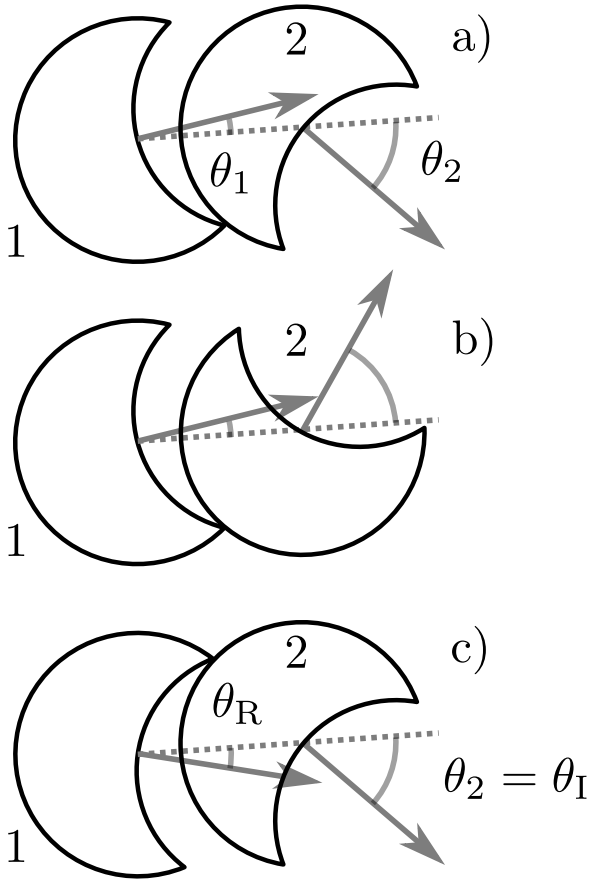

Figure 3.6: A schematic to demonstrate why we choose to make the smaller angle between director and radial vector - which we denote director angle for brevity - the relevant angle, θ_R. The range of orientations of 2 for which the combined locks' excluded volumes remain similar is much greater than 1. Thus, we always assume that the smaller angle has the greater influence on the depletion potential.

.

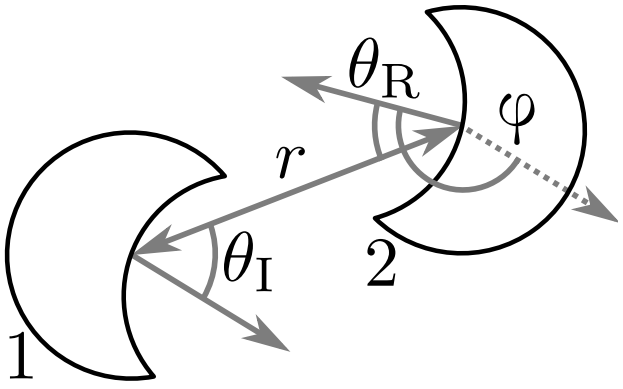

Figure 3.7: Demonstration of the simplest set of coordinates that can describe a two lock system.

3.7 Conclusion

Using the concept of the pair potential from standard liquid state theory, we have introduced the theoretical lock and key system and shown how it is possible to connect its probability distributions back to an analogous pair potential.

Further, we have described approximate partition functions for this lock and key system

and shown that it is possible to predict the free energy of specific configurational states of a lock and key colloid.

With foresight, we have also introduced the simplest lock and lock coordinate system and shown any necessary modifications to the lock-key specific tools.

In later chapters, we will contrast this predicted free energy of a lock and key system with a measured one, describing and explaining any differences. We will also use the concepts developed in this chapter to parametrise the effective potential for both the lock-key and lock-lock systems in a logical manner.

Chapter 4

Results for Lock and Key System

It is clear that to describe a self assembling lock and key colloid, one must have the depletion potential between a lock and key and also between two locks and between two keys. This chapter outlines the typical effective potential for an exactly matching lock and key system, laying out a reasonable strategy for simplifying the potential and finally presenting proof-of-concept parametrised effective potentials generated from real, nanoparticle-less simulations. This whole process is repeated for a mismatched lock and key system. By exact lock and key, we are referring to when a key can fit exactly into the mouth of a lock with no possible room for manoeuvre. From this, it should be clear that a mismatch lock refers to when a key does not fit exactly into a lock mouth. Here, we are simulating one lock and one key in a box with many (hard) nanoparticles using the geometric cluster algorithm (GCA). With reference to fig. 1.4, the box is cubic with a length of 3σ, where σ is the diameter of a key. We fix units by setting $\sigma = 1$. The locks and keys have radii of $r_{\mathrm{L}} = r_{\mathrm{K}} = 0.5$ whilst the nanoparticle's radii, $r_{\mathrm{n}} = 0.05$. The lock's cutting sphere radius, r_{c}, and distance between cutting sphere and lock centre, d_{c}, is also 0.5.

4.1 Typical Effective Potential

It is helpful to plot the radial distribution function, $g(r)$, between a lock and key pair as we know that the effective potential of the same system is related to the pair distribution via eqs. (3.5) and (3.14). Figure 4.1 depicts three (normalised) radial distribution functions for three different nanoparticle densities, η. We see very clearly that there is a peak at $r = 0.5$ that corresponds to the key binding to the mouth of the lock. We call this the 'bound regime'. We also see a peak at $r = 1.0$, which we term the 'back-back regime', that is associated with the lock and key touching without being near the mouth. We can see in fig. 4.2 that the full, two-dimensional effective potential includes a radial as well as an orientational dependence between a lock and key. We can see that the orientational dependence from fig. 4.1 is not clear but must be inferred from geometrical knowledge of the lock and key system.

Figure 4.2 depicts a typical effective potential between the *centres* of a lock and key, generated from a computer simulation that utilises the geometrical cluster algorithm (GCA) (chapter 2). A brief outline to generate figures like fig. 4.2 proceeds as follows:

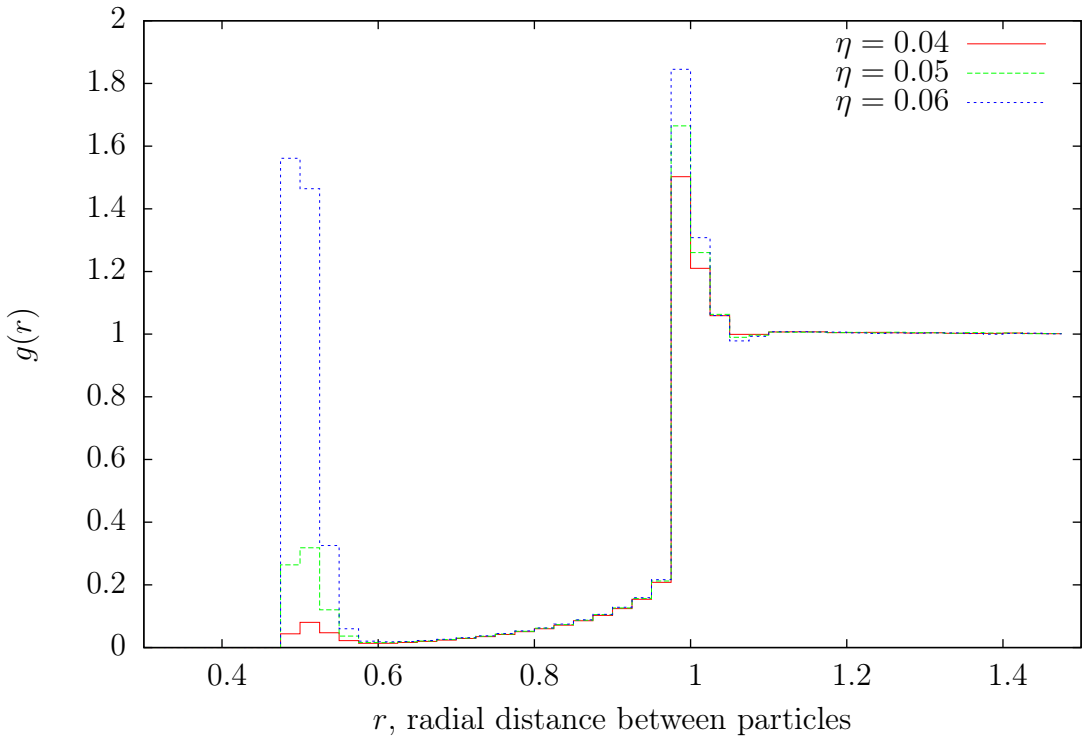

Figure 4.1: Radial distribution functions for different nanoparticle densities, η, of lock and key systems. We note that the peak at $r = 0.5$ corresponds to the bound regime (where the lock and bound to the mouth of the key) whilst the peak at $r = 1.0$ corresponds to the 'back-back' regime where the key touches the lock, but not near the mouth.

1. Run the GCA simulation for a single lock and key system at $\eta = 0.07$ and at $\eta = 0$
2. Construct a two-dimensional histogram of these two simulations in $(r, \cos\theta)$-space to produce two *uncorrected* probability densities, i.e., $\tilde{\mathbb{P}}^{\eta}_{\mathrm{LK}}(r, c)$ and $\tilde{\mathbb{P}}^{\eta=0}_{\mathrm{LK}}(r, c)$
3. Correct these probability densities for finite-size effects as described in eq. (3.11)
4. Finally, take the negative logarithm of the ratio - bin by bin - of $\tilde{\mathbb{P}}^{\eta}_{\mathrm{LK}}(r, c)$ and $\mathbb{P}^{\eta=0}_{\mathrm{LK}}(r, c)$, as described in eq. (3.14) to produce an *approximate* effective potential

We can see three characteristic regions in fig. 4.2:

- A small region of positive attraction situated near the lock mouth which we denote as the *bound* state
- A band of positive attraction located around the edge of the lock
- A repulsive region adjacent to the bound region

We also note that the white regions in fig. 4.2 represent locations where the *centre* of a key cannot exist, relative to a lock. We sketch a lock shape in the centre to aid the eye in this description. Later on, we go on to explain exactly what is meant by $\Delta W^{\eta}_{\mathrm{app}}(r, \cos\theta)$, but for now, it is sufficient to point out that the effective potential shown is a good approximation to the true effective potential. As the number of sampled configurations increases, and the size of the 'bins' in the 2D histogram increases such that the relative statistical uncertainty decreases, one will tend towards the true effective potential.

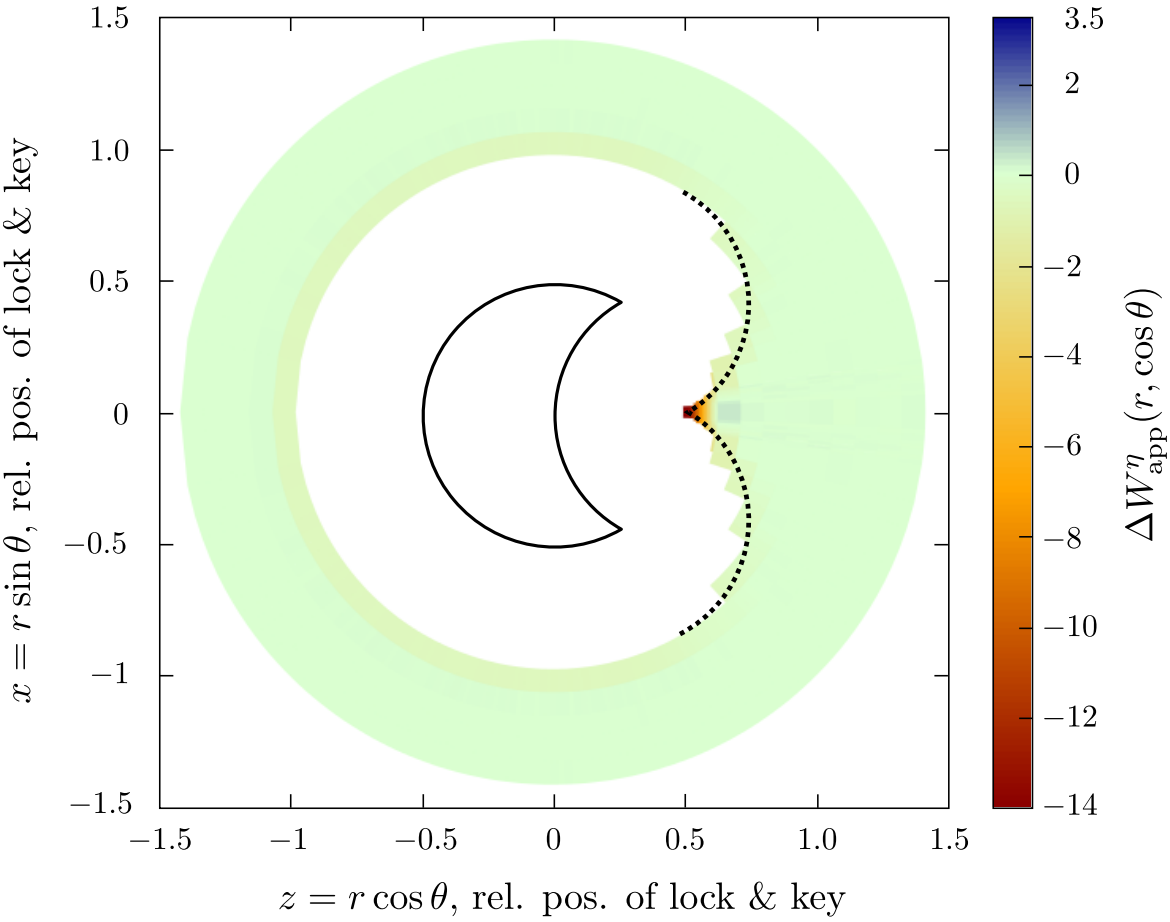

Figure 4.2: Typical $\Delta W^{\eta}_{\mathrm{app}}(r, \cos\theta)$ for a lock and key system. This particular system has parameters of $r_{\mathrm{L}} = r_{\mathrm{K}} = d_{\mathrm{c}} = r_{\mathrm{c}} = 0.5$, $r_{\mathrm{n}} = 0.05$ and $\eta = 0.07$. Despite more than half a billion data points, we still encountered sampling issues that led to noisy data. Therefore, we used large bins for $r > 0.625$ and $\cos\theta < 0.99$.

We will now go on to define these characteristic regions more rigorously, showing their physical original with respect to the geometry of our system, and therefore, the depletion potential.

4.2 Defining Regions of Interest

Looking to a later section, our main motivation is to define an approximate effective potential that captures the key features of fig. 4.2. In order to do this, the first step is to split fig. 4.2 - which typifies an effective potential for a lock and key system - into distinct regions of behaviour. A sketch of how this is done is shown in fig. 4.3, whereby we split the effective potential in terms of different (r, c) regions. A simple example of approximating an effective potential is to imagine replacing an Asakura-Oosawa (AO) effective potential on a sphere with a square well. We are looking for an extension of this to a particular anisotropic particle.

Except for regions D and E, we note that all the regions in fig. 4.3 vary according to the concentration and size of depletant present. Larger and/or a greater number of depletant results in an enhancement of each region's potential. As discussed in chapter 3, these attractive/repulsive phenomena are due to depletion forces, which are a direct result

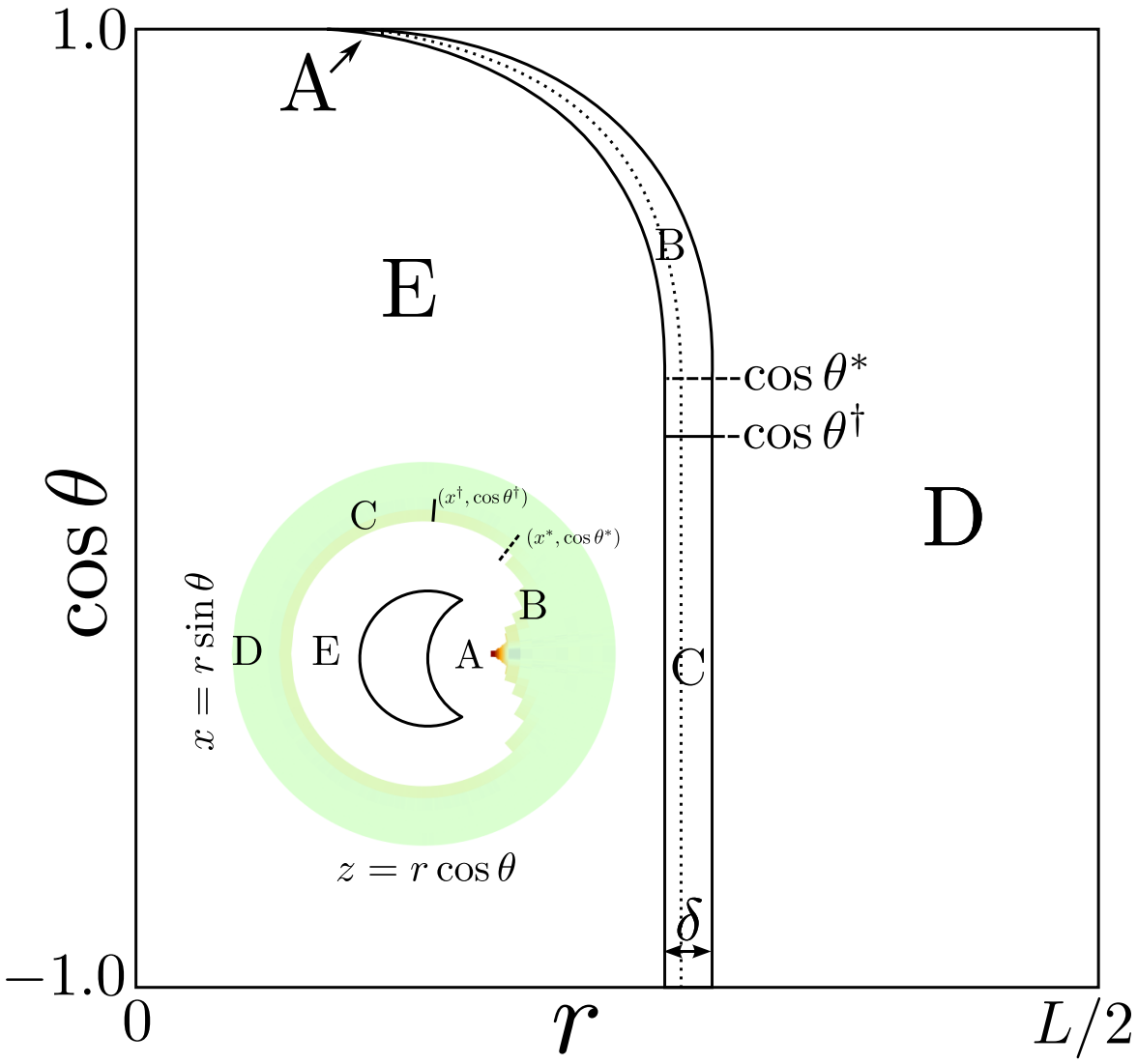

Figure 4.3: Diagram of how $\Delta W^{\eta}_{\text{app}}(r, \cos\theta)$ is split into different regions. We call the regions as follows: A – bound, B – look-up, C – back-back, D – far-field, E – overlap. Regions B and C have a constant width of δ in r only, and are also split via the dotted line into subregions of constant width in r only of $\delta/3$ and $2\delta/3$. Region A is further subdivided into three regions of equal size. We include an inset image of fig. 4.2 to demonstrate how the cylindrical polar coordinates were transformed to $(r, \cos\theta)$-space.

of the system of lock, key and nanoparticles attempting to maximise the total entropy available by maximising the volume available to the nanoparticles. Viewed in this light, we can qualitatively map the colours at any point in fig. 4.2 to the amount of volume gained by the system. The redder the area, the more volume is gained. The more repulsive the effective potential, the less volume is gained. Following on naturally from this, the more negative the effective potential, the more likely a lock and key will have that specific configuration. We can see in fig. 4.2 that the most favourable configuration for system volume gain is the bound pocket.

We can use these general trends which we elaborate further on, along with geometrical arguments to partition the effective potential into regions of distinct behaviour.

4.2.1 Bound Region

As a first step, we note that there is a small region of (r, c)-space where the attraction is strong. This can be observed in the $r = 0.5$ peak of fig. 4.1 and the dark-red point at $(0.5, 0)$ in fig. 4.2. We can approximate this by a constraint on r since the hard-particle criterion subsumes the constraint on theta. Looking back to our arguments of exclusion volume, we see that the point of maximum exclusion volume between a lock and key corresponds to the point of highest inter-particle attraction. To this end, it is sensible to define a small region, fixed by nanoparticle diameters, in radial space as a bound state. Strictly, we define the bound state (region A in fig. 4.3) to be any data point that satisfies

$$r_{\text{closest}} \leq r \leq r_{\text{closest}} + \delta r_{\text{n}} \tag{4.1}$$

where r_{closest} is defined as the smallest possible radial distance between the centres of a key and a lock before overlap occurs. δ is taken as 2.0. We know from the AO case that at sufficiently small nanoparticle packing fractions, any nanoparticle layering will not exceed two layers. This assumption becomes an important length scale in this and upcoming regions.

4.2.2 Back-back Region

For sufficiently low c, the particles interact like spheres and therefore the effective potential is independent of c. From the AO case, we can therefore write a radial criterion as:

$$2r_{\text{L}} \leq r \leq 2r_{\text{L}} + 2r_{\text{n}} \tag{4.2}$$

We also note that at sufficient *angular* position from the lock mouth a change in the potential character occurs. We can therefore write an angular restriction for the back-back region as:

$$\cos\theta^{\dagger} \geq \cos\theta \geq -1.0. \tag{4.3}$$

Taken together, these two conditions encapsulate region C in fig. 4.3. On first inspection, it seems reasonable to use $\cos\theta^{*}$ from fig. 4.3 as the angular restriction, rather than $\cos\theta^{\dagger}$. $\cos\theta^{*}$ is the angle formed by intersection of the line from the *lip* to the centre of the lock and the director pointing straight out of the lock mouth. In terms of location of the key, it can be imagined as placing the key exactly on the tangent of the lip. An example of θ^{*} can be seen in the middle inset image of fig. 4.4. We note with hindsight that effective potential in the back-back region does not fully decouple from the angular component until $\cos\theta^{\dagger}$, i.e., when the key has moved *past* the lip mouth by some amount. Later on, we determine what this amount is from simulation data and show how it connected to a non-trivial variation of exclusion volume. An example of $\theta^{\dagger}$ can be seen in the left inset image of fig. 4.4.

4.2.3 Overlap and far-field regions

Two more regions are needed to partition the $(r, \cos\theta)$ plane. Due to the hard particle criterion, there is a necessary overlap region which particles cannot overlap. There is also a far-field regime where any depletant driven interaction dies away to 0 (fig. 4.4). From fig. 4.3, region E is the forbidden lock-lock overlap region due to the hard lock criterion. Region D, the far-field region, can then be thought of as every state that is not regions A, B, C, or E.

We therefore state that the effective potential in region D is zero, as we are outside the AO limit of two nanoparticle diameters. In region E, the effective potential is essentially infinitely repulsive.

4.2.4 Look-up Region

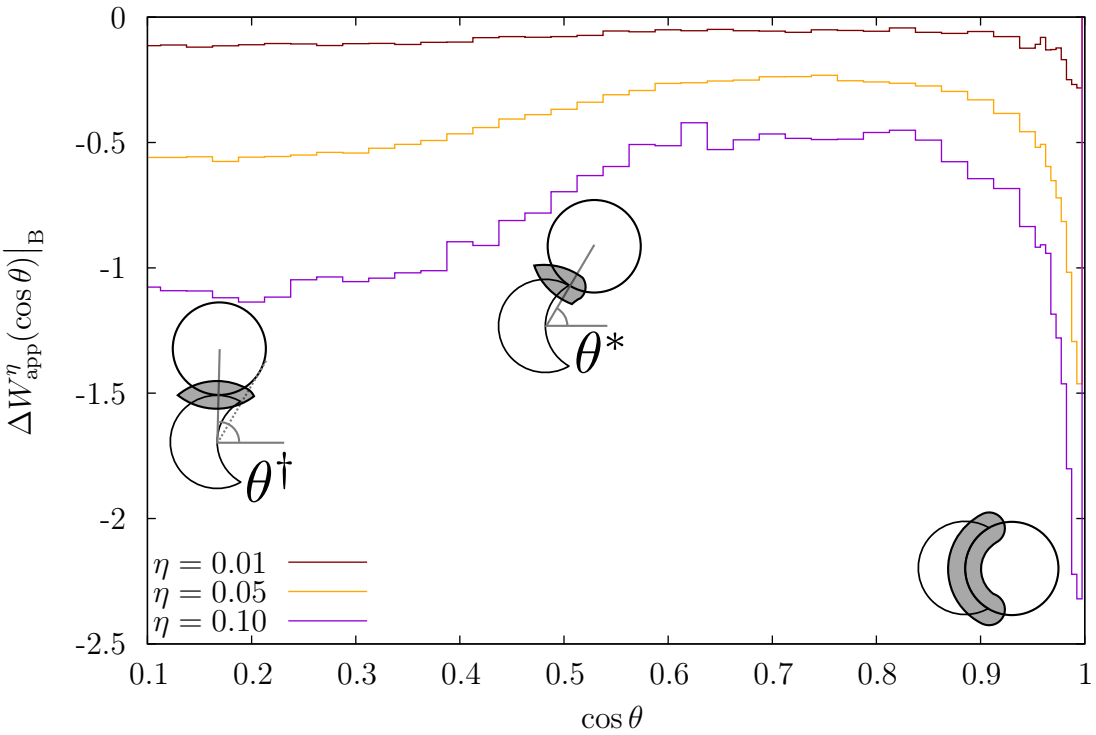

Figure 4.4: Three examples of the lookup effective potential, $\Delta W^{\eta}_{\mathrm{app}}(\cos\theta)\big|_{\mathrm{B}}$. We are confined to region B of fig. 4.3. Despite more than half a billion data points, the look up region remained relatively noisy, therefore each histogram bin for $\cos\theta \leq 0.95$ is five times larger than $\cos\theta > 0.95$. The embedded graphics demonstrate the relatives heights of $\Delta W^{\eta}_{\mathrm{app}}(\cos\theta)\big|_{\mathrm{B}}$. Following a decreasing $\cos\theta$, we see a rise and fall in exclusion volume (shaded area) that correspond to the non-trivial histogram curves. We see a rise in $\Delta W^{\eta}_{\mathrm{app}}(\cos\theta)\big|_{\mathrm{B}}$ close to $\cos\theta = 1$ where the bound region replaces the lookup region (fig. 4.3).

The final region needed to completely partition the effective potential in the $(r, \cos\theta)$-plane is called the look-up region. The name 'look-up' is used with anticipation of the way it will be parametrised in later sections. To describe the effective potential in this region, we make the approximation that ΔW is independent of r; to approximate its dependence on $\cos\theta$, we split the range of $\cos\theta$ in to equal segments of width c_0 and we approximate

the effective potential with each segment by

$$\Delta W^{\eta}_{\mathrm{app}}(\cos\theta)\big|_{\mathrm{B}} = -\log\left[\frac{\int_{r_{\mathrm{in}}}^{r_{\mathrm{out}}}\int_{c}^{c+c_0}\mathrm{d}r\mathrm{d}\cos\theta\mathbb{P}^{\eta}_{\mathrm{LK}}(r,\cos\theta)}{\int_{r_{\mathrm{in}}}^{r_{\mathrm{out}}}\int_{c}^{c+c_0}\mathrm{d}r\mathrm{d}\cos\theta\mathbb{P}^{\eta=0}_{\mathrm{LK}}(r,\cos\theta)}\right]. \tag{4.4}$$

The result is shown in fig. 4.4. With reference to fig. 4.3, $\cos\theta^{*} = 0.5$ and $\cos\theta^{\dagger} = 0.1$. We can justify the choice of using $\cos\theta^{\dagger}$ instead of $\cos\theta^{*}$ by inspecting the sketched exclusion volumes. It is not until $\cos\theta = \cos\theta^{\dagger} = 0.1$ that the exclusion volume looks like the hard-sphere case. We also typically see the least attractive region in the range of $0.7 \lesssim \cos\theta \lesssim 0.8$. This can be attributed to a reduced ΔV, as indicated in fig. 4.4.

Strictly speaking, the left boundary of region B in fig. 4.3 corresponds to the closest approach of the key to the lock at fixed θ. This is given by

$$\begin{gathered} z_{\mathrm{b}}r + x_{\mathrm{a}}\sqrt{1-c^2} = \frac{x_{\mathrm{a}}^2 + z_{\mathrm{b}}^2 + r^2 - r_{\mathrm{L}}^2}{2r} \ \text{ if } c > \cos\theta^{\dagger}, \\ r = 2r_{\mathrm{L}} \ \text{ otherwise.} \end{gathered} \tag{4.5}$$

Equally, the right boundary of region B is defined as

$$\begin{gathered} z_{\mathrm{b}}r + x_{\mathrm{a}}\sqrt{1-c^2} = \frac{x_{\mathrm{a}}^2 + z_{\mathrm{b}}^2 + r^2 - (r_{\mathrm{L}}+\delta)^2}{2r} \ \text{ if } c > \cos\theta^{\dagger}, \\ r = 2r_{\mathrm{L}} + \delta \ \text{ otherwise.} \end{gathered} \tag{4.6}$$

In both eqs. (4.5) and (4.6), $(x_{\mathrm{a}}, z_{\mathrm{b}})$ is the location of the 'lip' or 'point' of the lock in Cartesian cooordinates. We must solve for the radial coordinate, r, in these two equations.

We have now developed a sensible series of partitions with which to categorise different regions of behaviour in the $(r, \cos\theta)$ representation of the effective potential of a lock and key system. We have justified these choices with geometrical arguments with depletion-based vocabulary. We will now go on to interpret the free energy predictions that were developed in chapter 3. We aim to show that these predictions are a useful metre-stick in the parametrisation process.

4.3 Free energy versus well depth

Firstly, the well depth for any given region (e.g., fig. 4.3) is the value of the effective potential, whilst the free energy is the integral.

We must be careful about discussing absolute values as the choice of normalisation in the equilibrium constant, $\mathcal{K}$ in eq. (3.47) leads to a corresponding shift in the free-energy curve of fig. 4.5. However, we know that the reciprocal of $\mathcal{K}$, $\mathcal{K}^{-1}$, has units of density, and if the density of locks and density of keys, ρ_{L} and ρ_{K}, are both equal to the $\mathcal{K}^{-1}$, then the density of bound lock and keys, ρ_{B} is also equal to $\mathcal{K}^{-1}$, by definition of the equilibrium constant in eq. (3.35). Therefore, under these assumptions, half of the locks and keys would

be bound. One can then think of $\mathcal{K}^{-1}$ as approximately the *density of locks and keys* at which binding becomes important. Further, if $V_\sigma/\mathcal{K}$ is a small number, we obtain a good estimate of the packing fraction of locks and keys at which one would observe chaining behaviour, as described by Ashton et al. [1], for any η. We can therefore remark that the higher the packing fraction of nanoparticles, the lower the density of locks and keys are needed for any self-assembled aggregates to form.

Figure 4.5 plots the binding and back-back free energy, ΔF_{B} and ΔF_{BB}, as normalised by the unit volume of the system, against the nanoparticle density, η.

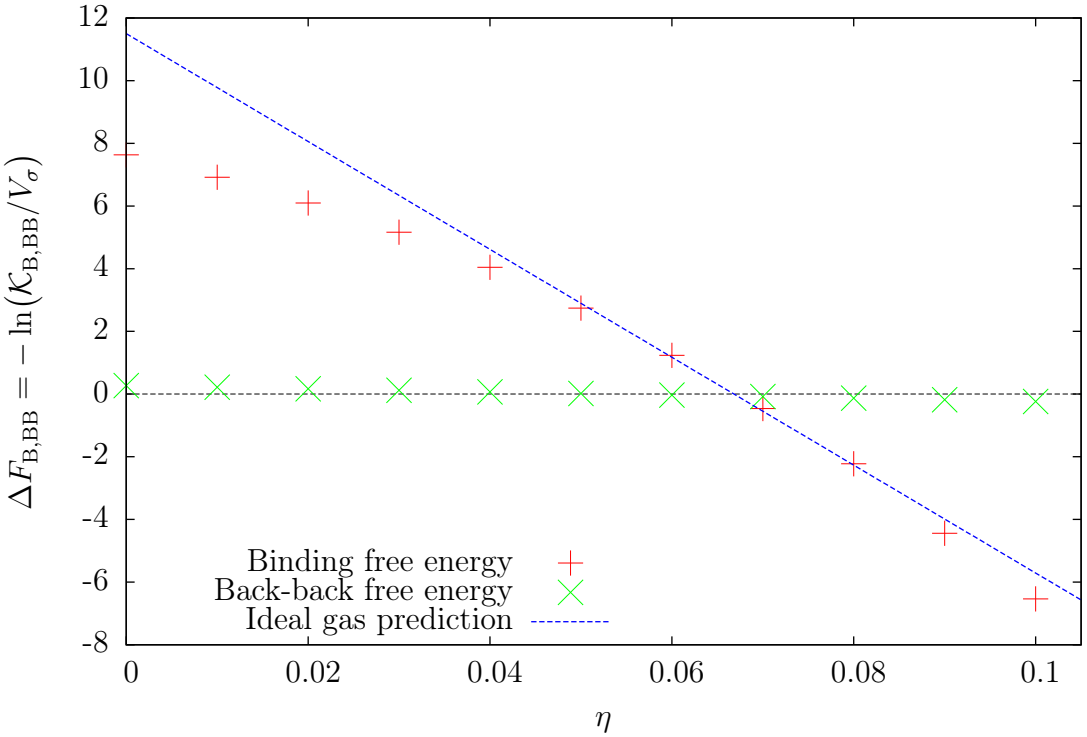

Figure 4.5: Binding and back-back free energy versus η of a lock and key system. We are able to make a prediction of the binding free energy of a lock and key, using the standard ideal gas pressure, giving a gradient, $\Delta V/V_{\mathrm{n}}$, of $\sim$172 (3 s.f.) [$\Delta V \sim 0.0901$ for $r_{\mathrm{c}} = d_{\mathrm{c}} = r_{\mathrm{K}} = r_{\mathrm{L}} = 0.5$] and an intercept with the ordinate-axis, $-\ln(V_{\mathrm{B}}/\sigma)$, of $\sim$10.8 kT (3 s.f.). We sketch a line at a binding free energy of zero to demonstrate that the back-back free energy decreases very slightly with increasing η.

We can see that the binding free energy, ΔF_{B}, does not become more favourable than the back-back free energy ΔF_{BB} until $\eta = 0.07$ which is a result of the punishingly low number of configurational states that inhabit the bound region compared to the vast number of back-back states. η must be above a certain value before the depletion force is strong enough for $\Delta F_{\mathrm{B}} < \Delta F_{\mathrm{BB}}$. This balance is further evidenced by fig. 4.6, where the increasing density of nanoparticles causes the well depth of the subdivided bound regions to increase more quickly than the subdivided back-back regions. Indeed, even within bound sub regions, we see that the rate of increase is proportional to the key and lock's radial proximity. In fig. 4.5, we also plot the ideal gas free energy prediction eq. (3.47), as derived from the partition function of a single lock and key system with AO particles in section 3.4. We have explicitly calculated the exact three-dimensional exclusion volume, ΔV, and found it to be ~ 0.0901. We refer to Appendix A for an approximate, much simpler method to calculate

the exclusion volume. We note that the departure of the simulation data to the prediction is due to there being insufficient depletion force to confine the key into the lock mouth. We had an assumption that the binding pocket volume - the point-like region in which a key would bind perfectly to a lock - is invariant to nanoparticle density due to the osmotic force of the nanoparticles pushing the key into the lock mouth. At lower nanoparticle densities, the binding pocket volume can no longer be constant and so our prediction fails in this regime ($\eta \lesssim 0.06$). Thus, we might correct for this by relaxing the constant binding pocket volume assumption. One must choose a radial cut off for the binding pocket volume that depends non-trivially on the nanoparticle density.

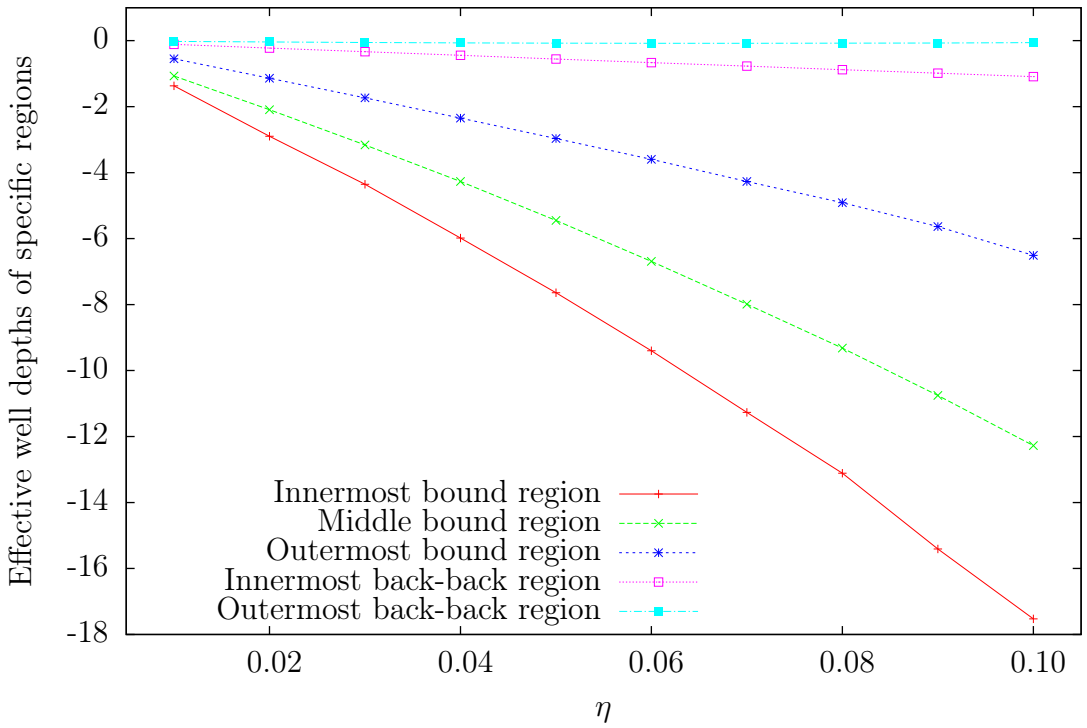

Figure 4.6: Well depth, for varying η of selected regions in fig. 4.3. By effective well depths, we mean the value of the effective potential in fig. 4.3. For example, the innermost bound region at arbitrary η will have a well depth expressed as $\Delta W^{\eta}_{\text{app}}\big|_{\text{A1}}$, where $A1$ refers to the innermost, or left most, bound region in fig. 4.3.

4.4 Parametrisation of Effective Potential

The general strategy to parametrise the effective potential can be visualised as follows: superimpose a tiling that fits exactly over the regions as shown in fig. 4.3. For example, in region B, our tiles would be constant in $\cos\theta$ but a large number of them will cover the whole region vertically. For each tile, we then construct a "piecewise constant" approximate effective potential that is roughly equivalent to the true effective potential. If our tiles were infinitesimally small, then this "piecewise constant" approximate effective potential will tend to the true effective potential. Later on, in the two-lock system, we will formalise the definition of the piecewise constant approximate effective potential.

Accordingly, to parametrise the lock and key effective potential for any given statepoint,

we separated computer simulation data into different regions as listed in section 4.2. For each region, we produced approximate effective potentials. We made deliberate choices to either include explicitly or integrate out specific coordinates. Our method of integrating out the effective potential ensures that there is good parity (a few percent) between second virial coefficients [69, 72] of the real effective potential and the resultant parametrised effective potential.

4.4.1 Back-back & bound regions

Analysis of the back-back and bound regions indicates a slowly varying effective potential. They can therefore be partitioned into sub-regions. For the back-back case, we have chosen two sub-regions in r-space and for the bound region, we have chosen three regions.

4.4.2 Overlap region & far-field regions

The overlap region, by definition, has infinite repulsion. In practice, this is just represented by algorithmically forbidding a key to penetrate a lock. For the far-field region, we have, by definition, neither attraction or repulsion. This was verified before encoding into the algorithm.

4.4.3 Lookup region

The 'look-up' region in the $(r, \cos\theta)$ representation of the effective potential (fig. 4.2) is unique for its use of tabulated values rather than parametrised equations. Figure 4.4 demonstrates the potential in the 'look-up' region for three different values of η. Specifically, it plots the potential along the curved path of fig. 4.3 so that any $\cos\theta$ corresponds to a unique radial coordinate. The inset 2D figures of the lock and key demonstrate the qualitative rise-fall of $\Delta W^{\eta}_{\mathrm{app}}(\cos\theta)\big|_{\mathrm{B}}$ with changing $\cos\theta$. From largest to smallest $\cos\theta$, we see that the excluded volume (shaded area) is correlated to the size of $\Delta W^{\eta}_{\mathrm{app}}(\cos\theta)\big|_{\mathrm{B}}$. We note that the rise in potential, corresponding to the middle figure is located at the point where the key is on a point of 'inflexion' with the tip of the 'lock mouth'. This point of inflexion can be seen as the key rolling around the lock has a smaller exclusion volume than the left and right-most inset image. Rather than quantify the shape of fig. 4.4 – which would involve calculating the complicated exclusion volume between $\cos\theta = 0.1$ and 1.0 – the data from long running GCA simulations was instead tabulated. For the same reason that the bound region was partitioned into three equal sections in r-space, the lookup-region was also partitioned into two regions. One region, closest to the left hand side of the bound region is one third of radial width of $2r_{\mathrm{n}}$ whilst the larger segment is then obviously two-thirds of the radial width of $2r_{\mathrm{n}}$.

4.5 Typical Parametrised Effective Potential

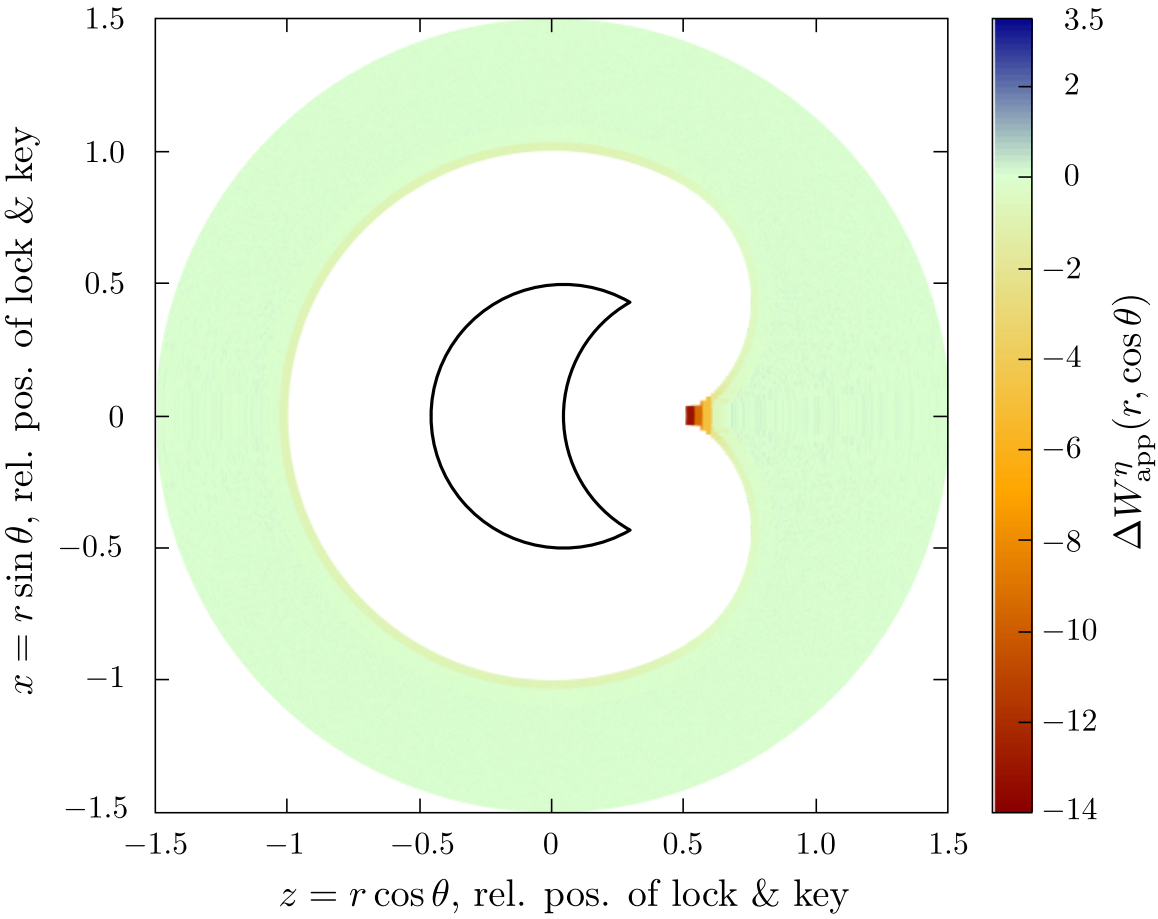

Figure 4.7: Typical effective potential, $\Delta W^{\eta}_{\mathrm{app}}(r, \cos\theta)$, generated using the parametrised effective potential of a lock and key system with parameters $r_{\mathrm{L}} = r_{\mathrm{K}} = d_{\mathrm{c}} = r_{\mathrm{c}} = 0.5$, $r_{\mathrm{n}} = 0.05$ and $\eta = 0.07$. The data set used to generate the parametrised effective potential, which was used to generate this diagram corresponds to real effective potential in fig. 4.2. As opposed to fig. 4.2, this 2D histogram is shown with bins that are constant in r and $\cos\theta$.

Figure 4.7 depicts a typical effective potential in the $(r, \cos\theta)$ plane. We point out that fig. 4.7 is an actual measurement, generated from applying the GCA simulation *without* nanoparticles but with partitioned regions as discussed in the previous section, rather than a measurement from a GCA with explicit nanoparticles, as shown in fig. 4.2. We note the excellent parity with fig. 4.2. Here, we can state that the parametrised effective potential coupled with a GCA simulation results in at least an order of magnitude reduction in simulation time. As such, there is much weight to the idea that a "colloid is trapped by a cage of nanoparticles for long times" in explicit nanoparticle Monte Carlo simulation (chapter 2).

This is further bolstered by the excellent sampling of configuration space in the parametrised effective potential. A numerical comparison of relevant effective potentials also indicates an excellent parity to the third significant figure. We also plot effective well depths of specific regions as a function of nanoparticle density. By effective well depths, we mean the integrated potentials across the equivalent regions in fig. 4.3. For example, the innermost bound region at arbitrary η will have an integrated well depth expressed as $\Delta W^{\eta}_{\mathrm{app}}\big|_{\mathrm{A1}}$,

where $A1$ refers to the innermost, or left most, bound region in fig. 4.3. These values are explicitly used in our parametrisation scheme. We see, as expected and mentioned earlier, that the depletion interaction depends on nanoparticle density. What is unclear and a major drive for the development of the parametrisation of the effective potential is the exact dependence of these well-depths on η. It is clear that these curves will be different for every different geometry. A fully quantitative prediction of the effective well depth remains out of the scope of this thesis.

4.6 Mismatched Lock & Key

In the previous section, we laid out a reasonable strategy for simplifying the effective potential of an *exactly* fitting lock and key potential and presented a proof-of-concept parametrised effective potential generated from real, nanoparticle-less simulations. Here we discuss a more general case of lock and key, where the lock and key are mismatched (sometimes called inexactly fitting). This is another important step in completely describing a general lock and key system. The first ever experiment performed on lock and keys used mismatched lock and keys too [38], so it is reasonable for simulation to make this bridge with experiment.

As before, we first discuss a typical effective potential for this system. For system details, we refer to chapter 4, with the single adjustment that $r_c = 0.7$ instead of 0.5. We recall that r_c is the radius of a sphere a distance d_c away from the centre of a sphere of the same radius as a lock, such that the intersection between the two spheres defines the mouth of the lock (fig. 1.4).

4.6.1 Typical Effective Potential

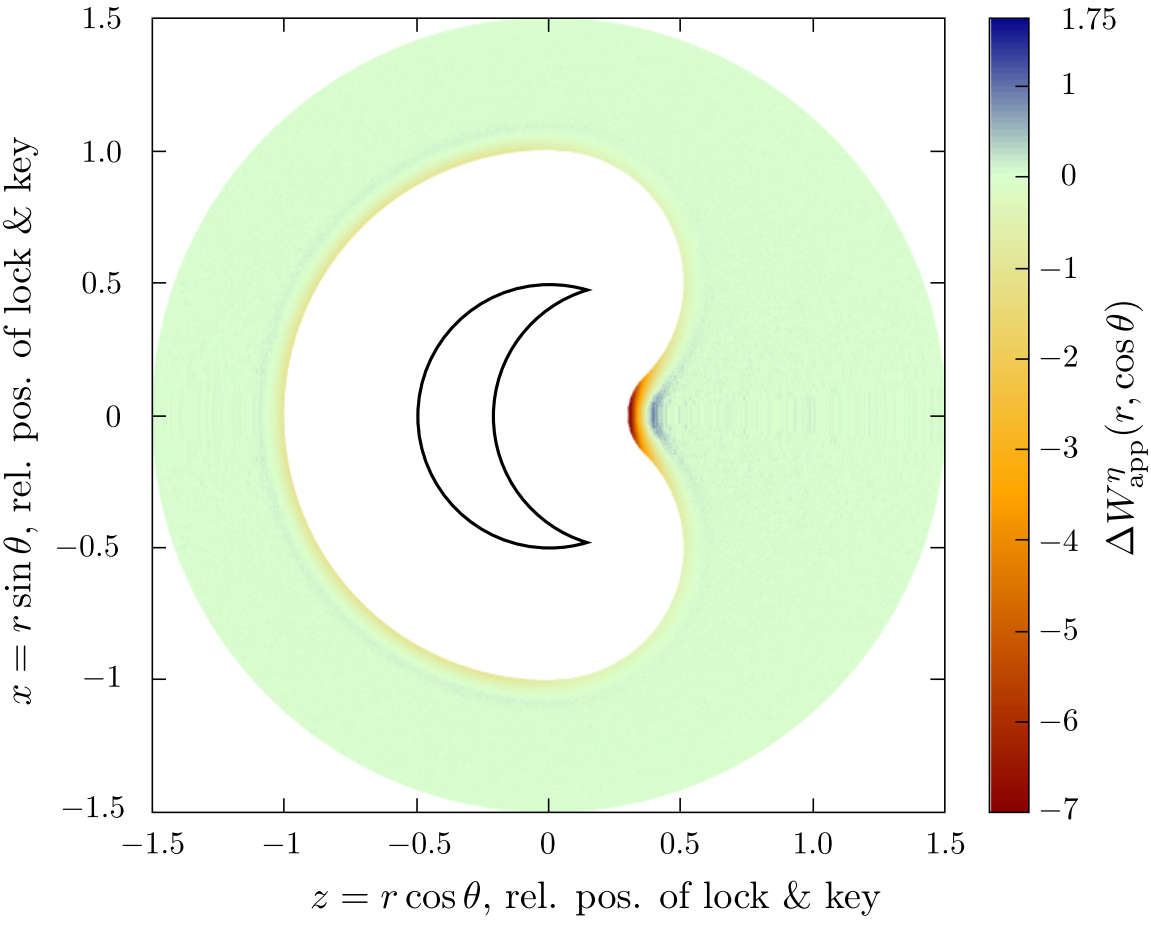

Figure 4.8: Typical $\Delta W^{\eta}_{\mathrm{app}}(r, \cos\theta)$ for a mismatched lock and key system. This particular system has parameters of $r_L = r_K = d_c = 0.5$, $r_c = 0.7$, $r_n = 0.05$ and $\eta = 0.07$. As opposed to the exact fitting case, fig. 4.2, this histogram is shown with bins that are constant in r and $\cos\theta$.

We do not show the equivalent radial distribution functions for the mismatched lock

and key system, but point to the exactly matched system in fig. 4.1 and state that the equivalent $g(r)$ is qualitatively similar, with a peak at the distance of closest approach between a lock and key in the lock mouth equal to, in this instance, $r = 0.3$, and a peak where the key is touching the lock but away from the key-mouth. The former will, as before, be known as the 'bound' regime whilst the former will be known as the 'back-back' regime.

Figure 4.8 is a typical effective potential for a mismatched lock and key, generated from a computer simulation. As before, we see that the full, two-dimensional effective potential includes a radial as well as an orientational dependence between a lock and a mismatched key. It should be clear that the orientational dependence of a radial distribution function is not obvious, but again, must be inferred from geometrical knowledge of a lock and key system. Unsurprisingly, we see similar regions of interest to the simpler exactly fitting lock and key (fig. 4.2). Compared to the simpler case study, we observe

- A larger region of attractive potential, due to a greater number of configurations with comparable binding free energy,
- A new band of repulsive potential around the back of the lock due to nanoparticle layering,
- A larger region of repulsive potential due to the enhancement of nanoparticle layering inside the lock mouth.

As before, the white regions in fig. 4.2 represent locations where the centre of a key cannot exist, relative to a lock. We sketch a lock in this figure to aid the eye. Following the same prescription, we go on to define these characteristic regions more rigorously. We find that their physical origin is very similar to the exactly fitting regime but with extra complications of mathematically precise definitions of the equivalent regions.

4.6.2 Defining Regions of Interest

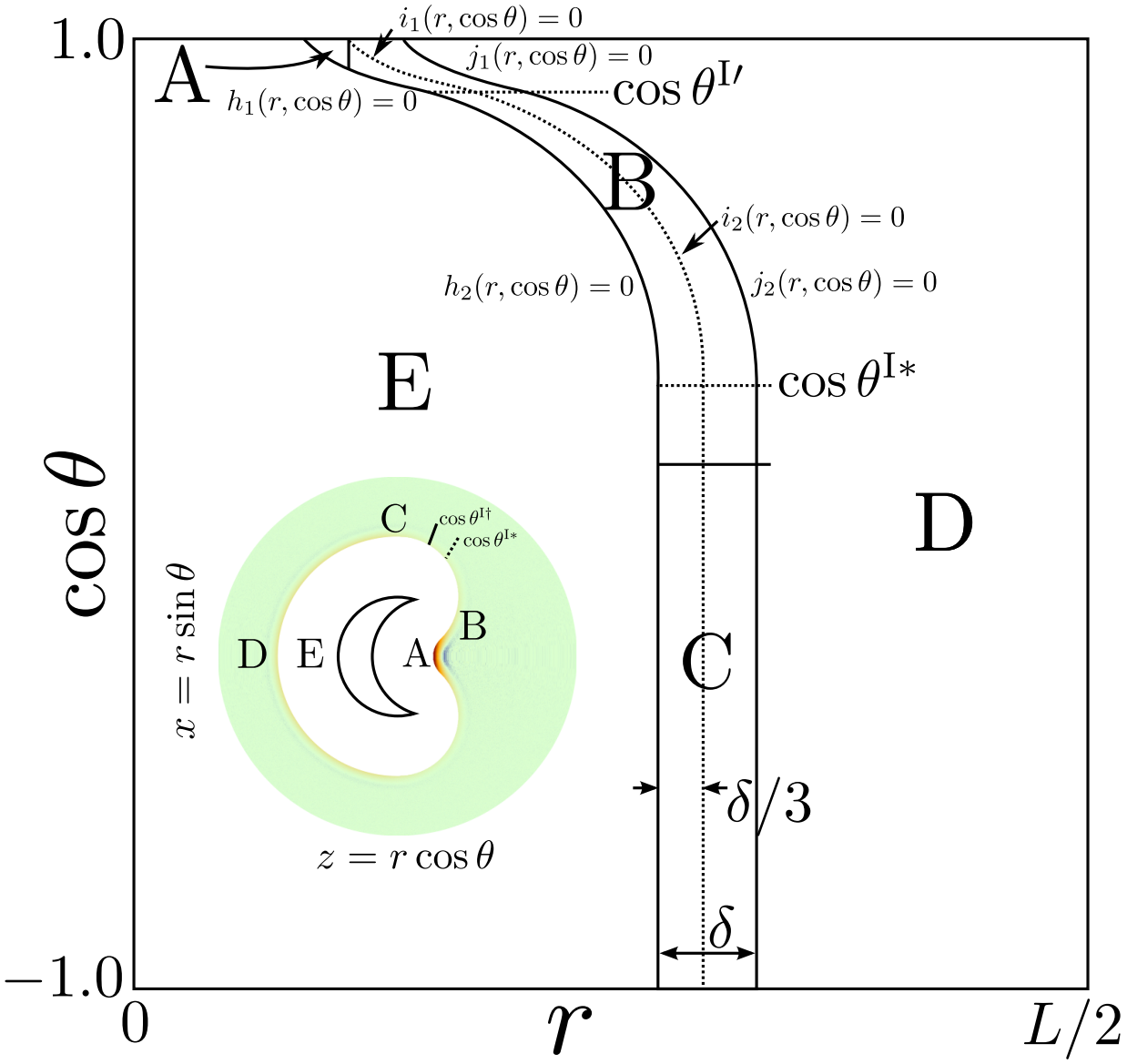

Figure 4.9: Typical sketch of how $\Delta W^{\eta}_{\mathrm{app}}(r,\cos\theta)$ for a mismatched lock and key is split into separate regions. We call the regions as follows: A – bound, B – look-up, C – back-back, D – far-field, E – overlap. Regions B and C have a constant width of δ in r only, and are also split into subregions of constant width in r only of $\delta/3$ and $2\delta/3$. The functions h_1, i_1 and j_1 begin at $\cos\theta = 0$ and terminate at $\cos\theta = \cos\theta^{\mathrm{I}\prime}$, while the functions h_2, i_2 and j_2 begin at $\cos\theta = \cos\theta^{\mathrm{I}\prime}$ and terminate at $\cos\theta = \cos\theta^{\mathrm{I}*}$. We include an inset image of fig. 4.8 to demonstrate how the cylindrical polar coordinates were transformed to $(r,\cos\theta)$-space. It is helpful to compare this sketch to the simpler sketch of fig. 4.3.

As before, our main motivation for partitioning the effective potential is to define an approximate effective potential that captures the key features of fig. 4.8. We split this figure - which typifies an effective potential for a *mismatched* lock and key system - into distinct regions of behaviour. A sketch of how this is done is shown in fig. 4.9, where we have split the effective potential into different regions. We point to the discussion in section 4.2 for a general explanation of the repulsive/attractive regions.

The general trends observed in a typical mismatched lock and key effective potential can be used as guidance for how to proceed with parametrisation. We use the language

and concepts developed in the exactly fitting lock and key case to aid us. We can again use functions in the $(r, \cos\theta)$ plane - based on geometrical arguments - to partition the effective potential into regions of distinct behaviour.

Bound region

As for the exact lock and key case, the point of maximum exclusion volume between a lock and key corresponds to the point of highest inter-particle attraction (fig. 4.8). To this end, it is sensible to define a small region (region A in fig. 4.9) in radial space as a bound state. We still strictly define the bound state to be any data point that satisfies

$$r_{\text{closest}} \leq r \leq r_{\text{closest}} + \delta r_{\text{n}} \tag{4.7}$$

where r_{closest} is defined as the smallest possible radial distance between the centres of a key and a lock before overlap occurs. δ is taken as 2.0. The bound region is *not* sub-divided into sub-regions for the mismatched case. We do not need to include an angular constraint as the hard-particle criterion subsumes it.

Back-back & Look-up Region

We can still identify two regions of distinct behaviour in the band of positive attraction located around the edge of the lock. As before, the back-back region is located for $\cos\theta$ less than 0.1 whilst the look-up region is for $\cos\theta$ greater than 0.1. We refer to the discussion in sections 4.2.2 and 4.2.4 that remains valid for this mismatched lock and key case. Therefore, we define the back-back region as

$$\cos\theta \leq \cos\theta^{\text{I}*} \tag{4.8}$$

and

$$2r_{\text{L}} \leq r \leq 2r_{\text{L}} + \delta. \tag{4.9}$$

Figure 4.11 depicts the mismatched look-up region's effective potential, which can be compared to fig. 4.4. We can see from the changing exclusion volume in this figure that, like the exact case, there is a clear reason to separate the band of positive attraction into two sections. The look-up region can be seen in fig. 4.9. Their equations (which can be compared to the simpler eqs. (4.5) and (4.6)) are given as:

$$h_1(r, \cos\theta) = \frac{r^2 + d_{\text{c}}^2 - (r_{\text{c}} - r_{\text{L}})^2}{2r} - d_{\text{c}}\cos\theta \tag{4.10a}$$

$$h_2(r, \cos\theta) = \frac{r^2 + (z^{\triangleright})^2 + (x^{\triangleright})^2 - r_{\text{L}}^2}{2r} - z^{\triangleright}\cos\theta - x^{\triangleright}\sqrt{1 - \cos^2\theta} \tag{4.10b}$$

where $(z^{\triangleright}, x^{\triangleright})$ is the Cartesian center of a key on the 'lip' of the lock mouth, as demonstrated in fig. 4.10. For the corresponding i functions, we make the substitution of $r \to r + \delta/3$. For the corresponding j functions, we make the substitution $r \to r + \delta$. The physical motivation for eqs. (4.10a) and (4.10b) stem from considering the closest approach of a key

to a larger lock mouth. One will relax the convex shape of region B in fig. 4.3 and develop two part concave-convex shape of region B in fig. 4.9.

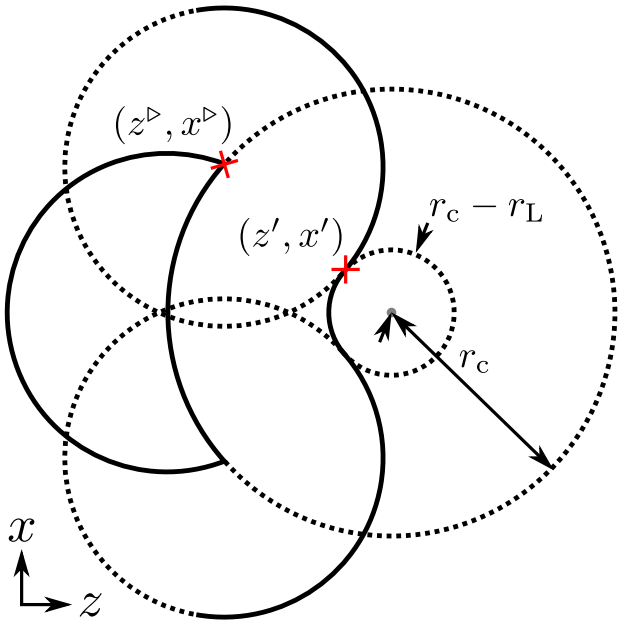

Figure 4.10: The middle black curve demonstrates the 2D representation of the closest approach of a mismatched lock and key. (z', x') is the circle-circle intercept between the Cartesian representation of eq. (4.10a) and eq. (4.10b). $(z^{\triangleright}, x^{\triangleright})$ is the Cartesian center of a key on the 'lip' of the lock mouth.

Overlap and Far-field Region

There is no change in explanation of the overlap and far-field regions. We refer to section 4.2.3, but point to fig. 4.9 instead of fig. 4.3 to explain the mismatched lock and key regions.

4.6.3 Parametrisation of Effective Potential

In the same fashion as section 4.4, we parametrised the lock and key effective potential for any given statepoint by separating computer simulation data into different regions. For each region, we produced approximate effective potentials. We made deliberate choices to either include explicitly or integrate out specific coordinates. Our method of integrating out the effective potential ensures that there is good parity (a few percent) between second virial coefficients [69, 72] of the real effective potential and the resultant parametrised effective potential. The look-up region for the mismatched lock and key is worthy of note, as its region of highest attraction appears as a dip at $\cos\theta \approx 0.96$ in fig. 4.11. We ascribe this dip to the $\cos\theta$ cut off of the bound region, as shown in the inset diagram.

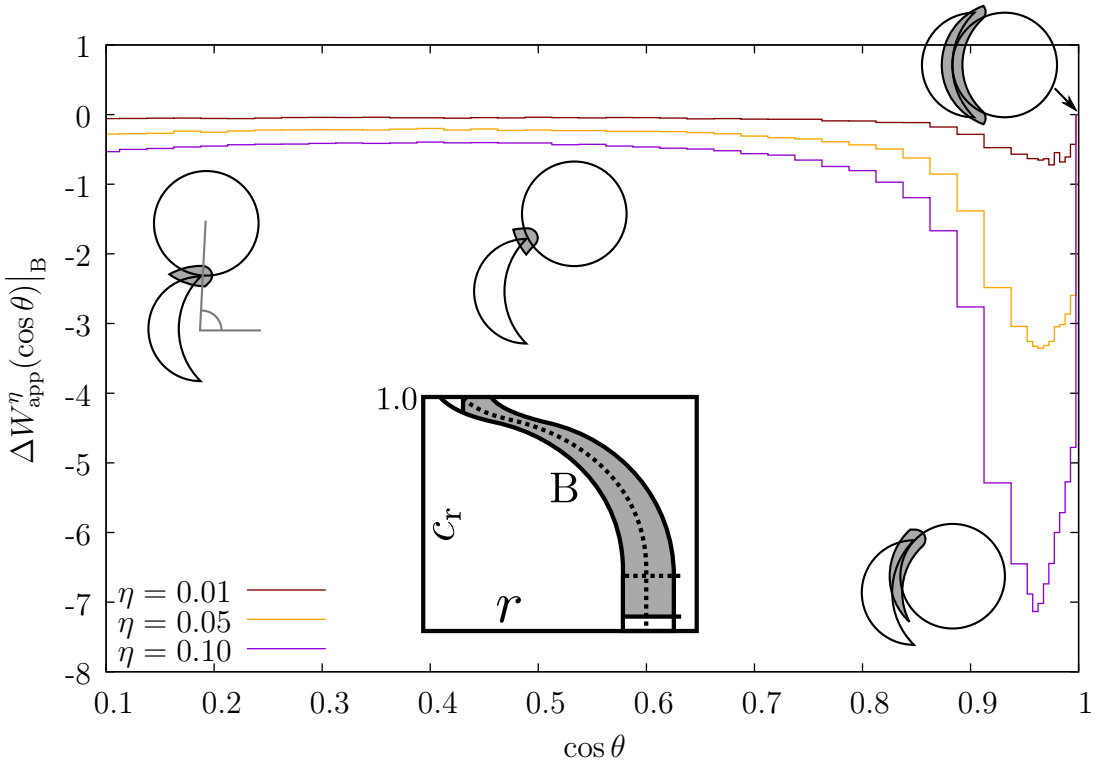

Figure 4.11: Three examples of tabulated data used in the effective potential algorithm, look up region. The major difference from the matched case, fig. 4.4, is the rise in $\Delta W(\cos\theta)$ after about $\cos\theta = 0.96$. We can attribute this to an enhanced bound region compared to the exact case, as shown in the inset figure.

4.6.4 Typical Parametrised Effective Potential

Figure 4.12 depicts a typical effective potential for the mismatched lock and key in the $(r, \cos\theta)$ plane. There is a good visual parity with the real potential in fig. 4.8 and, within the separate regions, an excellent numerical parity. The absent repulsive region near the mouth in this parametrised potential is consistent with the approximation that the far-field regime is neither repulsive or attractive. This approximation could be improved by tabulating the values in this region for use in a parametrised effective potential. Of particular note is the difference between the attraction in the bound pocket of the real potential and the parametrised. We can ascribe the greater pocket of 'medium' attraction in the parametrised potential to the purely radial cut off criterion in eq. (4.7) - which we preserved from the exactly fitting lock and key, leading to a 'smearing' out of the potential over a greater area. A truer criterion would have been to include some angular component. We drew the line of accuracy versus simplicity here.

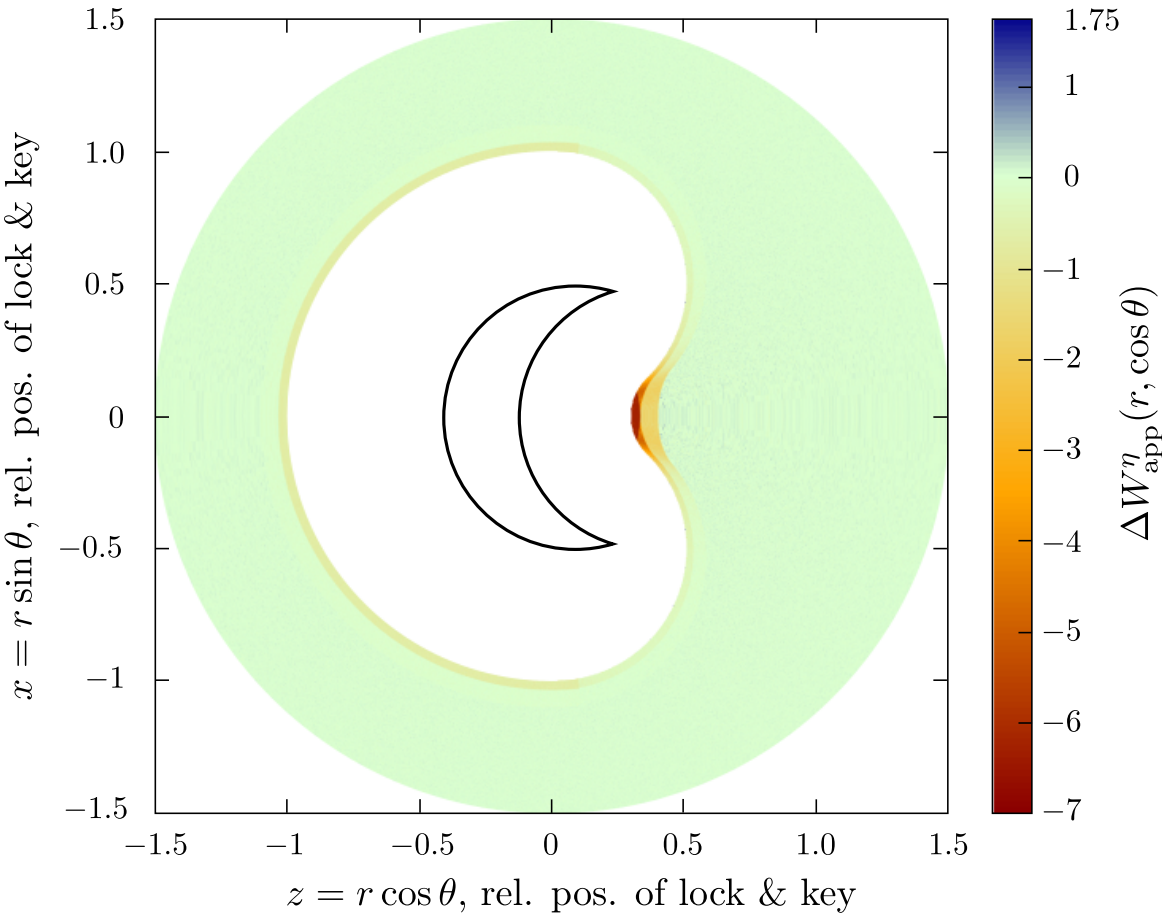

Figure 4.12: Typical parameterised $\Delta W^{\eta}_{\mathrm{app}}(r, \cos\theta)$ for a lock and key system. This particular system shares the same properties as fig. 4.8, i.e., $r_{\mathrm{L}} = r_{\mathrm{K}} = d_{\mathrm{c}} = 0.5$, $r_{\mathrm{c}} = 0.7$, $r_{\mathrm{n}} = 0.05$ and $\eta = 0.07$. This parametrised potential was generated from the data that created fig. 4.8.

4.7 Comparing Mismatched to Exact Lock and Key

It should, by now, be clear that only a few modifications of the exact lock key parametrisation process are needed to parametrise the mismatched case. The only major change is that the bound region is not subdivided. Analysing equivalent regions in the mismatched case leads to some interesting conclusions. Comparing free energy curves, fig. 4.5 and fig. 4.13, we can see that depletion potential in the mismatch case is, at equivalent packing fractions, less attractive (at $\eta = 0.10$, the mismatched $\Delta F_{\mathrm{B}} \approx -1.5$ compared to the exact $\Delta F_{\mathrm{B}} \approx -6.3$). Further to this, the mismatched well depth achieves a significantly lower attraction at all η above 0 (compare fig. 4.6 and fig. 4.14). In terms of phenomenology, a mismatched lock and key will have decreased self-assembling ability, in agreement with the experiments performed by Sacanna et al. [38]. Making a geometric argument, we can attribute the decreased self-assembly to a decrease in maximal exclusion volume gained in the bound region (mismatched exclusion volume, $\Delta V \approx 0.09$, exact $\Delta V \approx 0.05$). We can observe this in the right most inset images of fig. 4.4 and fig. 4.11. More subtly, as mentioned by Odriozola et al. [46], the lock mouth enhances the layering of nanoparticles, causing a patch of repulsion that a colloid must overcome before docking with the lock mouth. This effect is not visible (at least between $\eta = 0.01$ and $\eta = 0.10$) for the exactly

bound case - fig. 4.2 - but is visible for the mismatched case at $\eta = 0.07$ (fig. 4.8). A greater proportion of the surface area of the lock is devoted to the mouth for the mismatched case, leading to a greater proportion of nanoparticles taking part in this enhanced layering effect. Curiously, this larger mouth would also lend itself to easier key docking, only with reduced permanency due to a weaker potential.

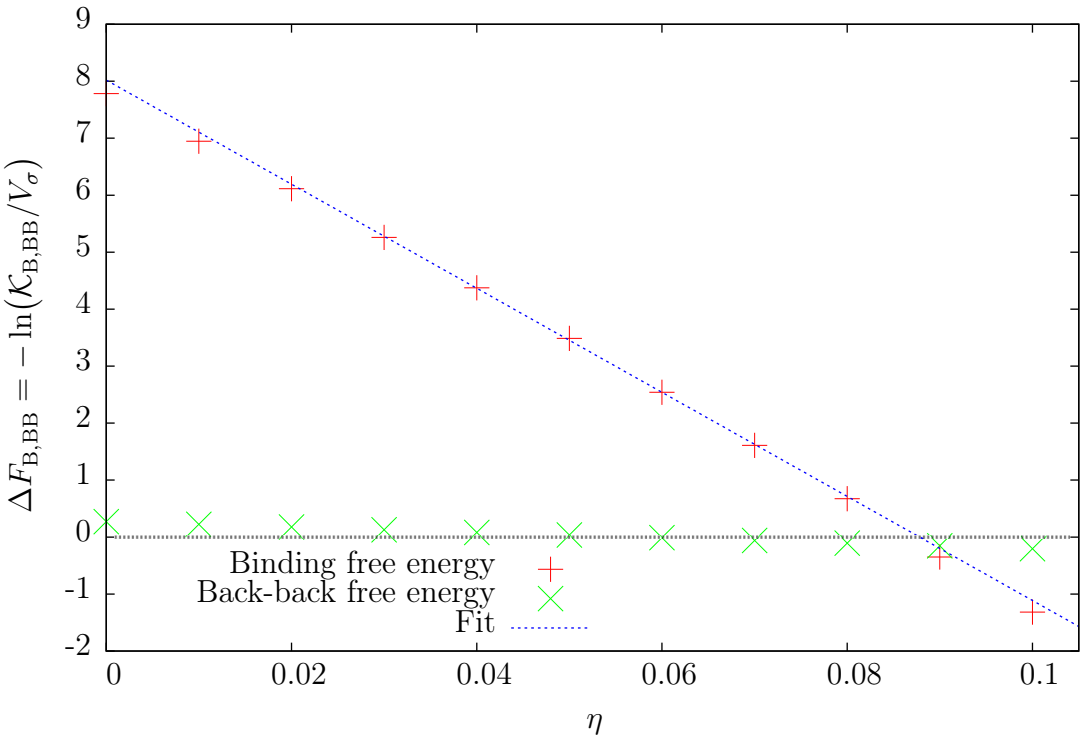

Figure 4.13: Binding and back-back free energy vs. η, compare to fig. 4.5, but with a mismatched lock and key. A line of best fit for ΔF between $\eta = 0.03$ and $\eta = 0.07$ has a gradient, ${}^{\Delta V}/_{V_\sigma}$ of $\sim$91 and an intercept on the ordinate axis, $-\ln({}^{V_\mathrm{B}}/_{V_\sigma})$, of $\sim 8kT$. The gradient leads to a mismatched exclusion volume, ΔV, of ~ 0.05 for $r_\mathrm{c} = 0.7$, $d_\mathrm{c} = r_\mathrm{K} = r_\mathrm{L} = 0.5$ and $r_\mathrm{n} = 0.05$. This seems to be the same order of magnitude as the exactly matched exclusion volume. We sketch a line at a binding free energy of zero to demonstrate that the back-back free energy decreases very slightly with increasing η.

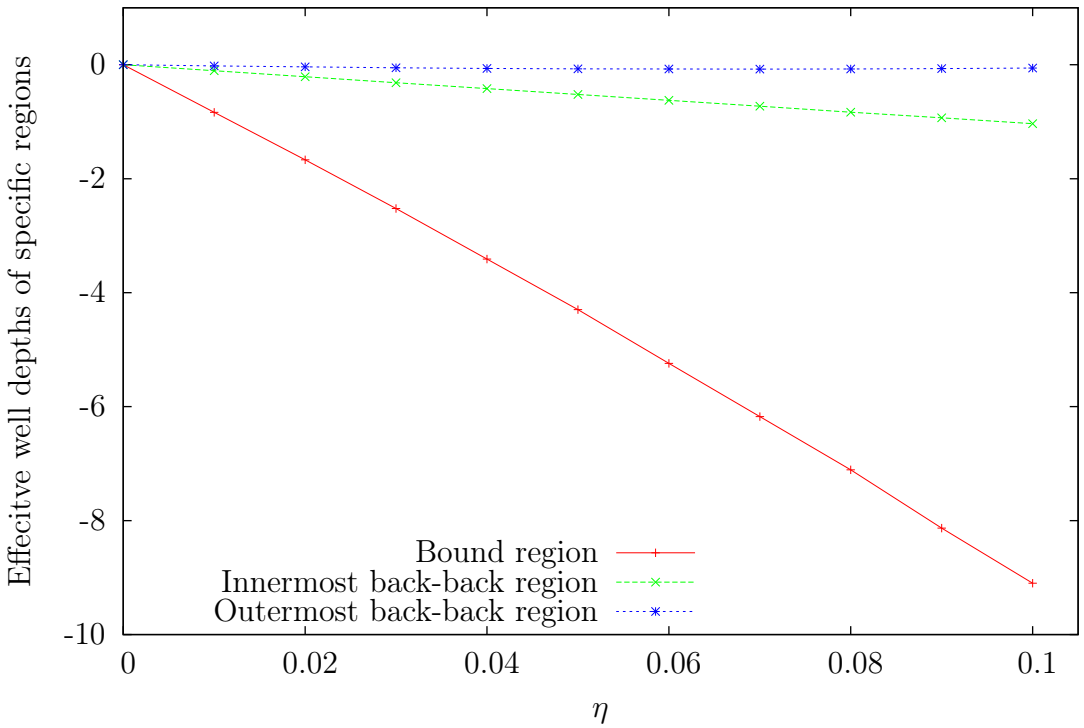

Figure 4.14: Well depth, or integrated potential well, for varying η. By effective well depths, we mean the integrated potentials across the equivalent regions in fig. 4.3. For example, the bound region at arbitrary η will have an integrated well depth expressed as $\Delta W^{\eta}_{\text{app}}\big|_{\text{A}}$, where A refers to the bound region in fig. 4.9.

Comparing effective well depths of specific regions between the mismatch (fig. 4.14) and exactly matching (fig. 4.6) cases, we observe that the mismatched case is nearly everywhere less attractive than the exact case. The essential shape, however, remains unchanged. These trends are reasonable as one expects the effective potential to be proportional to the number density of nanoparticles. The mismatch case should be less attractive as there is a smaller *difference* between the hard-sphere exclusion volume and bound exclusion volume, as seen in fig. 4.11. As pointed out before, what is unclear and thus the main driver behind this thesis is how exactly these potentials change with η and lock/key geometry.

4.8 Conclusion

For a lock and key colloidal system, we have shown how one can parametrise an effective potential. This was illustrated through the lens of a typical effective potential and how it can split into 'interesting regions' from which one applies the mathematical tools developed in chapter 3 to produce an effective potential. A visual comparison was made between this parametrised potential and the typical effective potential. Later, we demonstrate that the *lock-lock* effective potential is not only qualitatively similar, but quantitatively so by comparing it to an explicit GCA simulation [1].

Chapter 5

Results for Two Lock System

The next step in describing a general lock and key system is to consider the interactions between locks themselves. We want to parametrise the effective potential between two locks that fit together exactly. Using the coordinate system developed in section 3.6, we will see that we can extend the methodology used in previous sections and find that there is lot of common ground, even if the details require some work. In the simulations used to estimate ΔW, the box is cubic with a length of 3σ, where σ is the diameter of a key with radius, r_{L}, of 0.5. The locks have radii of $r_{\mathrm{L}} = r_{\mathrm{K}} = 0.5$ whilst the nanoparticle's radii, r_{n}, are a tenth of this. The lock's cutting sphere radius, r_{c}, and distance between cutting sphere and lock centre, d_{c}, is also 0.5. This system is identical to the exactly matched lock and key system, only with two locks instead of one.

5.1 Typical Effective Potential

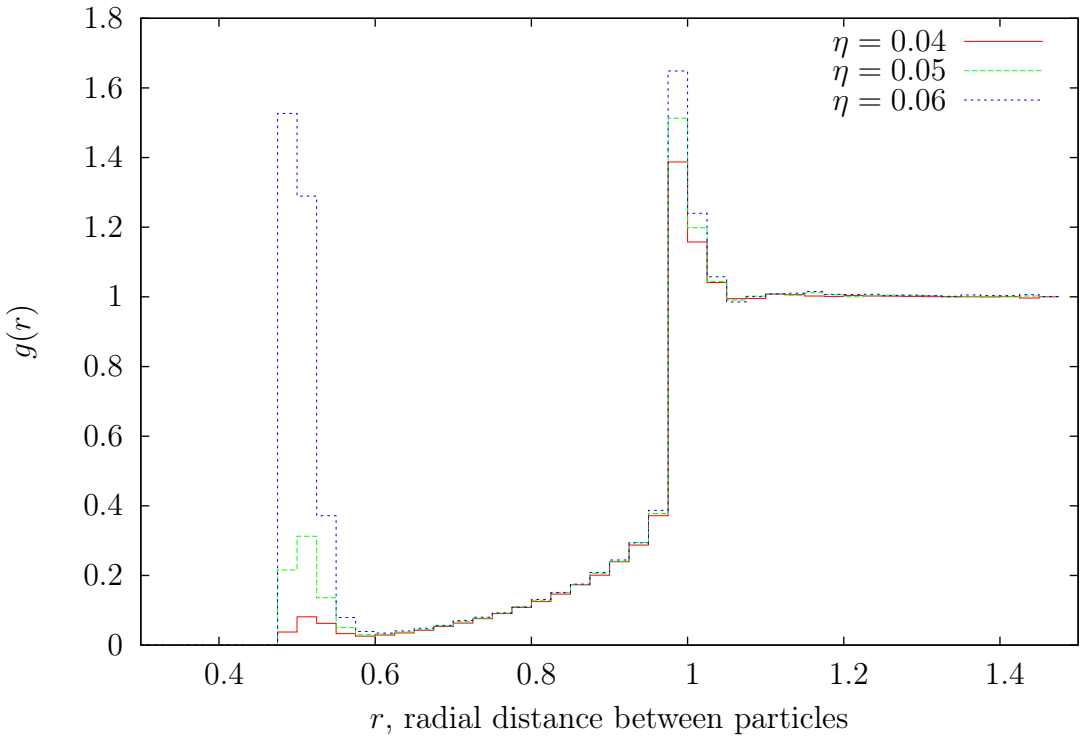

Figure 5.1: Radial distribution functions for different nanoparticle densities, η, of a two lock colloid. We note that the peak at $r = 0.5$ corresponds to the bound regime (where one lock is bound to the mouth of another) whilst the peak at $r = 1.0$ corresponds to the 'back-back' regime where one lock touches another, but not near the mouth.

One can see the immediate similarity between the lock and key system and our two lock system if we compare radial distribution functions. Figure 5.1 shows the familiar bound peak at $r = 0.5$ that corresponds to the closest possible approach of the lock to another lock and the analogous back-back peak where the lock is near the other, without being near the mouth at $r = 1.0$. We note therefore that the basic physical situation is not much more complicated than the lock and key system, though as we will see as this chapter unfolds, there are plenty of details to consider.

To make headway in parametrising the effective potential of a two-lock system, we expand the connection between the probability density of a lock and key system and the effective potential (eq. (3.14)) to the two-lock system as follows:

$$\Delta W^{\eta}(r, c_{\mathrm{r}}, c_{\mathrm{i}}, c_{\varphi}) = -\log\left(\frac{\mathbb{P}^{\eta}_{\mathrm{LL}}(r, c_{\mathrm{r}}, c_{\mathrm{i}}, c_{\varphi})}{\mathbb{P}^{\eta=0}_{\mathrm{LL}}(r, c_{\mathrm{r}}, c_{\mathrm{i}}, c_{\varphi})}\right). \tag{5.1}$$

It should be clear that eq. (5.1) is a function of four variables so is difficult to visualise. As a first attempt to characterise the effective potential, we will define an approximate effective potential:

$$\Delta W^{\eta}_{\mathrm{app}}(r, c_{\mathrm{r}}) = -\log\left(\frac{\int_{-1}^{1} \mathrm{d}c_{\mathrm{i}} \int_{-1}^{1} \mathrm{d}c_{\varphi} \mathbb{P}^{\eta}_{\mathrm{LL}}}{\int_{-1}^{1} \mathrm{d}c_{\mathrm{i}} \int_{-1}^{1} \mathrm{d}c_{\varphi} \mathbb{P}^{\eta=0}_{\mathrm{LL}}}\right) \tag{5.2}$$

We have already, informally, introduced this notation in chapter 4 for the lock and key

system. $\Delta W^{\eta}_{\mathrm{app}}(r, c_{\mathrm{r}})$ will be a good a approximation where the true $\Delta W^{\eta}(r, c_{\mathrm{r}})$ depends weakly on c_{i} and c_{φ}. This inference should follow from the discussion of "piecewise constant" approximate effective potentials in section 4.4.

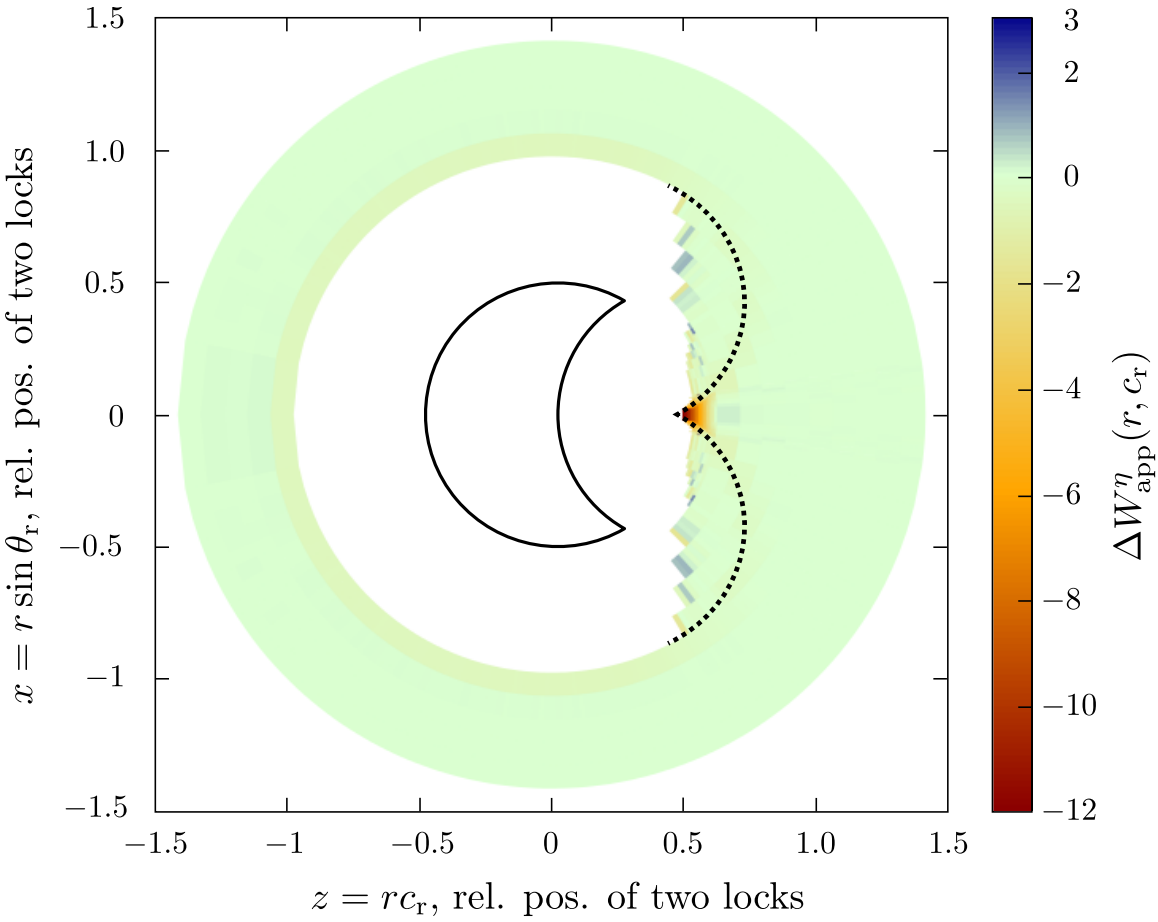

Figure 5.2: 2D effective potential from computer simulation for exactly fitting 2 lock system, where $r_{\mathrm{L}} = r_{\mathrm{c}} = d_{\mathrm{c}} = 0.5$ and $\eta = 0.07$. A new 'mouth-mouth' area has appeared between $z = 0.5$ and $z = 0.75$ that corresponds to when the lock directors are pointed at each other. The noisiness in this data is due to poor statistics, despite a very large data set. However, this has a minimal effect as the configurations of lock-lock associated with the noisy areas happen very rarely.

We are now in a position to introduce fig. 5.2, which demonstrates $\Delta W^{\eta}_{\mathrm{app}}(r, c_{\mathrm{r}})$. We recognise immediately that, due to the choice of coordinates in section 3.6, $\Delta W^{\eta}_{\mathrm{app}}(r, c_{\mathrm{r}})$ is very similar to the lock and key effective potentials.

5.2 Defining Regions of Interest

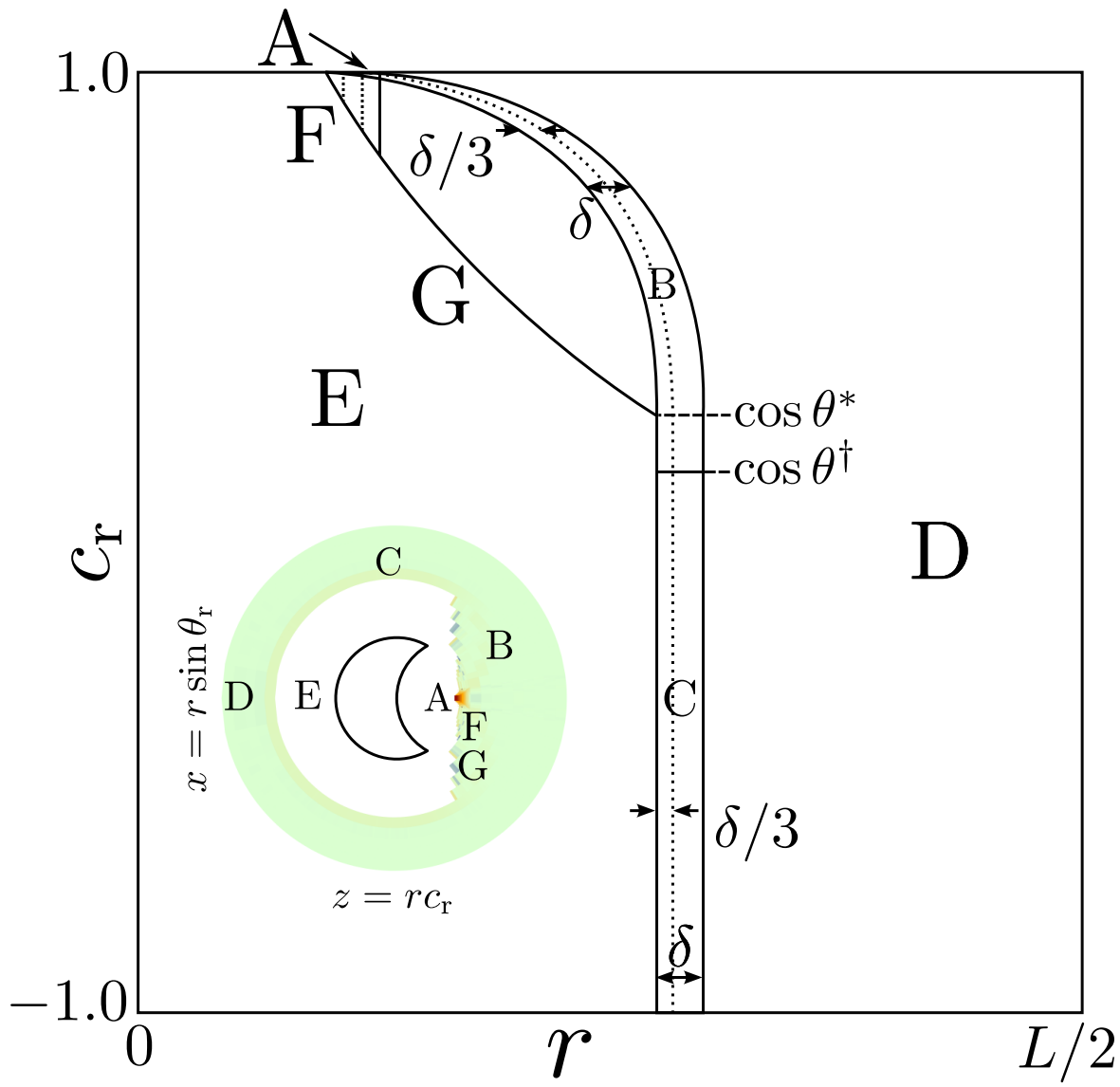

Figure 5.3: Diagram of how $\Delta W^{\eta}_{\text{app}}(r, c_r)$ is split into different regions. We call the regions as follows: A – bound, B – look-up, C – back-back, D – far-field, E – overlap, F – bound mouth-mouth, G – mouth-mouth. Regions B and C have a constant width of δ in r only, and are also split into subregions of constant width in r only of $\delta/3$ and $2\delta/3$.

Again, following the same principle as the lock and key case, we can use the lock and lock effective potential as guidance on how to proceed with parametrisation. We use functions in the (r, c_r) plane - which can be mapped back to the $(r, \cos\theta)$ case - along with sensible choices in the other lock-lock angular coordinates, c_i and c_φ, to partition the effective potential into similar regions of distinct behaviour. We use the same assumption that at sufficiently small nanoparticle packing fractions, any nanoparticle layering will not exceed one nanoparticle diameter. A sketch of this partitioning can be seen in fig. 5.3, where we have transformed the cylindrical polar coordinates of fig. 5.2 into (r, c_r)-space. We refer to eqs. (4.5) and (4.6) to define the edges of region B. The left edge of region G and F can then be defined as anything that is to the left of region B, where we remember the region E is forbidden by the hard-particle criterion. As such, we do not need to know the equation that describes the left edge of region F and G. The right edge of region F

is fixed by the same radial cut off as region A, which is typically $\delta r_{\rm n}$ in thickness, where $\delta = 2.0$. These partitionings are very similar to the lock and key case. We will motivate the existence of regions F and G in upcoming discussions. We note in particular that regions C, D and E are good approximations to the true $\Delta W^{\eta}(r, c_{\rm r})$. This is true because when the locks interact like spheres then $c_{\rm i}$ and c_{φ} - coordinates dependent on the orientations of the two locks - are clearly not important. With hindsight, we can therefore justify the name "relevant" for $c_{\rm r}$ because the dependence on $c_{\rm i}$ and c_{φ} is weak in most cases.

We note that fig. 5.2 has the strongest binding in region A of fig. 5.3 - when a lock is bound to the mouth of another like a key - which is as expected. The strong binding in region B is reminiscent of the lookup region for the lock and key, but we will describe these regions in more detail later on.

We now focus on regions that are unique to the two lock case. We call region F the mouth-mouth case and refer to the LHS of fig. 5.4 to demonstrate that it refers to when two lock mouths are facing each other. The RHS of fig. 5.4 is an example of the configuration seen in region G, where the mouth-mouth regime is skewed. We name this region the bound mouth-mouth region, as it is related to the mouth-mouth and bound configuration. We can ascribe configurations like the RHS of fig. 5.4 to why the white "overlap" region is smaller for the lock-lock than the lock-key system. Locks are able to approach each other more closely by assuming the bound mouth-mouth configuration.

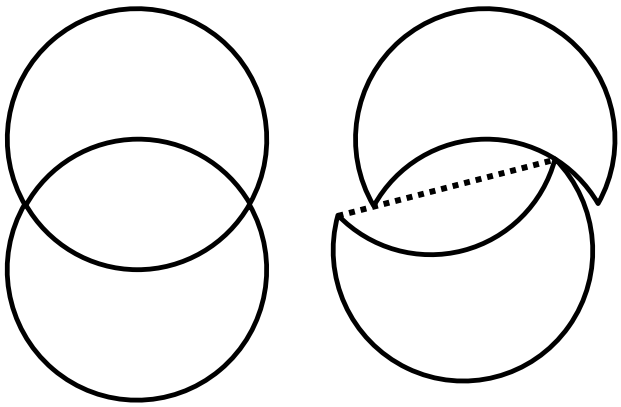

Figure 5.4: The left and right figure indicates the mouth-mouth and bound mouth-mouth two-lock configurations respectively. These are two-dimensional representations of a three-dimensional system, so we sketch a line across the mouth of the left hand lock to demonstrate that a 3D lock cannot approach closer than this. This may be seen by considering explicitly the 3D geometry of the lock particle.

5.2.1 Two Bound Regions

There are some regions where one must talk about the dependence of the approximate effective potential on $c_{\rm i}$ and c_{φ}. As a first step, we discuss the bound region. Figure 5.5 shows the two-dimensional dependence, in region A only, of the effective potential on $(c_{\rm i}, c_{\varphi})$-space. We have laid a 'tile' on top of region A, and integrated over all degrees of freedom within this region *except* for $c_{\rm i}$ and c_{φ}.

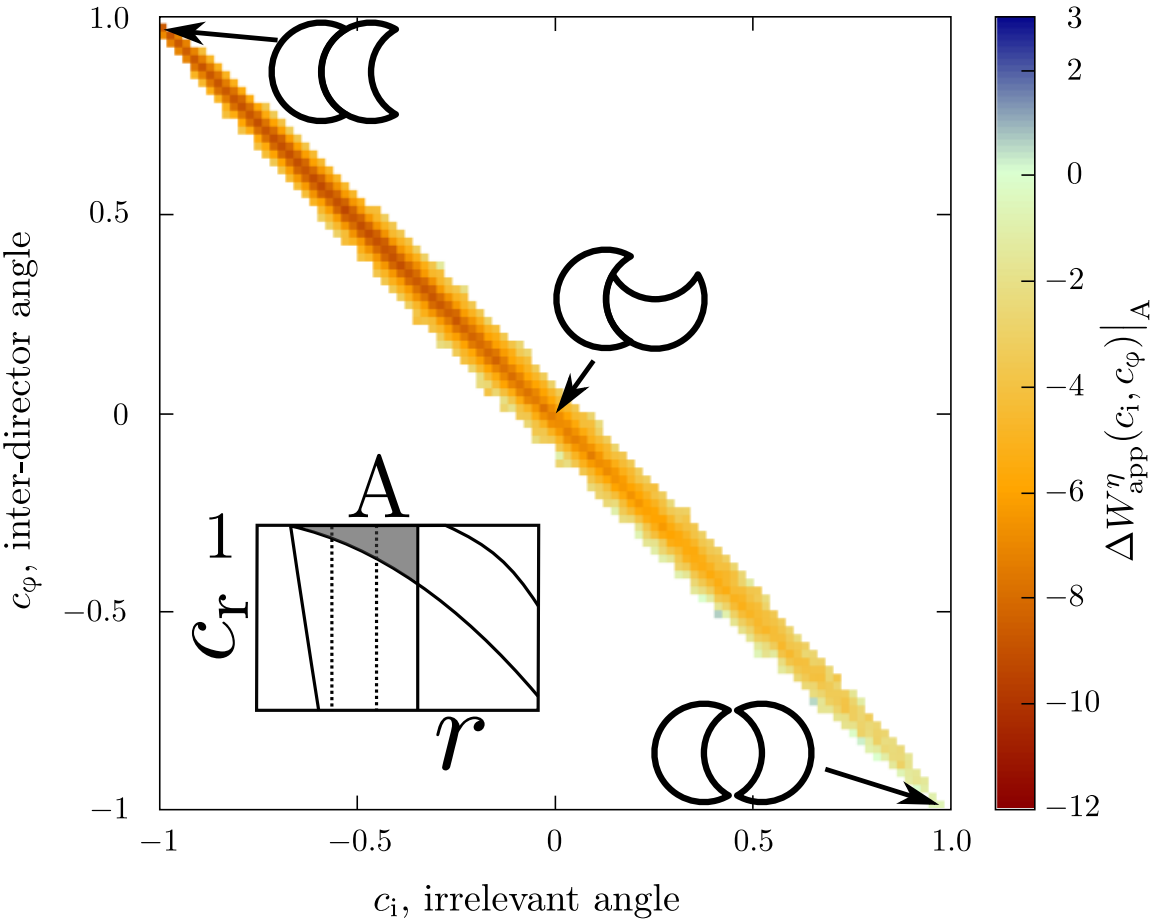

Figure 5.5: A 2D effective potential from computer simulation for an exactly fitting 2 lock system, $\Delta W^\eta_\mathrm{app}(c_\mathrm{i}, c_\varphi)\big|_\mathrm{A}$, bound region, $\eta = 0.07$. The bottom left inset image is a reminder that this potential is restricted to the bound (r, c_r) region A. We see the highest attraction along the diagonal, with the point (-1,1) corresponding to two bound locks (inset image). As the right lock rotates in the bound position, we see a decrease in potential, e.g., (0,0), until we finally reach a very small potential at the 'mouth-mouth' configuration, (1,-1).

More strictly speaking, in the same manner as $\Delta W^\eta_\mathrm{app}(r, c_\mathrm{r})$, we write that the true effective potential that depends on c_i and c_φ is

$$\Delta W^\eta(c_\mathrm{i}, c_\varphi | r, c_\mathrm{r}) = -\log\left(\frac{\mathbb{P}^\eta_\mathrm{LL}(c_\mathrm{i}, c_\varphi)}{\mathbb{P}^{\eta=0}_\mathrm{LL}(c_\mathrm{i}, c_\varphi)}\right) \tag{5.3}$$

and the equivalent approximate effective potential is

$$\Delta W^\eta_\mathrm{app}(c_\mathrm{i}, c_\varphi | r, c_\mathrm{r}) = -\log\left(\frac{\int_{\nu(r,c)} \mathrm{d}r\mathrm{d}c_\mathrm{r}\mathbb{P}^\eta_\mathrm{LL}}{\int_{\nu(r,c)} \mathrm{d}r\mathrm{d}c_\mathrm{r}\mathbb{P}^{\eta=0}_\mathrm{LL}}\right). \tag{5.4}$$

Note that the vertical bar on the LHS of both equations denotes that the specific c_i and c_φ depend on r and c_r. The special integral limit, $\nu(r, c_\mathrm{r})$, denotes that the specific integral area in c_i, c_φ space depends on the specific slice in r, c_r space. As a helpful guide, the *shape* of fig. 5.5 changes depending on which inset region we are integrating over. Therefore, for region A, the limits of our integrals will be set to $r_\mathrm{L} \leq r \leq r_\mathrm{L} + \delta r_\mathrm{n}$ and $c^+_\mathrm{r} \leq c_\mathrm{r} \leq 1.0$, where c^+_r is the point at which the RHS of region F intersects with the LHS of region B. As a further short hand, when referring to a specific region the RHS and LHS of eq. (5.4)

will become (e.g., region A):

$$\Delta W^{\eta}_{\mathrm{app}}(c_{\mathrm{i}}, c_{\varphi})\big|_{\mathrm{A}} = -\log\left(\frac{\int_A \mathrm{d}r\mathrm{d}c_{\mathrm{r}}\mathbb{P}^{\eta}_{\mathrm{LL}}}{\int_A \mathrm{d}r\mathrm{d}c_{\mathrm{r}}\mathbb{P}^{\eta=0}_{\mathrm{LL}}}\right). \tag{5.5}$$

For the approximate effective potential in region B, we will include a limit to demonstrate that we are in a particular region, i.e., $\Delta W^{\eta}_{\mathrm{app}}(c_{\mathrm{i}}, c_{\varphi})\big|_{\mathrm{A}}$. Figure 5.5 is a reasonable approximation to the true $\Delta W^{\eta}(c_{\mathrm{i}}, c_{\varphi})$ within the ranges of r and c_{r} defined. We are able to map any point in the ranges defined to the same two-dimensional effective potential, $\Delta W^{\eta}_{\mathrm{app}}(c_{\mathrm{i}}, c_{\varphi})\big|_{\mathrm{A}}$. The large white areas in fig. 5.5 have two origins. The first is what we are more familiar with, namely that the particles are forbidden to overlap in certain positions. The second is due to the coordinate system itself. We can see this by remembering that the irrelevant angle, c_{i}, is subject to the size of the relevant angle, c_{r}, as mentioned in section 3.6, and further, that c_{φ} is then dependent on c_{r} and c_{i}. As a simple first-order argument, the further 'up' in fig. 5.3 we are, the more constrained the $(c_{\mathrm{i}}, c_{\varphi})$-space effective potential arguments will be. Once r and c_{r} have been fixed, there are purely geometrical constraints on the possible values of c_{i} and c_{φ}. Thankfully, these constraints are independent of nanoparticle density so when we take the ratio of probability densities to produce the effective potential, they cancel out.

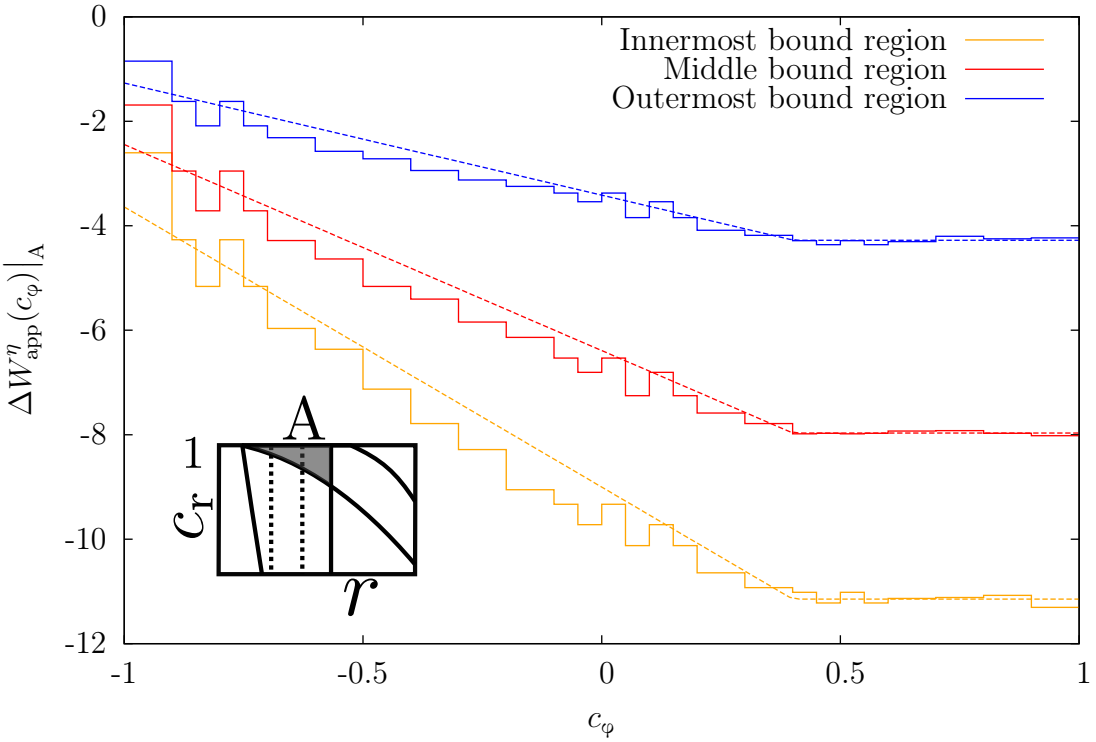

Figure 5.6: 1D effective potential from computer simulation for exactly fitting 2 lock system in the bound region, $\Delta W^{\eta}_{\mathrm{app}}(c_{\varphi})\big|_{\mathrm{A}}$. From bottom to top, we have the left-most to right most third of the bound region, as shown in the inset image.

Given the narrowness of the coloured region in fig. 5.5, we can approximate the functional dependence of $\Delta W^{\eta}_{\mathrm{app}}(c_{\mathrm{i}}, c_{\varphi})\big|_{\mathrm{A}}$ on c_{i} and c_{φ} by a simple function of c_{φ} alone. We show this in fig. 5.6, where we have further divided region A into three regions for more granularity. As expected, the binding is strongest at large c_{φ} and weakest at small c_{φ}. The

images in fig. 5.5, going from bottom to top map to the bottom axis of fig. 5.6, going from left to right. We will explain the fits to fig. 5.6 later.

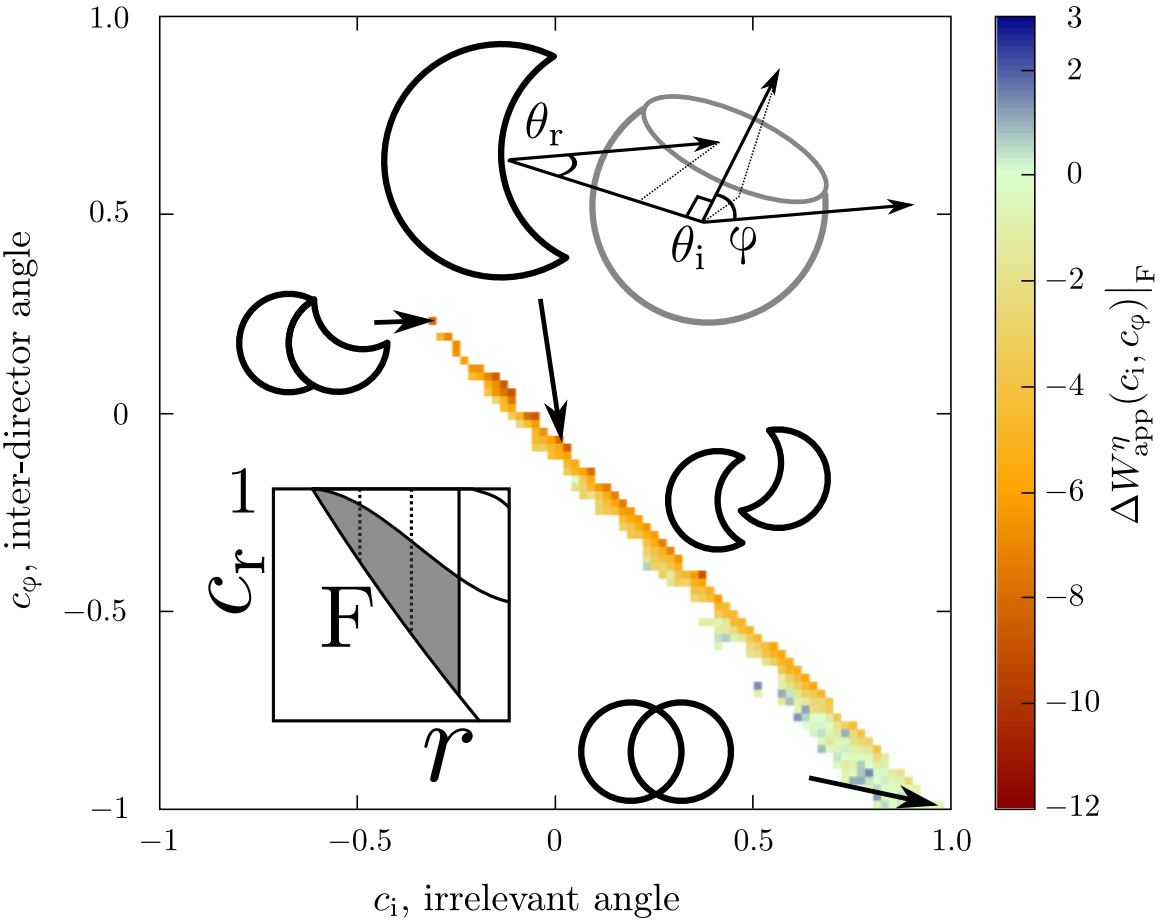

Figure 5.7: 2D effective potential from computer simulation for exactly fitting 2 lock system, $\Delta W^\eta_\mathrm{app}(c_\mathrm{i}, c_\varphi)\big|_\mathrm{F}$, bound mouth mouth region, $\eta = 0.07$. The bottom left inset image is a reminder that this potential is restricted to the bound mouth mouth (r, c_r) region F. As with fig. 5.5, we see the highest attraction along the diagonal. Due to the restriction in (r, c_r) space, we do not see any potential until approximately (-0.3, 0.2) where an inset image demonstrates the corresponding lock configuration. As we move down the diagonal, we see that the right lock prefers to be facing the lip of the left lock. At (0, -0.05), we have sketched a truer 3D representation of the lock configuration. The other inset images are approximate.

Figure 5.7 demonstrates $\Delta W^\eta_\mathrm{app}(c_\mathrm{i}, c_\varphi)\big|_\mathrm{F}$, i.e., the approximate two-dimensional effective potential confined to the (r, c_r)-space of region F. We have shown in the inset images approximate configurations of two locks. We call region F the bound mouth-mouth region, recognising that it can be very similar to the bound region and the mouth-mouth region. Given the narrowness of this region, we choose to discretise region F into three equal regions in r, essentially giving each sub-region its own, constant, value of effective potential, i.e.,

$$\Delta W^\eta_\mathrm{app}\big|_{\mathrm{Fn}} = -\log\left(\frac{\iint\limits_{Fn}\mathrm{d}r\mathrm{d}c_\mathrm{r}\iint\limits_{-1}^{1}\mathrm{d}c_\mathrm{i}c_\varphi\mathbb{P}^\eta_\mathrm{LL}}{\iint\limits_{Fn}\mathrm{d}r\mathrm{d}c_\mathrm{r}\iint\limits_{-1}^{1}\mathrm{d}c_\mathrm{i}c_\varphi\mathbb{P}^{\eta=0}_\mathrm{LL}}\right), \tag{5.6}$$

where n represents the particular sub-region. We justify the choice of being independent

of c_i and c_φ by realising that the lock and key will infrequently assume the bound mouth-mouth configuration, as the much more favourable bound configuration is very close in (r, c_r)-space. This infrequency can be observed in the noisy data (despite more than a billion data points).

It should be clear from fig. 5.2 and fig. 5.3 that region G experiences neither attraction or repulsion. The noisy edges are caused by the same constraints of geometry as the bound mouth-mouth case.

To the RHS of regions G and E, we can collapse back on to the exact lock and key case as inter-lock orientations do not matter and so can safely borrow the relevant equations from section 4.6.2. The locks can be treated as spheres in these regimes.

5.3 Parametrisation of Effective Potential

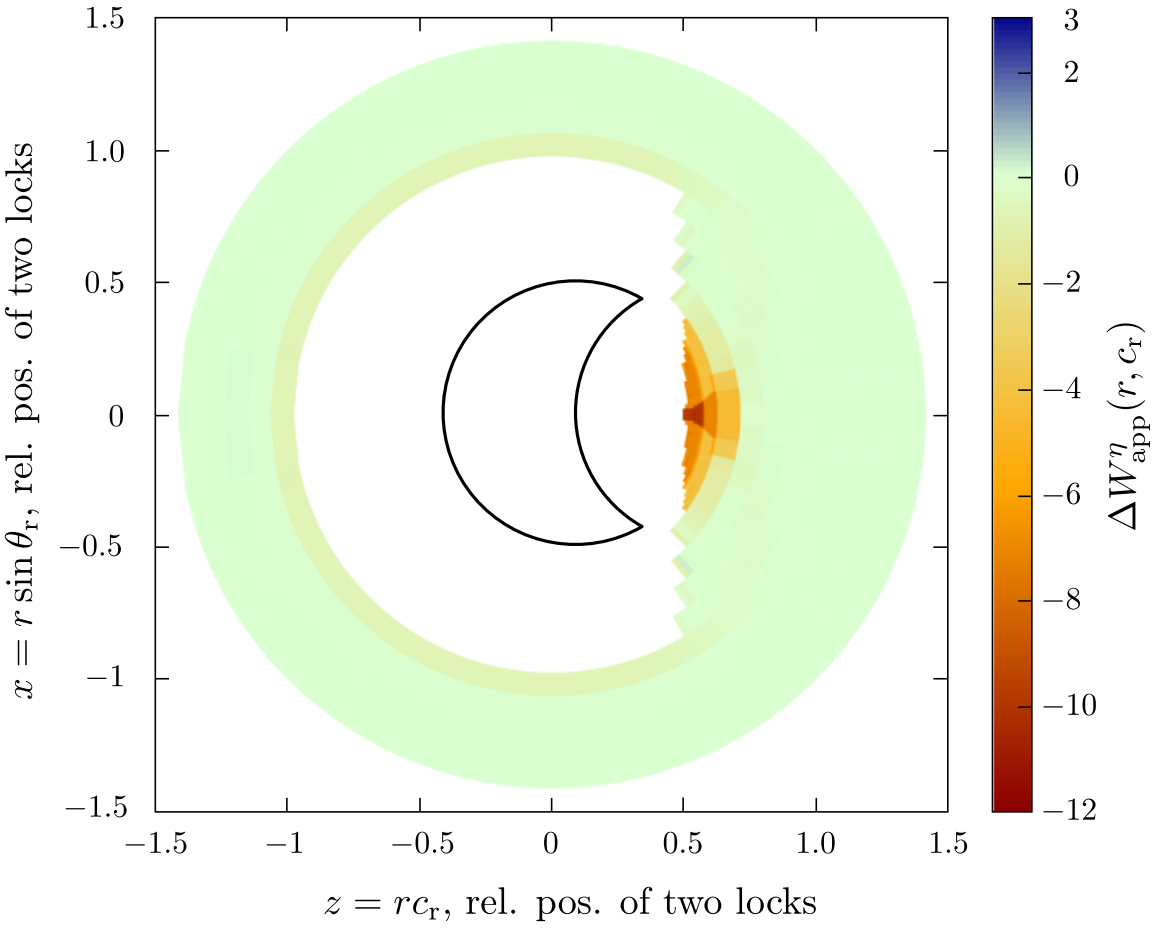

Figure 5.8: Typical parametrised $\Delta W^\eta_\mathrm{app}(r, c_\mathrm{r})$ for a lock-lock system. The parametrised effective potential is generated with data from a real computer simulation, with the same properties as fig. 5.2, i.e., $r_\mathrm{L} = r_\mathrm{c} = d_\mathrm{c} = 0.5$ and $\eta = 0.07$.

To parametrise the lock and lock effective potential for any given state point, we separated computer simulation data into different regions as discussed in the previous section. Depending on the region in fig. 4.3, rationalisations were made as to how many degrees of freedom were reasonable to explicitly include. Other degrees of freedom were essentially 'integrated out'. We present fig. 5.8 as an example of a typical parametrised potential that was generated from parametrising the data that produced fig. 5.2. In more detail,

this procedure involved running a GCA simulation with exactly the same parameters as fig. 5.2 but with no nanoparticles and associating a parametrised effective potential with each lock. This procedure is much like the lock and key system. The obvious difference between this parametrised effective potential and fig. 5.2 is region F. The real attractive potential is more localised to large c_r whilst our approximate effective potential is more smeared out. We show a magnified version of fig. 5.2 in fig. 5.9 to demonstrate the spread out nature of the effective potential. The real effective potential is much more attractive towards the left-most sub-region of region F, as can be seen in the inset image of fig. 5.9. Since we match the integral of the potential, it is our hope that this will make only a small difference to the reproduction of any self-assembling behaviour with our parametrisation method. Here, therefore, we see a trade off between algorithmic simplicity and the real potential landscape. In a later section, we present evidence that this 'smeared out' approximation is sufficient to reproduce some self-assembly behaviour.

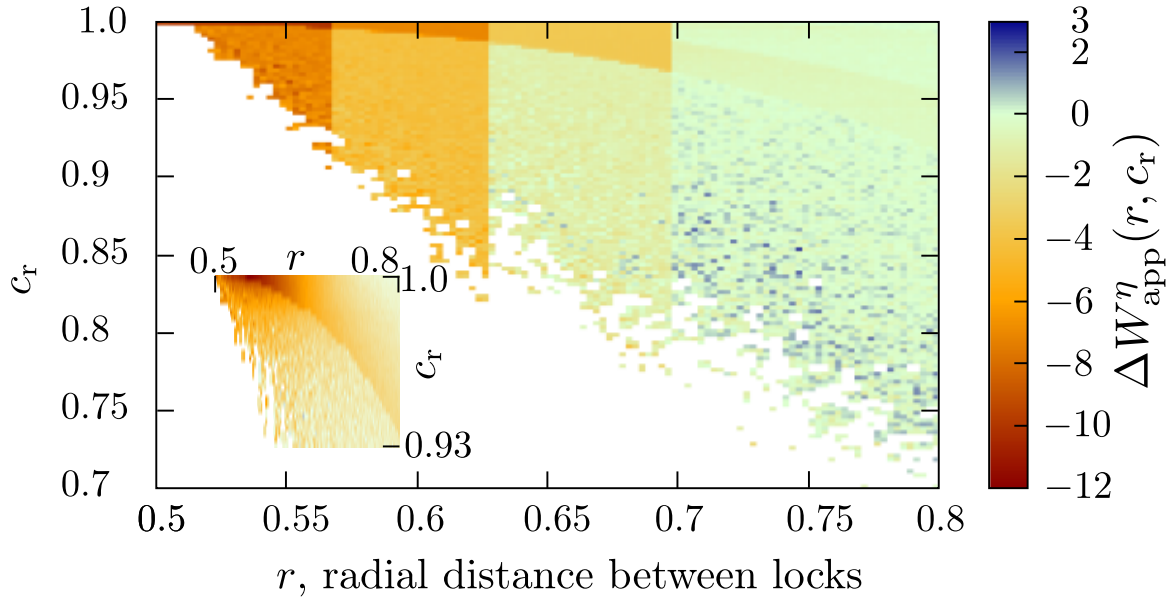

Figure 5.9: An enlarged version of the parametrised effective potential in the (r, c_r) plane, restricted to $0.5 \leq r \leq 0.8$ and $0.7 \leq c_r \leq 1.0$. Here we use finer, constant in r and c_r, binning than fig. 5.8 to demonstrate the subdivision of the bound and bound mouth-mouth regions in fig. 5.3. We can also observe the look-up region at $r > 0.7$, near the top right of the figure. The inset image demonstrates the equivalent, zoomed in, real effective potential. We see the attraction is much more concentrated to lower r and higher c_r than in the three sub-regions of the parametrised version.

5.3.1 The two bound regions

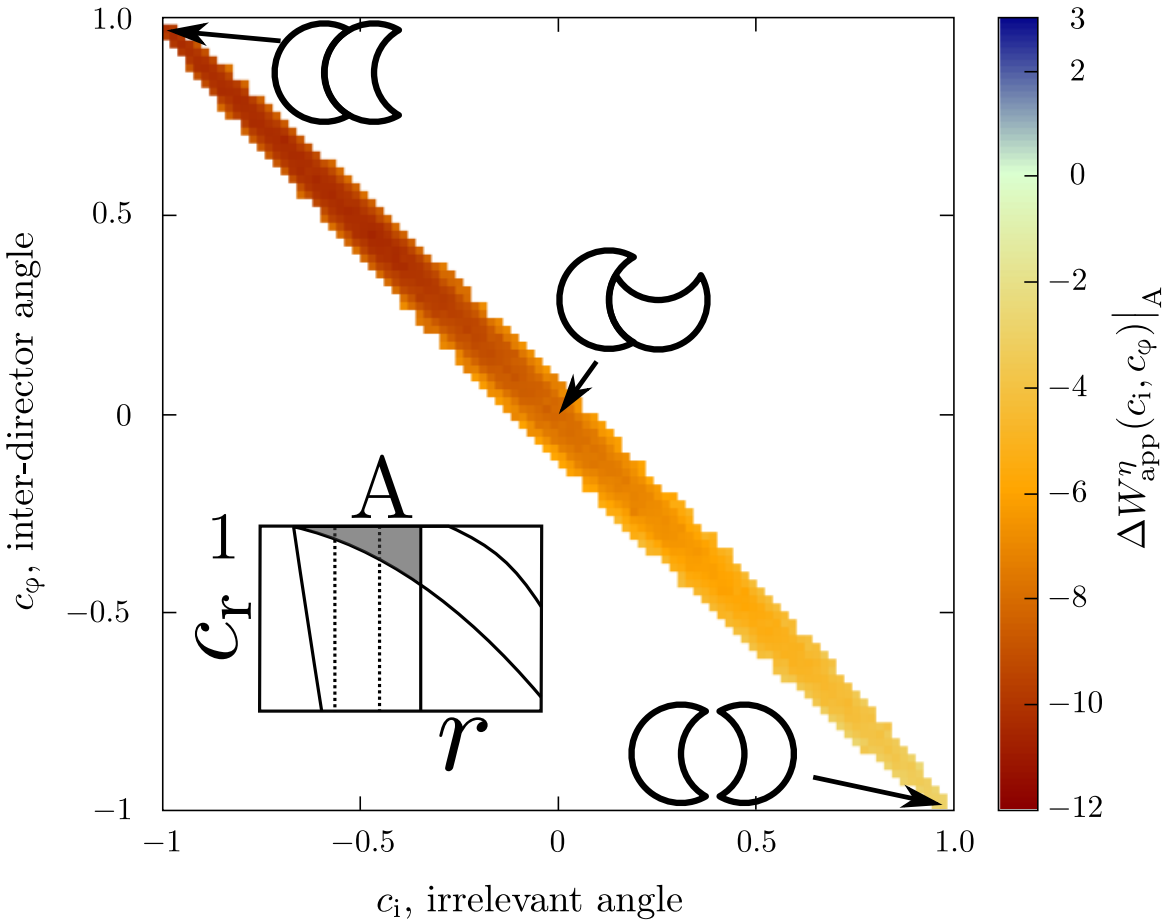

Figure 5.10: A 2D parametrised potential, generated from the parametrisation of an equivalent system. Compare with fig. 5.5. We are therefore affirmed in our choice of having the depletion potential in this region depend on c_φ only (fig. 5.6.) Note that here, we are in the bound regime, region A.

Figure 5.10 demonstrates a typical parametrised effective potential in the $(c_\mathrm{i}, c_\varphi)$ plane, confined to region A. There is excellent parity with fig. 5.5. Importantly, we do not attempt to encode fig. 5.10 into our effective potential algorithm because we can represent $\Delta W(c_\mathrm{i}, c_\varphi)$ with a 1D potential in c_φ, $\Delta W(c_\varphi)$, as in fig. 5.6. We can perform a simple constrained fit (Appendix C) - in which we ensure that the integrated potential over the whole c_φ range in question, $\Delta W^\eta_\mathrm{app}\big|_\mathrm{A}$, is satisfied - on the data points in fig. 5.6 to produce the lines of best fit. The parameters associated with this constrained fit are then are used in the effective potential algorithm. We point out here that we have chosen to break the usual "piecewise constant" effective potential strategy as the c_φ-dependence is obviously not piecewise constant. We perform this constrained fit to ensure that the second virial, B_2, is preserved. For hard spheres, Noro and Frenkel [72] discuss that matching B_2, based off a corresponding pair potential, can, through a law of corresponding states be used a rough guide to the phase behaviour. For a many lock and key system, we observe that this works empirically. [1]

[1] We reason that this is because our system is also short range, and therefore to a rough approximation, the only thing that matters is how our locks and keys are touching. For spheres, according to Noro and

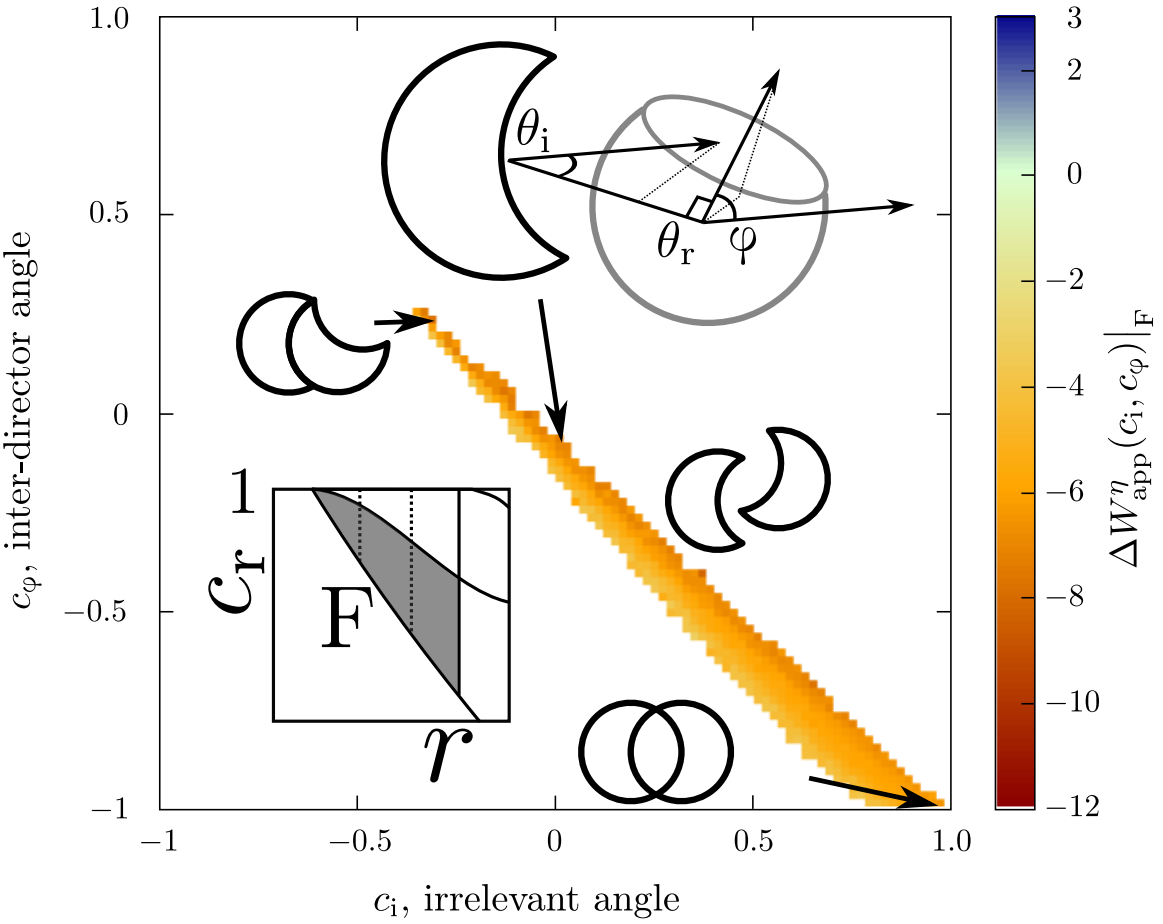

Figure 5.11: A 2D parametrised potential, generated from the parametrisation of an equivalent system. Compare with fig. 5.7. Note that here, we are in the bound mouth-mouth regime.

We note a similar effective potential in the bound mouth-mouth region in fig. 5.11 to fig. 5.7. We note that fig. 5.7 has relatively poor statistics and posit that it should look actually look more like its parametrised cousin. Importantly, we retain the mouth on mouth-*edge* preference in the parametrised case.

5.4 Comparing Lock-Lock to Lock-Key

We restate here that exact and mismatch lock and key refer to the geometry of the lock and key. An exactly fitting lock and key means that the key will fit into the mouth of the lock with no room for manoeuvre, whilst an mismatch lock and key means that there are multiple places where the key can be said to be bound to the lock.

In this chapter, we have analysed effective interactions between lock particles, which we now compare with the results for the lock-key interactions from chapter 4. We have already seen that the exact and mismatched cases have essentially the same, distinct, regions of parametrisation and that the lock-lock introduces two new regions associated with the mouth facing mouth lock orientations. From fig. 5.12, we observe that between $\eta = 0$ and $\eta = 0.10$ there is little difference between the exact and lock-lock binding free

Frenkel, there should be one number - B_2 - that describes their behaviour due to the range and strength of their interactions. We make an empirical observation that B_2 seems to be sufficient as well.

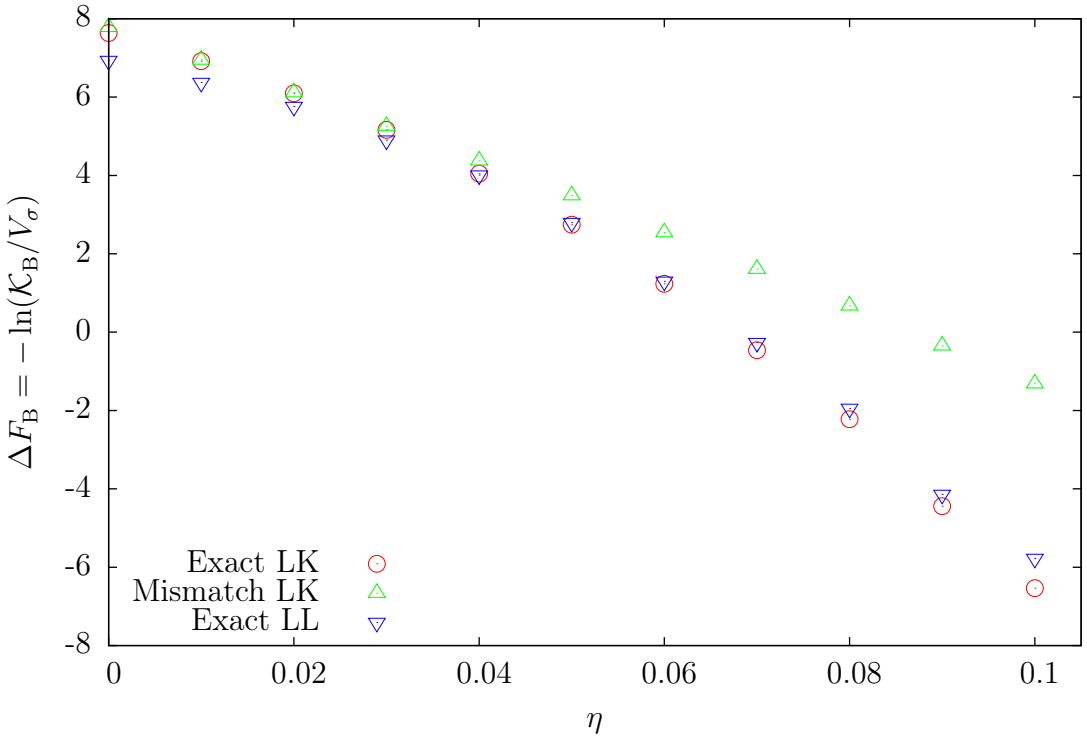

Figure 5.12: A comparison of the binding free energies, ΔF_{B}, for the exact lock-key (LK), mismatched LK and exact LL. The most distinguishing feature is the divergence of the mismatch LK ΔF_{B} away from the other cases.

energy. The data indicates that the exact lock and key (LK) is less 'sticky' at lower packing fraction than exact lock lock (LL), but by $\eta = 0.07$, exact LK has overtaken exact LL. The mismatched LK diverges from the exact cases by $\eta = 0.04$, reflecting an overall lower binding propensity.

We can understand the binding free energy by observing the back-back free energy, ΔF_{BB}, which is less attractive for the exact LL fig. 5.13. Within error, the LK cases are the same. Therefore, we can say that this particular LK system is more prone to back-back self-assembly than the LL system. We can make qualitative arguments that a two lock system has less overall 'back-back' region. In this light, a key is essentially entirely 'back-back'. The exact LK system has a similar propensity to bind as the LL, reflecting their overall similarity. The exact LK overtaking the LL may be attributed to the additional LL mouth-mouth region. This mouth-mouth region is physically very close to the bound region. As such, it may be possible that the mouth-mouth to bound transition is more sensitive to η - i.e., additional nanoparticles somehow block the transition - therefore leading to the exact LK overtaking the LL. A mismatched LK system has a greater mouth surface area. This means that there are more ways in which a key can be called bound. This is in competition with a greater nanoparticle layering. We see the increased number of nanoparticles really taking effect at about $\eta = 0.04$ onwards, where the mismatched LK system rapidly diverges away from the exact cases.

We can explain the vertical shift in fig. 5.13 with a geometrical argument, in which we note that there are fewer ways for a lock to be bound to the mouth of another lock compared to a key in the same situation. This is because the bound lock must have a

particular orientation. Any deviation from from this orientation will mean that the lock will end up in a mouth-mouth or bound mouth-mouth regime, which would not be counted.

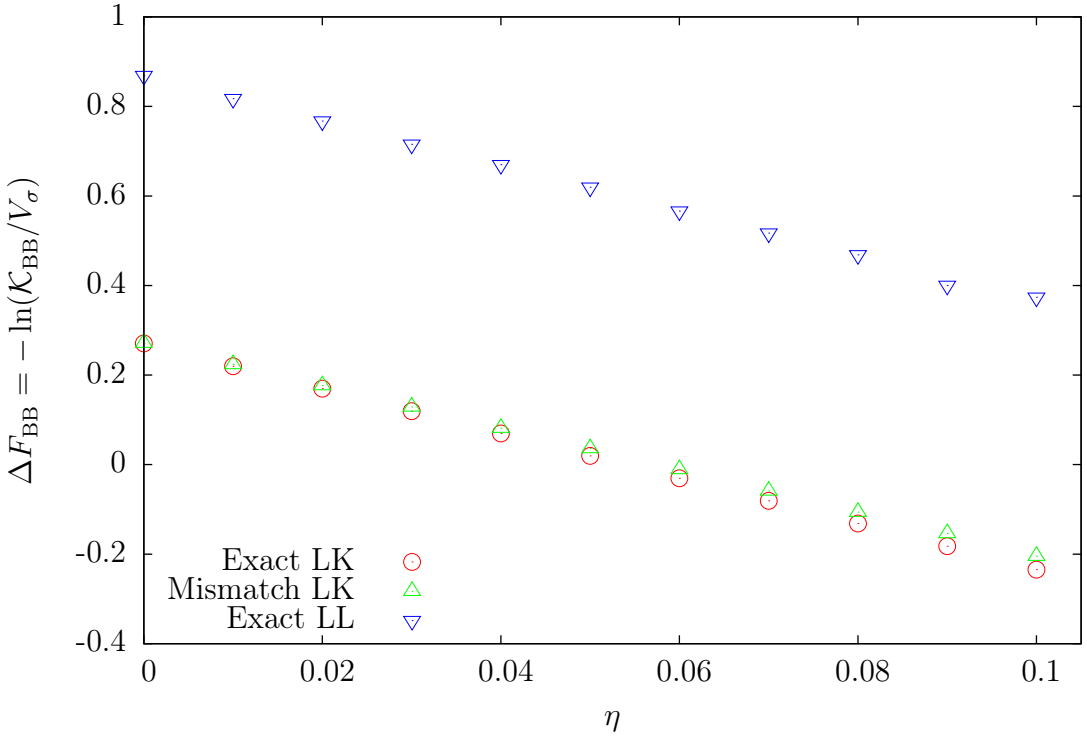

Figure 5.13: A comparison of the back-back binding free energies, ΔF_{BB}, for the exact lock-key (LK), mismatched LK and exact LL. The most distinguishing feature is the everywhere positive ΔF_{BB} of the LL case, compared to the partially attractive LK cases.1

5.5 Verifying the Parametrisation

Here, we attempt to reproduce some of the results of Ashton et al. [1] using parametrised effective potentials - as developed in previous chapters - together with a pre-existing simulation that employs the geometrical cluster algorithm on a mono-disperse lock-only system. A successful reproduction of these results would then provide evidence that the effective potential parametrisation is valid and thereby trustworthy in future works.

For a system of locks, Ashton et al. [1] defines X as the fraction of locks with a free binding site. Figure 5.14 superimposes X generated from employing the GCA with an effective potential with data from their paper for $h = d_{\mathrm{c}} = 0.5$. We can see a good agreement for the state points chosen. At lower X (higher η), we see a small deviation between the explicit lock simulation. This probably originates from equilibration issues. By equilibration issues, we mean that even in a GCA simulation, some configurations will be sampled less. Examples of these pathological cases are the relaxation of chains. For the GCA, there is no explicitly written move set that ensures that a chain will break into sub-chains (the plane pivot moveset can relax the orientations of a chain, but this is distinct from breaking apart a chain whilst retaining some structure). Therefore, the GCA can lead to systems that become stuck in states of non-typical chain lengths. Keeping such a problem in mind, a higher packing fraction will cause greater equilibration issues as chains,

once bound together, will be even less likely to break apart into separate chains.

With our parametrisation approach, we are able to run our simulation for a greater number of total Monte Carlo moves so that our lock and key system has time to 'un-stick'. It is also plausible that our approach leads to easier equilibration for the full system because our bonds are more flexible due to the three subregions of our bound region (fig. 4.7). The real effective potential (fig. 4.2) is less equally distributed in terms of its bound region.

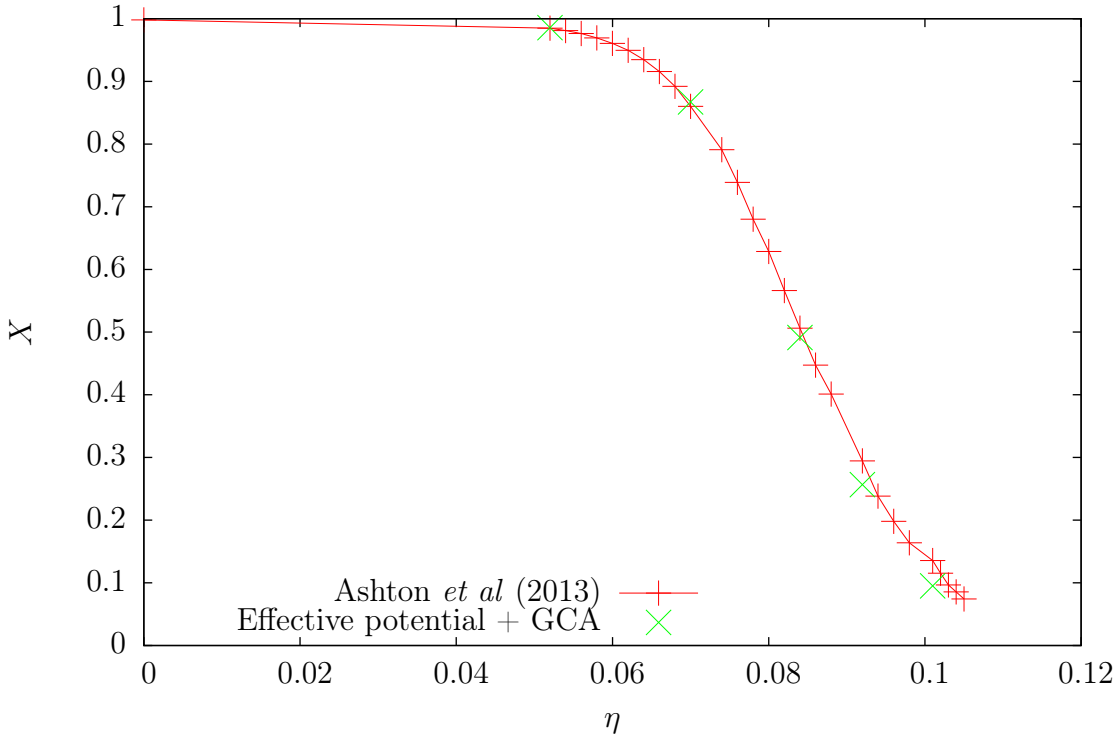

Figure 5.14: Comparing lock occupation between Ashton et al. [1] and data generated from effective potentials of certain state points used in a lock-only GCA simulation.

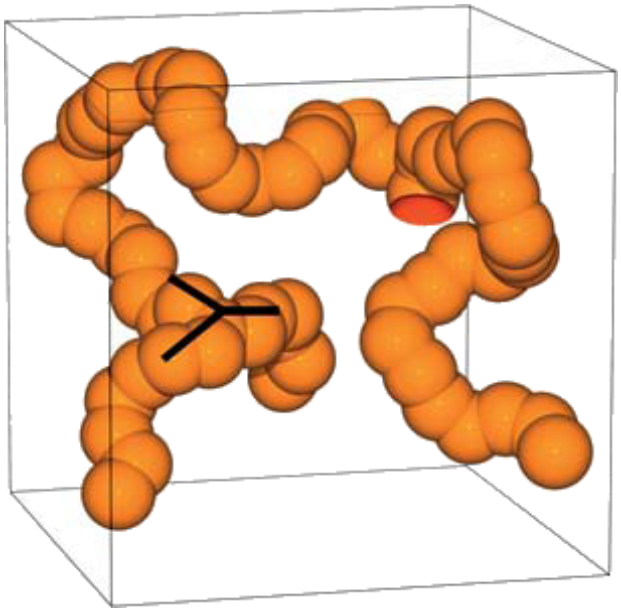

Figure 5.15: Based on Ashton et al. [1]. A highlighted example of branching in a lock and key system at $h = 0.5$, where $h = r_{\mathrm{L}}$ in this instance.

Using the same analytic software as Ashton et al. [1], a branching factor of $(3 \pm 1)\%$

was found for $X < 0.1$ and $h = 0.5$. This falls within the error bars of the published data of 1%[2]. A branch point refers to the nexus of two or more locks that have bound on to the 'back' of another. We demonstrate this in fig. 5.15. A branching factor is therefore the ratio of the number of these branching points to the total number of particles present.

With respect to time taken to produce data, each effective potential data point in fig. 5.13 took on the order of an hour to produce, whilst the data from Ashton et al.[1] took on the order of days to produce. Unfortunately, we balance this order of magnitude speed up with the time taken to *produce* data of sufficient quality to parametrise. Typical time needed to produce quality parametrisable data is on the order of days, though this can be expedited by running many simulations at the same state point in parallel.

5.6 Conclusion

In the same fashion as a single lock, single key system, we have shown how one can parametrise an arbitrary two lock effective potential. This was illustrated through the lens of a typical effective potential and how it can split into 'interesting regions' from which one applies the mathematical tools developed in chapter 3 to produce an effective potential. A visual comparison was made between this parametrised potential and the typical effective potential. We demonstrate that the *lock-lock* effective potential is not only qualitatively similar, but quantitatively so by comparing it to an explicit GCA simulation [1].

[2]Private communication with Douglas Ashton

Chapter 6

Sedimentation Behaviour of a Many Lock System

Recently, in 2013, Ivell et al. [57] studied the sedimentation behaviour of a suspension of locks near a wall. They showed how the boundary conditions of the wall cause a counter-intuitive development of disorder over time. Here, we present an analogous Monte Carlo simulation, where hard locks are simulated near a soft potential barrier in order to explore the interesting effects of the boundary conditions on lock sedimentation. Specifically, we study the sedimentation behaviour of increasingly shallow locks and compare this to the simpler sphere case.

We begin by summarising the findings of Ivell et al. before discussing how we ensure that our simulation matches experiment as closely as possible. We then discuss the mathematical tools needed to extract meaningful information from our simulation before ending with an account of the findings of our experiment.

6.1 Experimental Sedimentation

Ivell et al. created a suspension of monodisperse locks using 3-methacryloxypropyl trimethoxysilane from some existing methods in the literature, due to Sacanna et al. [73]. They filled a small glass vial that had been truncated and glued on to a glass coverslip with a suspension of locks ($\eta \approx 0.01$). Before any measurements with confocal microscopy, the solution was allowed to 'sediment completely'. Ivell et al. discovered a decrease in crystallinity in the lowest layer of locks within the first 48 hours of sample preparation. All observations were taken from 'bottom-up'. They note this decrystallisation correlated with a transition from mouth-down to in-plane locks *without* an increase in lock density. They hypothesise that this lock reorientation from a more ordered state of hexagonal close packing is due to upper layer pressure, causing the bottom-most locks to form a disordered state.

6.2 Matching Physical Characteristics

We imitated the experiment of Ivell et al. by using a standard small move, small rotation Monte Carlo simulation of many hard locks in a box, under the influence of a gravitational bias in the z-axis. The standard periodic boundaries were used in the x, y plane but a soft, repulsive, potential was introduced in the farthest edges of the box in the z axis to simulate the glass coverslip in the original experiment.

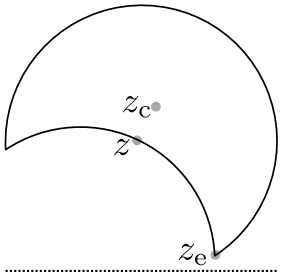

Figure 6.1: Diagram of different vertical, z-like coordinates used in the simulation of the sedimentation of a many lock system. z_e is the point of closest approach, z_c is the centre of mass - adjusted from that of a sphere due to the lock mouth - and z is the geometric centre of a sphere with the same radial size, r_L, as a lock..

6.2.1 9-3 Lennard-Jones Potential

We modelled the 'floor' of the glass coverslip of height h with a truncated 9-3 Lennard-Jones potential, due to Abraham and Singh [74][1] and shown in fig. 6.2, of the form

$$V_F(z_e) = \begin{cases} \epsilon\left[\frac{\sigma^9}{z_e^9} - \frac{\sigma^3}{z_e^3}\right] + c, & \text{if } z_e > 3^{1/6}\sigma \\ 0, & \text{otherwise} \end{cases} \tag{6.1}$$

and the 'ceiling', or upper surface of the lock suspension with a similar repulsive potential of the form

$$V_C(z_e) = \begin{cases} \epsilon\left[\frac{\sigma^9}{(h-z_e)^9} - \frac{\sigma^3}{(h-z_e)^3}\right] + c, & \text{if } z_e < h - 3^{1/6}\sigma \\ 0, & \text{otherwise} \end{cases} \tag{6.2}$$

As we are dealing with a lock shaped particle, we let the potential interact with the point of closest approach between the lock and floor/ceiling, z_e. There are two cases: case a) where the 'lip' of the mouth is the closest to the wall, and case b) where the back of the lock is closest to the wall. ϵ and σ control the steepness of the soft wall repulsion and c ensures that the potential is continuous at the point where the wall stops influencing the system. We refer to fig. 6.2 for greater clarity of these parameters. For $\epsilon = \sigma = 1.0$, the point of inflexion of these potentials is $3^{1/6}\sigma \approx 1.2$ (and $h - 3^{1/6}\sigma$). With this, $c = |3^{-1.5} - 3^{-0.5}| \approx 0.38$. We can see both functions, as well as a zero potential, plotted in fig. 6.2 for $h = 5$. We can observe that the soft potentials are asymptotic to the box edges.

[1] We note that the 9-3 Lennard-Jones potential was developed by considering the 12-6 Lennard-Jones potential [75] of a spherical particle near a wall.

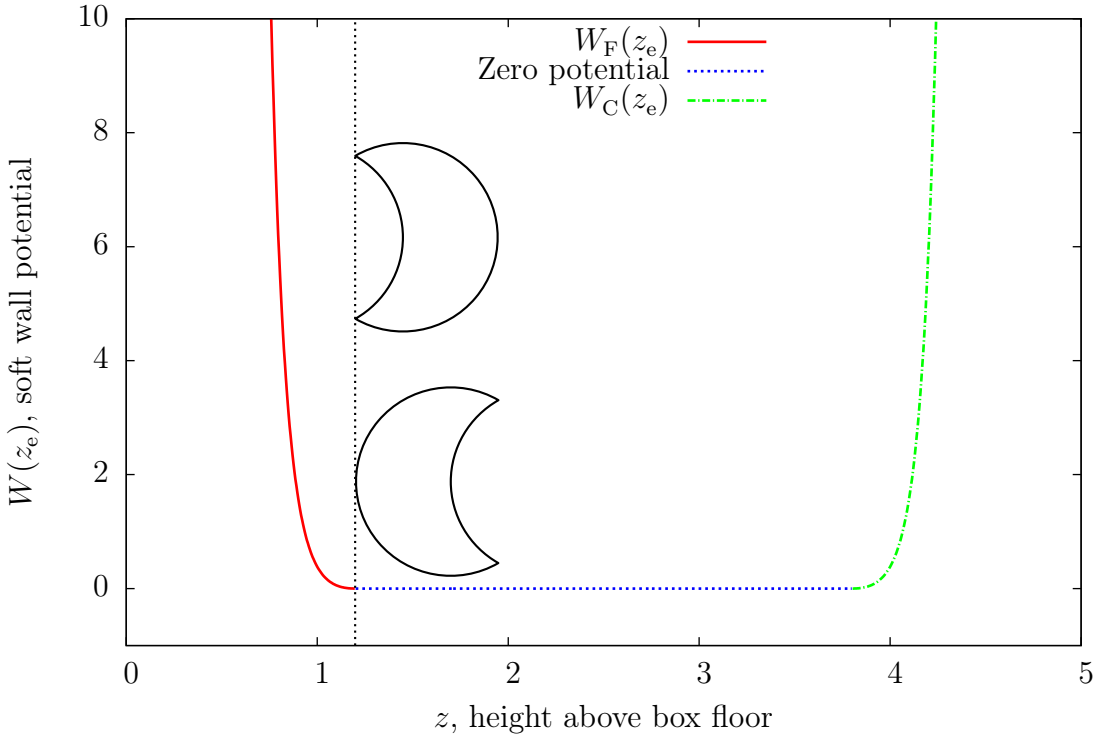

Figure 6.2: The soft potential, $W(z_e)$, models the floor and ceiling of the experiment and interacts with the closest approach of any locks, z_e, rather than their geometric centres. The inset images demonstrate the closest approach of the *centres*, z, of the locks to the potential before it becomes non-zero.

6.2.2 Small Translation & Rotation Monte Carlo

In the Monte Carlo algorithm, the standard Metropolis acceptance criterion is simply

$$P_{\text{acc}} = \min(1, \exp[-\beta \Delta E]) \tag{6.3}$$

where $\Delta E = E_f - E_i$ is the energy difference of the final (proposed) and initial Monte Carlo move. We apply small translational and rotational steps to a lock to simulate the thermal motion of a real lock suspended in a fluid. The translational vector is chosen randomly within a sphere of radius ϵ, centred at the original lock position. The rotational step was performed by choosing a small random rotation of ϵ_r about a randomly chosen axis.

With gravity and a soft potential wall, the energy difference related to a move for a single particle becomes

$$\Delta E = \Delta E_g(z_c) + \Delta V(z_e) \tag{6.4}$$

where $\Delta E_g(z_c)$ represents the energy difference of a lock in its original and proposed position suspended in a fluid with gravity, and $\Delta V(z_e)$ represents the analogous energy difference due to the soft wall potentials (which are only non-zero near the soft potentials, V_C and V_F, of the floor and ceiling of the box). This equation also assumes that there are no particles overlapping with the particle being moved. The energy difference due to gravity and buoyancy can be written as (Appendix D)

$$\beta \Delta E_g(z_c) = \frac{G\left(z_{c,f} - z_{c,i}\right)}{\sigma} \tag{6.5}$$

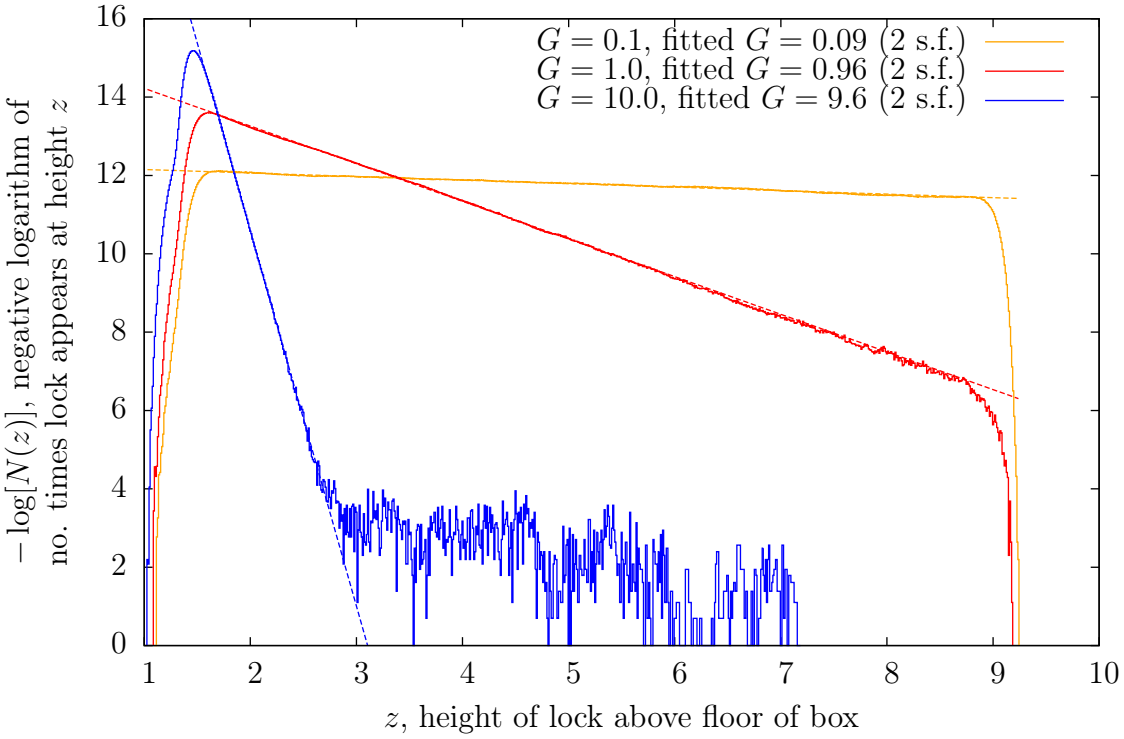

Figure 6.3: Showing the negative logarithm of the frequency that a lock appears at a specific height, i.e., $-\log[N(z)] \propto -Gz$ for G =0.1, 1.0 and 10.0. We observe a good agreement for the fitted G. All three systems have a size of $h^3 = 10^3$, with 10 locks, 10 million Monte Carlo sweeps (rotation/translation), $d_c = r_c = r_L = 0.5$, maximum move size of $a = 0.67$, maximum rotation of 2.0, and a soft potential boundary condition for the floor and ceiling ($z = 0$, $z = h$)

where $z_{c,f}$ and $z_{c,i}$ are the z-coordinates of the centres of mass centre of mass of the proposed (or final) and initial positions of a lock, and G is the strength of the gravity in our box. In terms of model parameters, we define the strength of gravity as $G = \sigma\beta g m_0$, where β and g are the typical inverse thermal energy and gravitational acceleration, and m_0 is the (reduced) mass of our lock. We refer to Appendix D for a fuller description. We make the assumption that the centre of mass of the lock will play an important part in the 'decrystallisation' process we are trying to match. Therefore, the z coordinate used in eq. (6.5) is the centre of mass, whilst the z coordinate used in the soft potential, z_e, is the aforementioned closest approach coordinate.

Subject to the soft potential boundary condition, we expect the number density of locks to have a decaying exponential correlation to gravitational field strength, G, i.e.,

$$N(z) \propto \exp\left(\frac{-z}{\ell_G}\right), \tag{6.6}$$

where we make a note that $\ell_G = \sigma/G$ is the gravitational length. This relation is confirmed in fig. 6.3, where we note an initial rise in number density close to the soft potential wall, before the expected exponential decay.

Figure 6.4 shows the result of gravity and a soft potential floor upon a collection of locks in a box. For this particular setup, where the strength of gravity, G, is 10 and lock density, ρ_L, is ~ 0.026, there is a preponderance for locks to point lock 'up' and, to a lesser extent,

to point down. We are using a small density of locks because eq. (6.6) assumes there are no interactions between locks, which is only valid for low densities. When a lock points down, its geometrical centre is lowered compared to a lock pointing up, hence the lower height near $n_z = -1$. If we perform the simulation with soft potentials at the floor and ceiling of our box, but at the same time, remove any gravitational bias, we would expect the geometrical centre of the closest approach of a lock pointing down to be at 1.45σ above the floor of the box. For an up-facing lock, this would be at 1.7σ. A gravitational bias forces these positions to be lower. For fig. 6.4, they are roughly 1.3σ and 1.5σ, respectively.

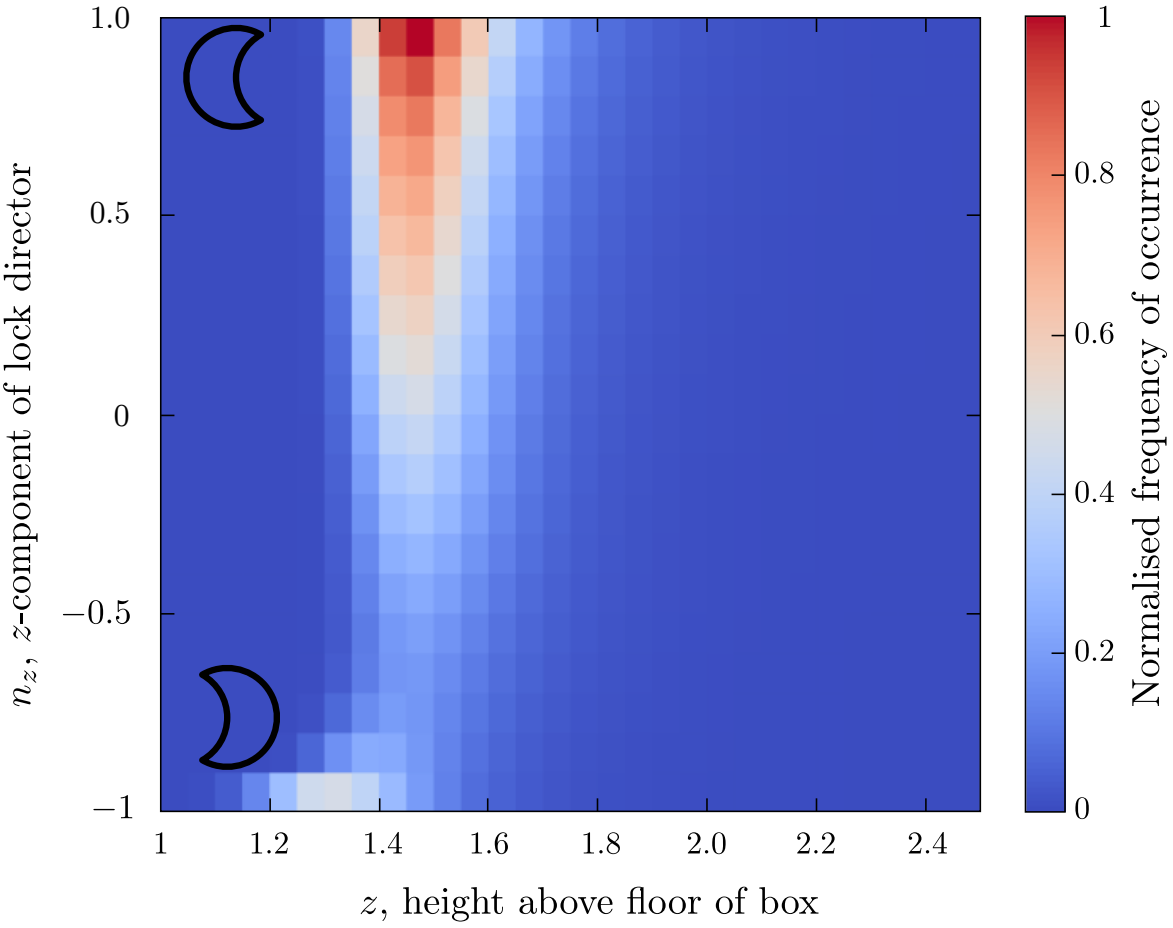

Figure 6.4: For a system of 50 locks in a 10^3 box, under the influence of a gravitational field strength ($G = 10.0$) acting in the z direction, this figure shows the normalised frequency of occurrence of the z-component of the directors at a height z above the floor of a box.

6.2.3 Correlation Functions of Motion

To ensure that our Monte Carlo simulation of a lock's motion is realistic, we present two correlation functions that deal with the translational and orientational behaviour of a lock.

To a good degree of approximation, without a gravitational field, a lock's translation movement is that of a three-dimensional random walker. We now present an argument used to test whether our particle is diffusing realistically. As a result of this argument, we can also connect the simulated motion to realistic time.

The mean square displacement of a diffusing particle is proportional to the real time, t,

$$\langle \delta x^2 \rangle = 6Dt \tag{6.7}$$

where D is the translational diffusion constant. The variance of a random walker's translational movement is equal to the average step size, $\langle\epsilon\rangle$, multiplied by the number of steps taken, N_s:

$$\langle|\boldsymbol{\delta x}|^2\rangle = N_\mathrm{s}\langle\epsilon^2\rangle. \tag{6.8}$$

How do we relate a Monte Carlo translation to real time? For translational motion, we can equate eq. (6.7) and eq. (6.8) if we relate the real time to the Monte Carlo steps of a simulation, i.e.,

$$6Dt = N_\mathrm{s}\langle\epsilon^2\rangle. \tag{6.9}$$

In a Monte Carlo simulation, the maximum move size is known and has units of σ^2. Therefore, we can rewrite eq. (6.9) with a reduced average step size, $\langle\tilde{\epsilon}^2\rangle$

$$6Dt = N_\mathrm{s}\langle\tilde{\epsilon}^2\sigma^2\rangle. \tag{6.10}$$

Rearranging eq. (6.10), we have

$$N_\mathrm{s}\langle\tilde{\epsilon}^2\rangle = 6\tilde{t} \tag{6.11}$$

where the reduced time is defined as

$$\tilde{t} \equiv \frac{Dt}{\sigma^2}. \tag{6.12}$$

A hypothetical experimental measurement of lock and key colloids will have a known colloid diameter, σ, diffusion constant, D, and duration, t, from which one can calculate the reduced time, $\tilde{t}$. One can then use eq. (6.11) to determine the number of Monte Carlo steps, N_s, needed for simulation (where the maximum move size, a, is related to the average step size, ϵ, as $\langle\epsilon^2\rangle = a^2$).

Figure 6.5 plots the reduced time, $\tilde{t}$ against the variance of the lock's translational motion, $\langle\delta x^2\rangle$, which is also known as the mean squared displacement (MSD). For a system of N locks, we calculate the average MSD as

$$\langle\delta x^2\rangle = \frac{\sum_{i=1}^{N}\langle[r_i(\tilde{t}) - r_i(0)]^2\rangle}{N} \tag{6.13}$$

where $r_i(\tilde{t})$ is the position of lock i at (reduced) time $\tilde{t}$. We can see that the fitted gradient of fig. 6.5 is in agreement with eq. (6.11), confirming that our Monte Carlo translational moves are similar to the diffusion of a real particle.

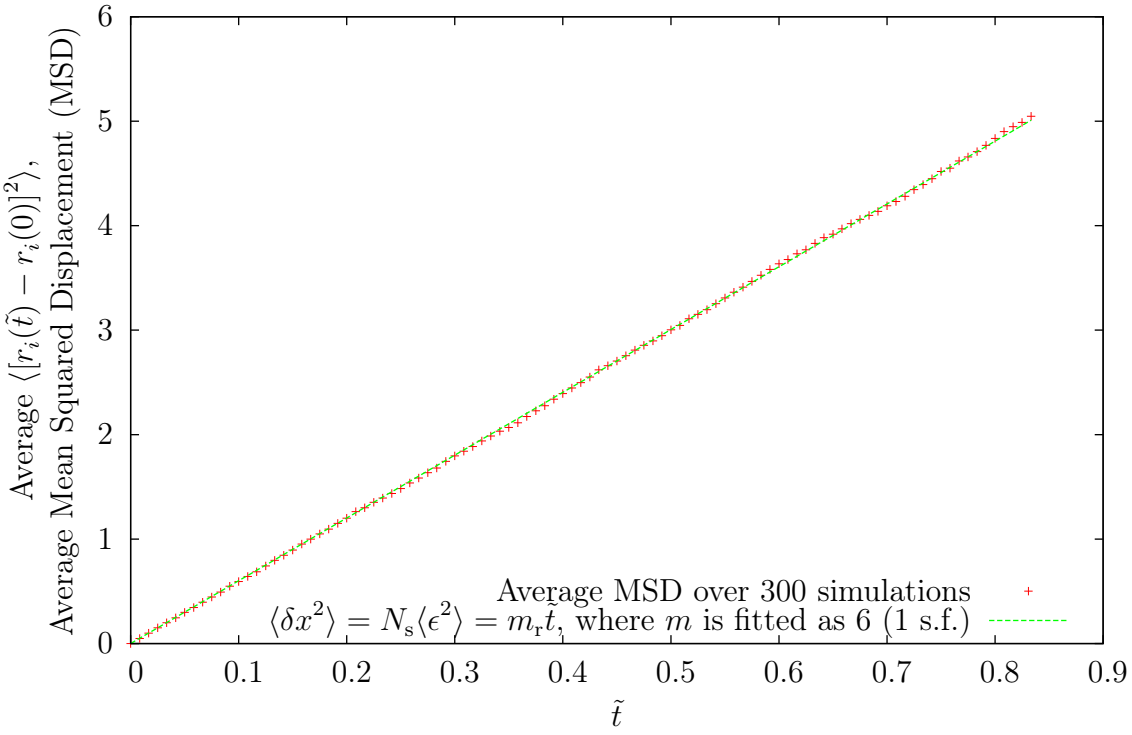

Figure 6.5: The average mean square displacement over 300 simulations of a dilute solution of locks in a large box (10 locks, $\sigma = 1$, 10^3 box volume). The simulations ran for 1000 Monte Carlo steps. We can map this to a reduced time, $\tilde{t}$, through eq. (6.11).

We also expect a lock in suspension to rotate in a similar way to a rotating sphere in a fluid if there is no gravity. We will show that there is a simple way to tell whether a locks are being rotated realistically, and we further show that this rotation can be related to the translational motion. Taken together, we can test whether our locks' motion are being realistically modelled.

If, for an evolving system of dilute locks, we take the average of the dot product between each lock's director at time t, $n_i(t)$, and at $t = 0$, $n_i(0)$, we expect a value at $t = 0$ of unity as the locks have not moved. At long times, we expect the locks to completely decorrelate from their original orientations as the Monte Carlo algorithm is ergodic. In medium times, we expect this value to decay quickly and smoothly (if our locks are sufficiently dilute to avoid interactions) from 1 to 0. This behaviour, in 3D, is described with the director dot product (DDP):

$$\langle \hat{n}_i(t) \cdot \hat{n}_i(0) \rangle = \exp(-2D_r t) \tag{6.14}$$

where D_r is the rotational diffusion constant that controls the rate at which a lock spins and hence the decay length of eq. (6.14)[2].

We observe that fig. 6.6 satisfies eq. (6.14). In a special case of the Einstein relation, known as the Stokes-Einstein equation, a spherical particle in a low Reynolds number fluid has rotational diffusion constant[3] of

$$D_r = \frac{1}{\pi \beta \eta \sigma^3} \tag{6.15}$$

[2]For a stricter derivation, see, e.g., Barrat and Hansen [76, pp. 235–236]

[3]See, e.g., Kimmich [77, p. 87] or the original derivation by Debye [78].

and a translational diffusion constant [76, p. 223] of

$$D = \frac{1}{3\pi\beta\eta\sigma}, \tag{6.16}$$

so that

$$D = \frac{D_{\mathrm{r}}\sigma^2}{3}. \tag{6.17}$$

6.2.4 Real Time Translation & Rotation

Equation (6.17) connects the translational diffusion constant, D, with the rotational diffusion constant, D_{r}. Using eq. (6.17), the concept of reduced time, $\tilde{t}$, introduced in previous discussion of translational motion and eq. (6.14), we show that our Monte Carlo rotation step is commensurate to a rotating particle in a low Reynolds number fluid. If we substitute real time from eq. (6.12) into eq. (6.14), we obtain

$$\langle \hat{n}_i(t) \cdot \hat{n}_i(0) \rangle = \exp\left(\frac{-2D_{\mathrm{r}}\tilde{t}\sigma^2}{D}\right). \tag{6.18}$$

If we use the Stoke-Einstein connection between D and D_{r} (eq. (6.17)), we then arrive at

$$\langle \hat{n}_i(t) \cdot \hat{n}_i(0) \rangle = \exp\left(-6\tilde{t}\right). \tag{6.19}$$

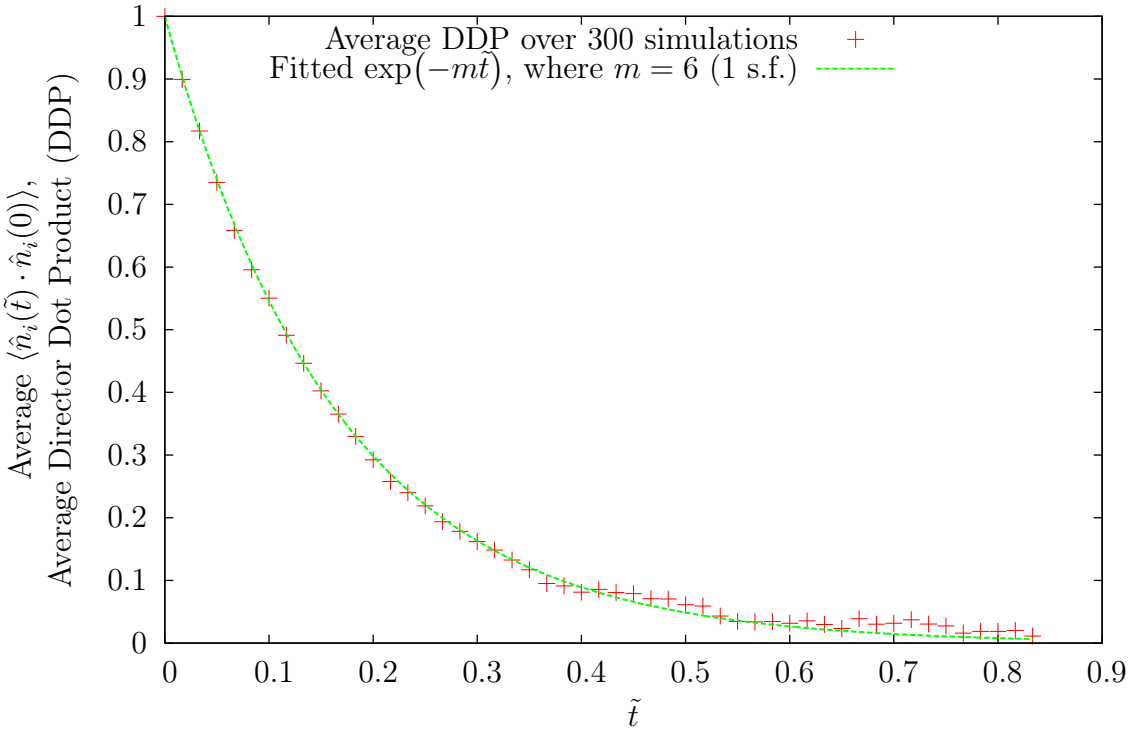

Figure 6.6: The average director dot product over 300 simulations of a dilute solution of locks in a large box (10 locks, $\sigma = 1$, 10^3 box volume). The simulations ran for 1000 Monte Carlo steps. We can map this to a reduced time through eq. (6.11).

Hence, for a system of N locks, fig. 6.6 shows the average DDP, given as

$$\langle \hat{n}(\tilde{t}) \cdot \hat{n}(0) \rangle = \frac{\sum_{i=0}^{N} \langle \hat{n}_{\mathrm{i}}(\tilde{t}) \cdot \hat{n}_{\mathrm{i}}(0) \rangle}{N} \tag{6.20}$$

against the reduced time, $\tilde{t}$. We can see that there is agreement with eq. (6.19). Together with fig. 6.5, we state that our locks are diffusing and rotating in a similar fashion to a spherical particle suspended in a fluid.

6.3 Correlation Functions

Here, we introduce the tools used to study the static and time-dependent characteristics of our sedimenting system.

6.3.1 Many Independent Snapshots

The radial distribution function and the to-be-defined bond orientational order parameter refers to one 'snapshot' of a continuously changing system of particles. In practice, these measurements are equivalent to sampling from a small 'time window' or range of snapshots in a long running computer simulation. In a time-dependent simulation, this range of snapshots could be obtained from many independent simulations. In this section, any angle brackets refer to an average over many independent configurations. We can improve this estimate of the average by also averaging over a 'time window' within each simulation.

6.3.2 2-D Radial Distribution Function

The 2-D radial distribution function is calculated by:

$$g_{2\mathrm{d}}(r) = \langle \frac{n(r)}{N_{\mathrm{tot}}} \frac{A_{\mathrm{tot}}}{2.0\pi r \delta r} \rangle. \tag{6.21}$$

$g_{2\mathrm{d}}(r)$ describes the probability of a particle in a 2-D system to be located at any distance, r, from any other particle, normalised by an equivalent probability distribution for an ideal gas particle. $n(r)$ denotes the number of particles at a given distance, r. A_{tot} is the total area that our particles inhabit, whilst N_{tot} is the total number of occurrences in our particle's probability distribution.

6.3.3 Short and long range bond-orientational order parameters

The local, or short range, bond-orientational order parameter describes the extent that a particular particle, m, and its surrounding neighbours, j, are packed in a regular hexagonal lattice. Originally introduced by Nelson and Halperin [79][4], we sum the bond order

[4] In their paper, Nelson and Halperin [79] do not perform a sum over nearest neighbours. To be clear, their bond order parameter is denoted ψ whilst we denote our local hexatic bond-orientational order parameter with ψ_6 in the same fashion as Ivell et al. [57]

parameter of a particle's neighbours and normalise by the number of neighbours, N_{nbors}, to ensure that we have a measurement with a range of $[-1, 1]$, i.e.,

$$\psi_6(r_m) = \frac{1}{N_{\text{nbors}}} \sum_n \exp[6i\theta(r_{mn})] \tag{6.22}$$

where $\theta(r_{mn})$ is the angle between the vector connecting m and n and a fixed, arbitrary axis. For a perfectly hexagonal system $|\psi_6|$ is unity, whilst a completely disordered system would produce a zero ψ_6. An average ψ_6 for a system would be calculated as a simple sum over all particles, N, i.e.,

$$\langle \psi_6 \rangle = \frac{\sum_m^N |\psi_6(r_m)|}{N}. \tag{6.23}$$

The long range bond-orientational order parameter determines the long range system wide hexaticity by summing the imaginary and complex parts of $\psi_6(r)$ rather than the modulus:

$$\langle \chi_6 \rangle = \frac{|\sum_m^N \psi_6(r_m)|}{N}. \tag{6.24}$$

6.3.4 Bond-orientational order parameter

In a similar way to the radial distribution function, the bond-orientational order parameter can study how the ψ_6 component of a particle m is distributed at distance r relative to any other particle, n. This can be written as a double sum over all particles:

$$g_6(r) = \frac{\langle \sum_m^N \sum_n^N \psi_{6m}^*(r_m)\psi_{6n}(r_n)\delta(r_{mn} - r) \rangle}{\langle \sum_m^N \sum_n^N \delta(r_{mn} - r) \rangle} \tag{6.25}$$

where $\psi_{6m}^*(r_m)$ refers to the complex conjugate of the ψ_6 component of m, and $\psi_{6n}(r_m)$ refers to any other particle, n, at radius r. The delta functions act to discount any particles that do not lie a distance r apart.

6.4 Results

Unless otherwise specified, our units are always in units of σ, where σ is the diameter of a sphere with a radius of r_{L}. Our locks have a r_{L} of 0.5, our box size is $10\times10\times10$, our rotation size is 0.1 and our step size is 0.033.

6.4.1 Quasi-2D System

We can observe from fig. 6.7 that distinct layers are forming at evenly spaced distances in height. Most of our measurements will be concerned with the bottom-most layer of locks. From fig. 6.7, we have chosen $z = 2.1$ as the cut-off for the bottom most layer of locks. If we focus on this bottom layer, we can make an argument that due to the pressure of the upper layers of locks, the subsystem of bottom-most locks can be said to be quasi-2D. By quasi-2D, we mean that the locks on this bottom layer act as though they are *confined* in this layer. The prefix 'quasi' can be qualified by fig. 6.8 where we see evidence of the interlayer

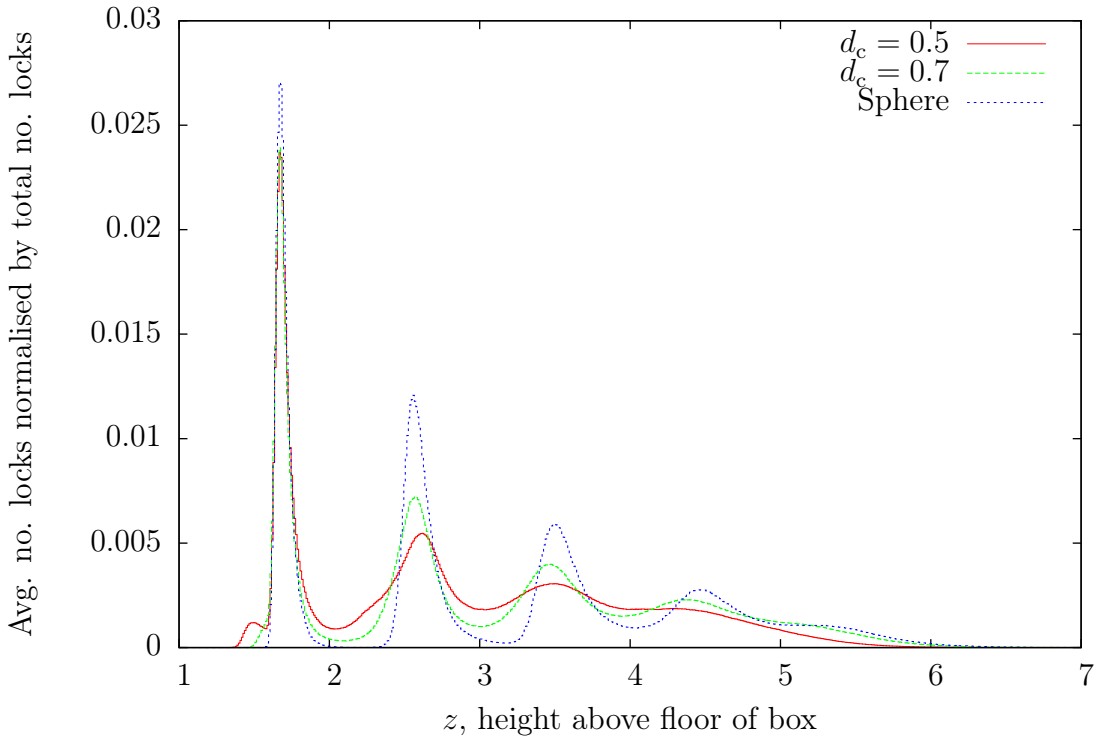

Figure 6.7: The average number of particles at a specific height, z, in the box normalised by the total no. particles in the box over 4 separate simulation runs (locks with $d_c = 0.5$, 0.7 and spheres) in a system of size $10 \times 10 \times 10$, with 350 particles and gravitational field strength of 5 and a soft wall ϵ of 100.0. One can compare these density distributions to studies of spherical particles under gravity in, e.g., [80–82]

particle movement. For long enough time, we expect all particles that were initially at the bottom-most layer to have swapped with particles above it. Indeed, we see this begin to happen. We see that for shallower locks the interlayer swapping increases. We also note that though the number of locks in the bottom layer fluctuates, it is still relevant to talk about a quasi-2D nature due to the relatively low range. Intriguingly, the decay of locks of $d_c = 0.8$ is distinct from other geometries. We will discuss the $d_c = 0.8$ geometry in depth.

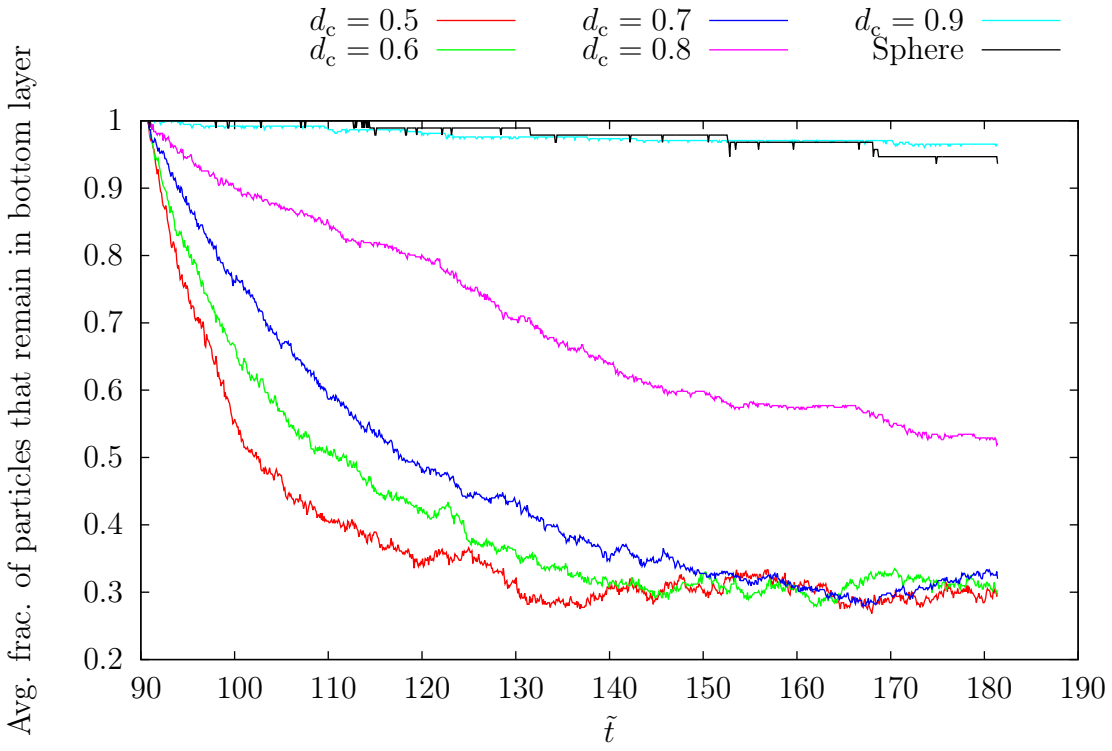

Figure 6.8: The fraction of locks with $d_c = 0.7$, 0.8 and spheres that remain in the bottom layer of a system (from $\tilde{t} = 50\%$ onwards) of size $10 \times 10 \times 10$, with 350 locks and gravitational field strength of 5 and a soft wall ϵ of 100.0. The data from the sedimenting locks were averaged over 4 separate simulation runs.

6.4.2 Quasi-2D melting

Here, we present evidence that there is a transition from a liquid to a solid phase as we make our locks increasingly shallow. For $d_c = 0.5$, 0.7 and spheres, we plot the two-dimensional pair distribution function at long times in fig. 6.9 and the corresponding bond-orientational correlation function in fig. 6.10. We note the characteristic long-range positional and orientational oscillations of the spherical system that are a strong indicator that this system is crystalline. In the case of $d_c = 0.7$ and 0.5, we note the typical decay of $g_{2d}(r)$ to unity and $g_6(r)$ to zero is a hallmark of the liquid phase.

In fig. 6.9, we highlight the 'shoulder' for $d_c = 0.5$ that slowly converges to a single peak as the lock mouth becomes shallower. This shoulder corresponds to lock-lock chaining and is very useful feature in identifying what type of system we are studying. We note particularly that the periodicity of these graphs is affected by the lock depth. If we consider just three locks in a closely packed row, there are many different arrangements. Examples of these arrangements include (where the first lock is on the left) 1. having the first two locks pointing left, but the third lock pointing to the right, 2. having all the locks pointing left, 3. having all the locks pointing *upwards* and so on. Each of these permutations will have a different radial distribution function, and we can trace the influence of the most likely ones in fig. 6.9. The common feature amongst these graphs is the peak at $r = 1$, which corresponds to a lock being an indented sphere of diameter $\sigma = 1$.

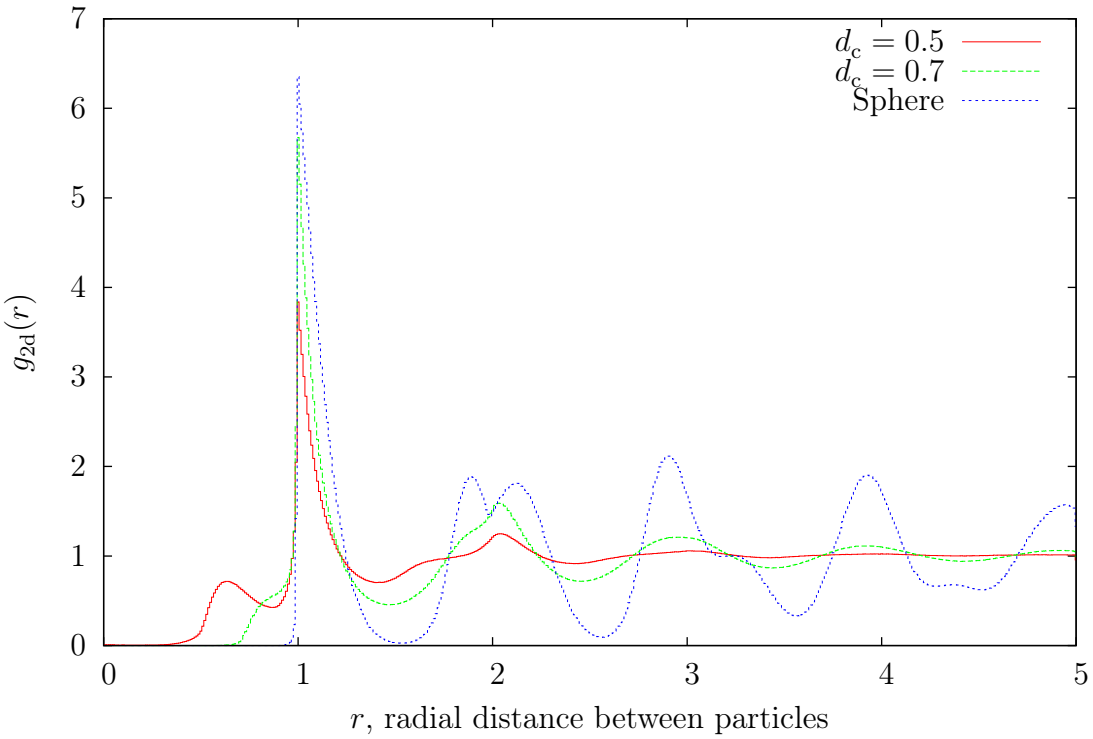

Figure 6.9: The average $g_{2d}(r)$ over 4 separate simulation runs for locks with $d_c = 0.5$, 0.7 and spheres at the bottom layer of a system of size $10 \times 10 \times 10$, with 350 particles and gravitational field strength of 5 and a soft wall ϵ of 100.0. Take note of the 'shoulder' for $d_c = 0.5$ and $d_c = 0.7$ located at $r \approx 0.5$ and $r \approx 0.7$, respectively, associated with lock-lock chaining. r is the two dimensional radial distance between the particles.

Looking at fig. 6.10, we see also a common peak at $r = 1$ that corresponds to a lock with an indented sphere of diameter $\sigma = 1$. We have already discussed that $d_c = 0.5$ and 0.7 decaying to zero is a hallmark of a fluid. Having a non-zero value, as in the sphere case, is a hallmark of a solid. We can make a tentative case that the deeper the lock, the quicker $g_6(r)$ decays to zero.

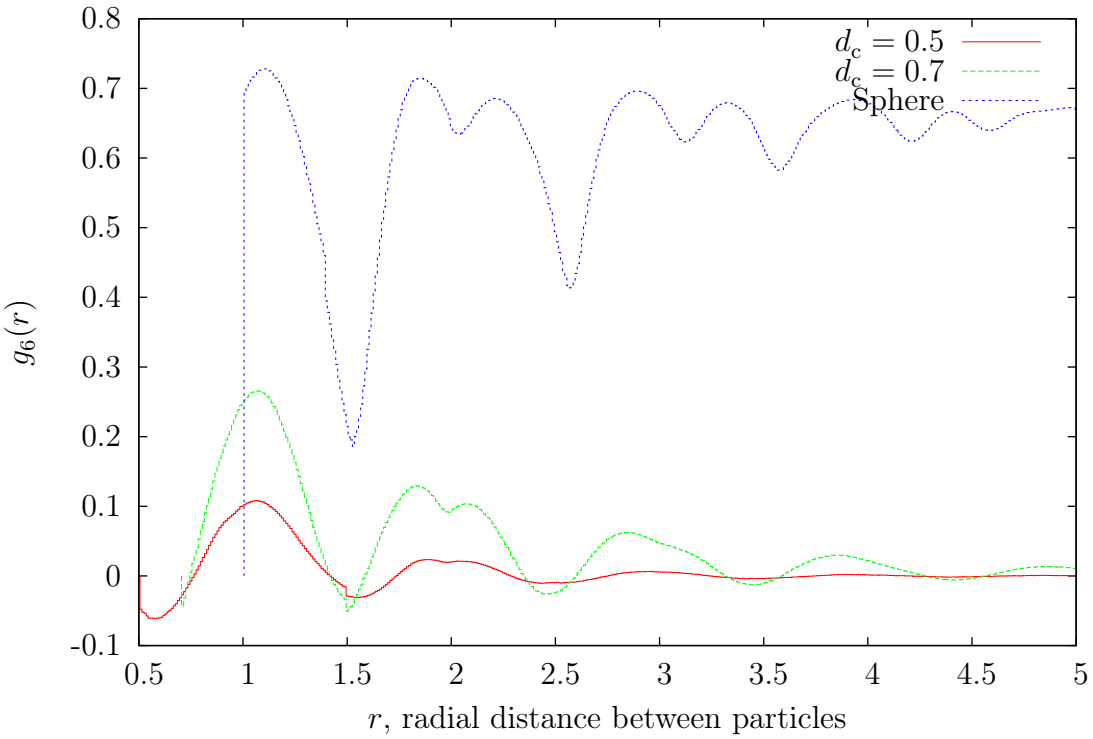

Figure 6.10: The average $g_6(r)$ over 4 separate simulation runs for locks with $d_c = 0.5$, 0.7 and spheres at the bottom layer of a system of size $10 \times 10 \times 10$, with 350 particles and gravitational field strength of 5 and a soft wall ϵ of 100.0. Note that r is the two dimensional radial distance between the particles.

Figure 6.11 highlights that $d_c = 0.5$ has a higher number of (longer) lock-lock chains. Further evidence of the liquid and solid phase are observed in fig. 6.12 where the average short range bond-orientational parameter is plotted for the lifetime of the simulation. The spherical system has a high $\langle \psi_6 \rangle$ of ~ 0.85, whilst the $\langle \psi_6 \rangle$ of $d_c = 0.5$ and 0.7 is a lower ~ 0.55 and ~ 0.42, respectively.

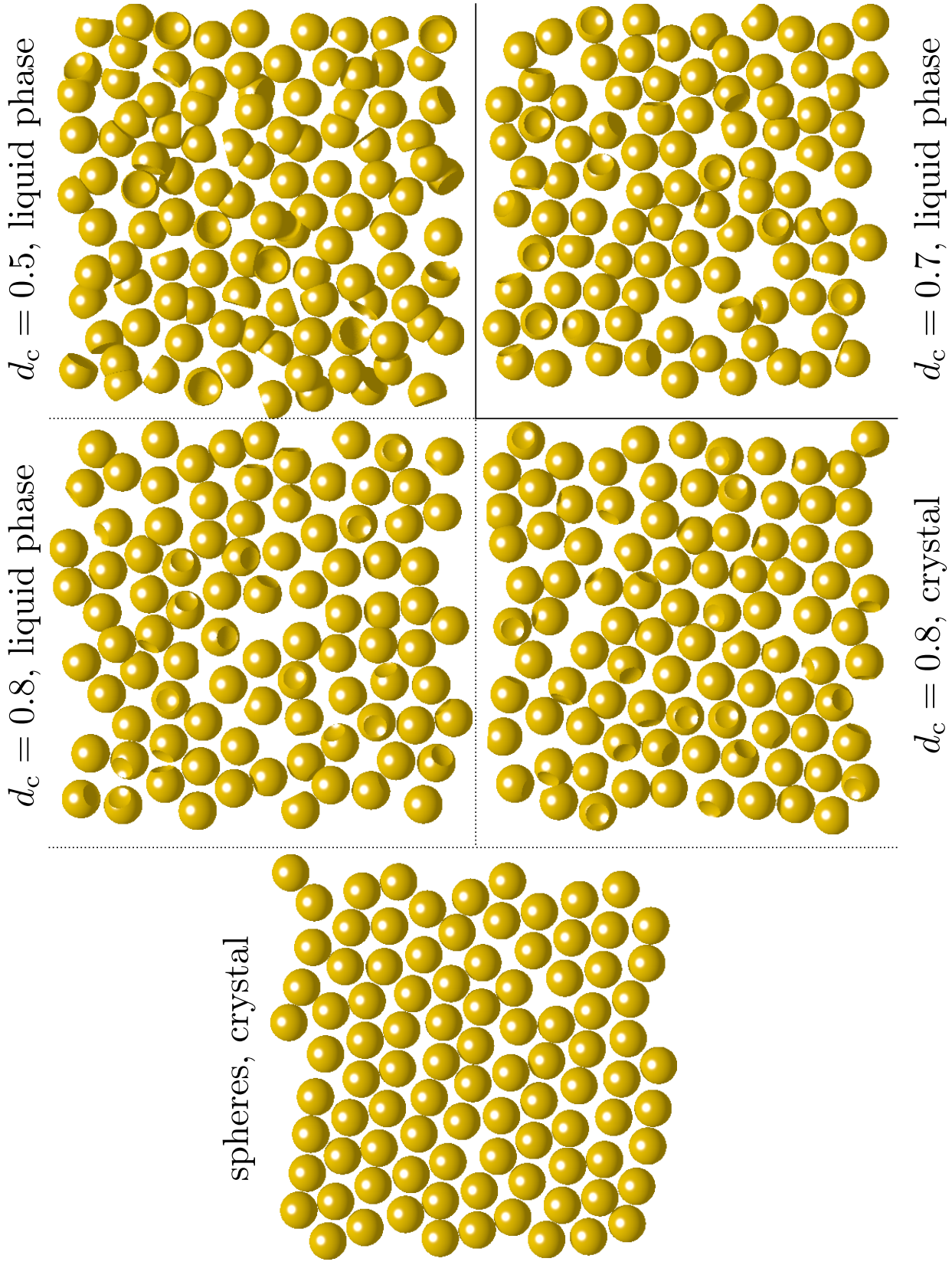

Figure 6.11: 3D visualisation, looking 'upwards' from the bottom of the box, of the bottom-most layer of four sedimenting systems. $d_c = 0.5$ and $d_c = 0.7$ demonstrate a disordered liquid that incorporates lock-lock chaining. $d_c = 0.8$ is shown twice: on the left in the liquid state and on the right in a solid state. The spherical system is shown to demonstrate an almost perfect solid or crystalline state. We can observe a liquid to solid transition from $d_c = 0.5$ to $d_c = 0.8$.

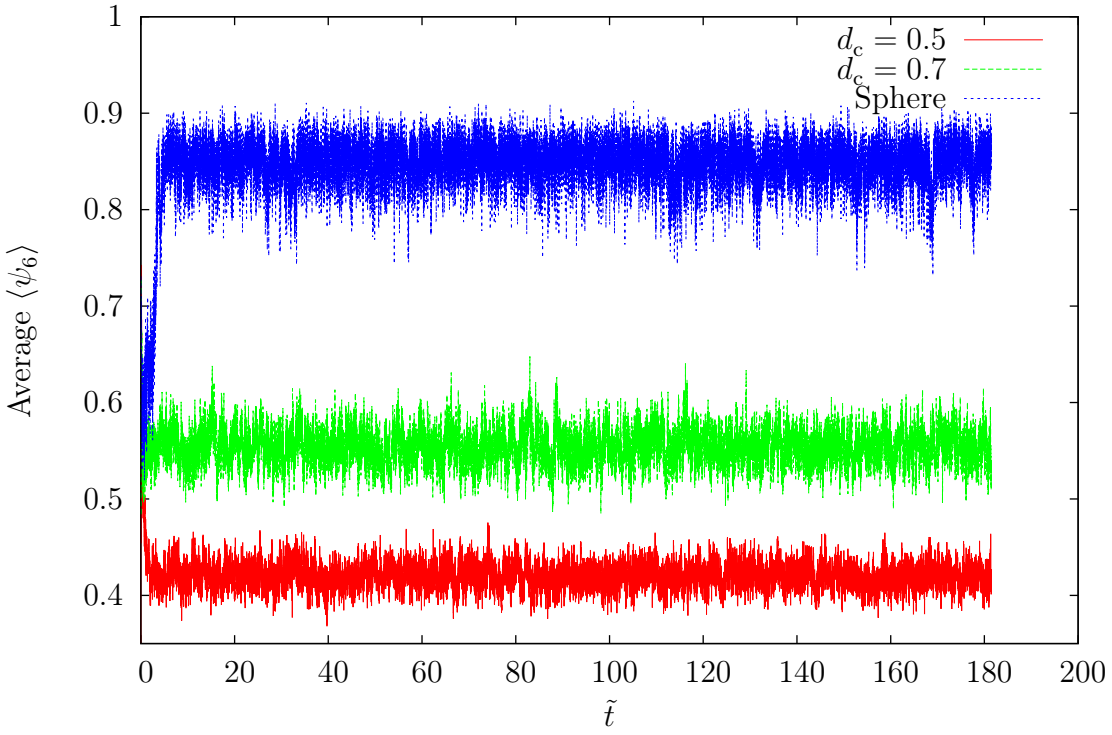

Figure 6.12: The average ψ_6 measurements of locks with $d_c = 0.5$, 0.7 and spheres at the bottom layer of a system of size $10 \times 10 \times 10$, with 350 locks and gravitational field strength of 5 and a soft wall ϵ of 100.0. This figure was averaged over 4 separate simulation runs.

6.4.3 Fluctuating Measurements between Solid and Liquid

Figures 6.13 and 6.14 plot the average ψ_6 and average χ_6 of the bottom-most layer of locks of varying geometries, respectively, over the life times of single simulation runs. Together with fig. 6.11, they show that a lock with $d_c = 0.8$ fluctuates between the solid and liquid phase.

In the bottom-up snapshots, we can visually identify two phases. The left hand image of $d_c = 0.8$ looks like a liquid whilst the right hand image looks like a solid. $d_c = 0.5$ and 0.7, as seen, are definitely in a liquid state, though the former has a few more lock pairs and triplets. We show a spherical system on the bottom-most pane to demonstrate a sedimented crystalline system for comparison.

In figs. 6.13 and 6.14 we show the average long and short range order parameters through time, respectively, for a single system. We display $d_c = 0.7$ and the spherical system for comparison to $d_c = 0.8$, where we see fluctuation between a value close to the spherical system's solid phase and a deeper lock's liquid phase. The corresponding probability distributions in right hand pane of figs. 6.13 and 6.14 show single peaks. From the broader peaks at $d_c = 0.8$, we can remark that we probably do not see a discontinuous first order jump between solid and liquid phases.

Aside from the question of phase transitions, there is at least some different, distinct behaviour at $d_c = 0.8$ which we can observe in fig. 6.8. At this particular lock geometry, there appears to be a unique decay length of the average fraction of particles that remain in the bottom layer from $t = 50\%$ onwards.

With the evidence presented, we are quite confident that a phase transition from between solid and liquid is shown. We also posit that the bottom-most layer of sedimented lock colloids exhibits quasi-2D melting controlled by lock depth. There are at least two possibilities as to the nature of this melting.

1. A simple discontinuous phase transition from solid to liquid. This phase transition is what we normally observe in 3D ice-water.

2. A continuous phase transition involving an intermediate hexatic phase. Possibilities for this include KTHNY theory [83], or similar phase transitions to those seen by Bernard and Krauth in his 2D hard disk simulation [84].

To confirm whether our system possesses a hexatic intermediary stage or simply fluctuates between liquid and solid, we offer three suggestions of future work:

- Locate the liquid-hexatic transition by sweeping through d_c below 0.8.
- Simulate a large lock system (on the order of a million particles) at the d_c associated with phase transition to determine if phase coexistence is present
- Determine if the high density coexistence phase is hexatic or liquid by decreasing lock depth and analysing if the positional correlation order decays exponentially

We also point to experiments performed on colloids confined between 2D glass plates to study their quasi-2D phase transitions [85]. It may therefore be illuminating to compare characteristics of our multi-layer system to a very *thin* box such that the soft potential of the ceiling acts like multiple layers of locks.

Reaching back to the experiment [57] that began this computer study, we find that we do not see any constant decrystallisation with time but rather a fluctuation between two phases. We can suggest at least two explanations for this: 1. the dynamics in the experimental study are much slower and therefore the system has not truly sedimented 2. we have missed an important physical characteristic, e.g., the rounded mouth edges of the lock. Therefore we propose the study of the characteristics of our system at 'short' times, i.e., at the initial point of the locks forming a layer at the bottom. To be able to observe this quasi-2D melting in experiments, one may need to wait longer than 48 hours.

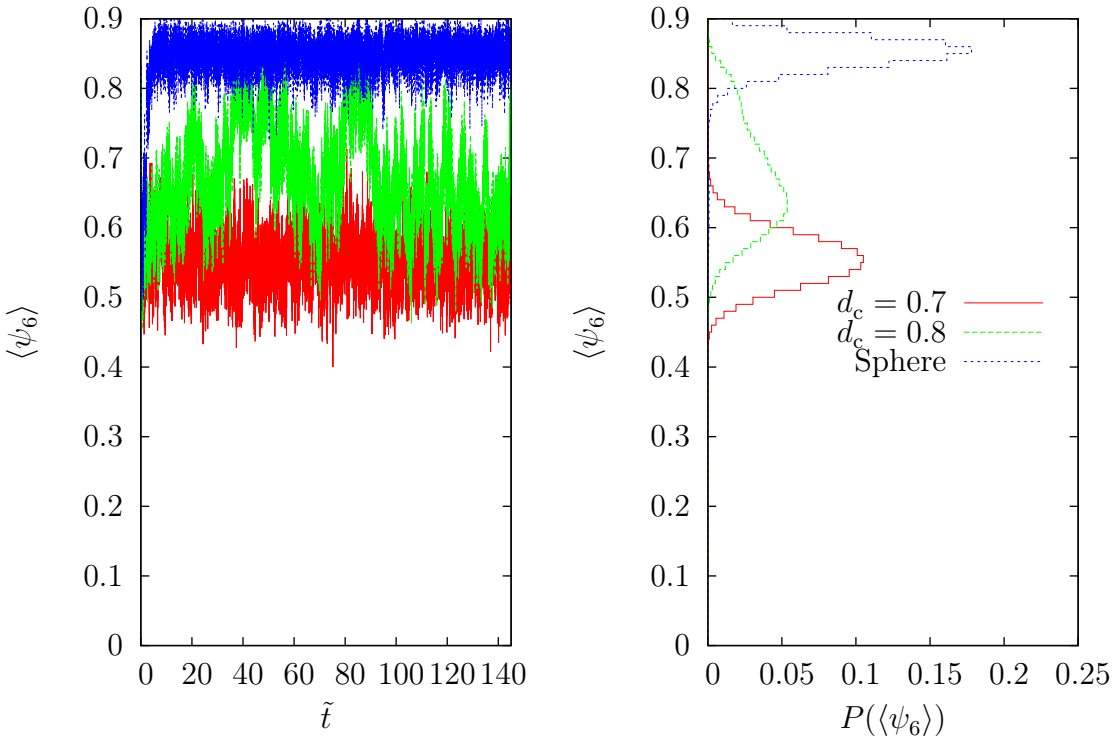

Figure 6.13: The ψ_6 measurements of locks with $d_c = 0.7$, 0.8 and spheres at the bottom layer of a system of size $10 \times 10 \times 10$, with 350 locks and gravitational field strength of 5 and a soft wall ϵ of 100.0. The data has been taken from single simulation runs. Note that $d_c = 0.9$ is very similar to the sphere like measurements and so is not shown.

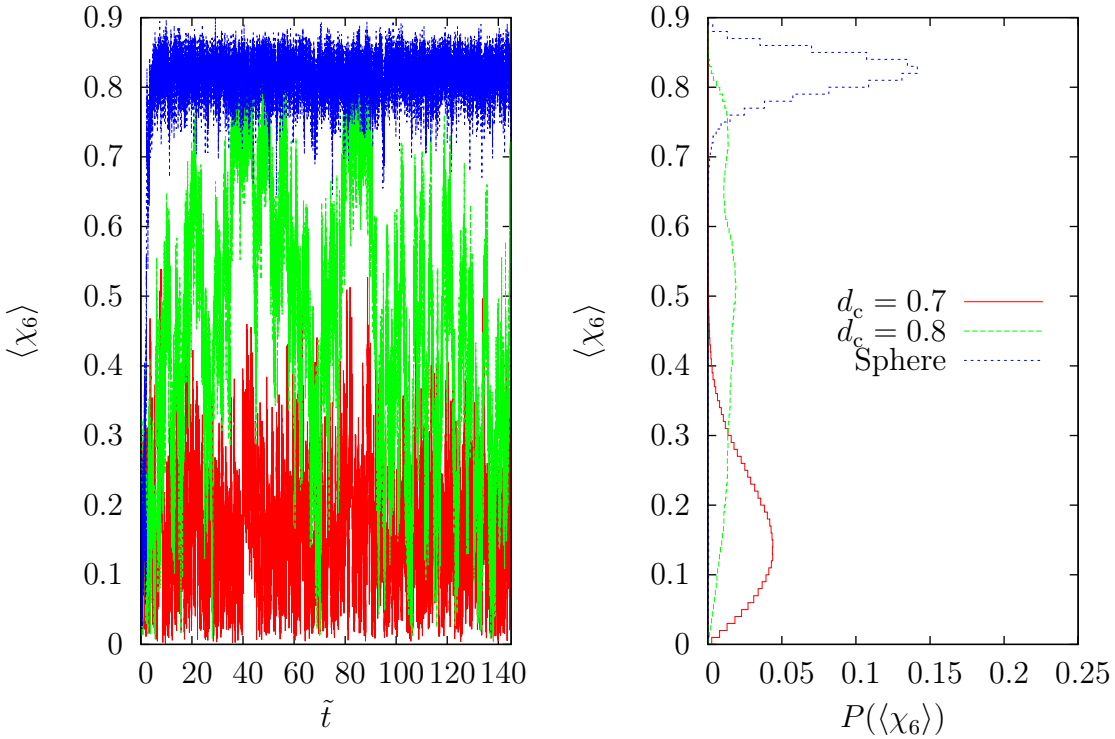

Figure 6.14: The χ_6 measurements of locks with $d_c = 0.7$, 0.8 and spheres at the bottom layer of a system of size $10 \times 10 \times 10$, with 350 locks and gravitational field strength of 5 and a soft wall ϵ of 100.0. The data was taken from single simulation runs. Note that $d_c = 0.9$ is very similar to the sphere like measurements and so is not shown.

6.5 Conclusion

In conclusion, we have presented an interesting experimental system of sedimenting locks and simulated a similar set up. We noticed that the fluctuating bond-correlating order parameter for a specific geometry of lock probably points to a classic discontinuous solid-liquid transition and may point to an analogous 2D melting of hard disks - tunable instead by lock depth - and have proposed further work to investigate this. We have also proposed reasons for why our simulated setup does not produce decrystallisation over time and have suggested further work to investigate this.

Chapter 7

Outlook

7.1 Discussion

The initial and primary aim of this thesis was to produce a workable method to parametrise the depletion potential due to nanoparticles for a lock and key colloid [38]. The cornerstone of this whole process was the partitioning of the two-dimensional effective potential into sensible regions. We conclude by assessing the progress made and suggesting future avenues of research based upon the findings made.

The parametrisation of the depletion potential seems to follow a by now established pattern. Firstly, one chooses an appropriate, simple, coordinate system in which to represent the depletion potential. A lot can be said for how important this first step is, as a more complicated coordinate system can hinder later steps. The lock and lock system is a primary example of this, as we showed that it could be reduced from six degrees of freedom to four.

Secondly, after representing a depletion potential with this coordinate, one carves it up into regions of characteristically different behaviour. With regards to this, we believe we have a developed a terse but powerful notation that allows one to address the degrees of freedom that are the most important in a characteristic region and integrating out the less important degrees of freedom, whilst still keeping a macroscopically important system parameter (the second virial).

Thirdly, one then checks for self-consistency by running an explicit simulation and comparing with another simulation that is using the parametrised potential.

Thus, we have a prescription of creating an effective potential. We believe that this methodology can be extended to other anisotropic systems. The next section will address this, amongst other new avenues of potential work.

We have seen a good, and in some cases, excellent quantitative match between explicitly simulated lock and key colloids and their corresponding parametrised potentials. We bolstered this claim by testing a few state points against a recent paper by Ashton et al. [1], who explicitly simulated lock-only colloids, and found a good to excellent agreement with their measures. An important lesson to glean from the parametrisation exercise is the balance between parametrisation, granularity and simplicity. The more fine grained we make our parametrised potential, the better the microscopic match up between the model

and the real system, but the more opportunity for error. Of course, at the extreme end of fine-graining, one will inevitably ask why we do not load the whole two-dimensional into a giant 'look-up' potential. Rather than this brute force method, we believe in the elegance and simplicity of our prescription. On this point, we believe that matching the second virial is a very good route to continue upon.

We believe that the lock and key partition function developed was useful as a first check to verify whether the parametrisation functioned correctly, but quickly found that some of the simplifying assumptions limited the low packing fraction predictions. Past a certain packing fraction of nanoparticles, the predictions were very good despite the inbuilt Asakura-Oosawa nanoparticles rather than hard nanoparticles. There is much scope for improvement here, which we will discuss in the next section.

As a small aside, we also simulated and analysed a system of locks that, under the influence of gravity, sediment. We were inspired by the experiments of Ivell et al. [57], and though we did not discover a slow decrystallisation in time as they found, we found a novel tunable liquid-solid phase transition.

7.2 Future Work

In the introduction, we also claimed that the lock and key colloid is a good candidate for exploring depletion-mediated self-assembly. The bulk of this thesis dealt with the actual parametrisation of the effective potential, but now that the prescription for this is complete, there is much scope for further work.

As a first suggestion, one could pick up the suggestion by Ashton et al. [1], where they observed that strongly-branched (shallow) locks lead to clusters of bound locks that spanned the whole system, i.e., percolation. We could use the parametrised effective potential to simulate a large system and see whether percolation occurs, or if there are liquid-vapour, transitions. This would be a good avenue for exploring depletion-mediated self-assembly and a good test for the accuracy of the parametrisation.

If the granularity of our parametrisation is sufficiently fine, then we could explore the claim by Odriozola et al. [46] that there is a real, repulsive, barrier that a key travels around to dock with a lock mouth. This could proceed by simulating a lock and key colloid explicitly with event driven molecular dynamics [86][1] or a small step, small rotation explicit nanoparticle Monte Carlo with realistic Brownian dynamics and comparing a lock's motion with an equivalent small step, small rotation parametrised potential Monte Carlo scheme. We refer to our chapter of sedimenting locks for a quick reminder of the small step, small rotation Monte Carlo scheme.

There of course remains one last piece to completely describing the lock and key colloid. This piece is the inexactly matching two-lock system. We suggest a similar approach to the development of the mismatched lock and key colloid, i.e., noticing the common ground with the exactly matched two lock system and modifying the approach for the inexact case. Once this piece is complete, one has the entire lock and key parametrisation puzzle and

[1] A simulation technique that explicitly models the mass and velocity of a particle

can simulate, at the very least, a very large, poly-disperse, lock and key colloid to examine its character. There is much potential to this line of work.

In a similar vein, one should be able to apply the methodology we have developed to double, triple or n-locks, i.e., a sphere with multiple, spherical indentations. With this in place, one can explore the phenomenology of the colloidal rock, a cousin to the lock and key colloid, highlighted by Zhang [54].

It is a definite theoretical possibility to develop a partition function for a mismatched lock and key in a very similar fashion to how we derived the exact case. In fact, one can derive accompanying partition functions for the exact and mismatched two-lock system. Once this has been completed, a free energy comparison can be made to aid the development of future parametrised potentials. This will be discussed now.

Towards the challenge of the lengthy time taken to produce one parametrised potential, one can very realistically develop an interpolation scheme so that a parametrised potential that is near to a state point already explored can be estimated. One can use free energy curves - derived from partition functions - to test a newly interpolated potential.

On a grander scale, there are some important questions that we are now better suited to answer. As mentioned in the introduction (chapter 1), what conditions are needed for optimal self-assembly [47–53]? Furthermore, we could explore whether a lock and key are actually the best matching shapes for depletion-mediated self-assembly or whether there exists a 'better' set of shapes. More immediately, we are better equipped to answer the question of which particular geometry of lock and key colloid, and which nanoparticle packing density, lends it self to the most optimal self-assembly. To this end, we believe that the ideas of the equilibrium constant, which provides a good yard-stick for the density of locks needed for interesting self-assembly, will be a useful tool.

Touching base with existing anisotropic systems, there is much possible work to compare the lock and key interactions with patchy particles. This is an interesting path to explore as the explicit lock and key and nanoparticle colloid interacts by a different mechanism than the typical patchy colloid, yet in this thesis, we are essentially substituting the depletion mediated interaction for a 'complicated patch'. Some insight could be gained for how simple a patch is needed to maintain the same lock and key aggregates observed by [1, 38], and further, to what limit we need to reach to begin seeing more simple 'patchy' particle behaviour rather than lock and key behaviour.

On a connected point, perhaps a very shallow lock would exhibit similar behaviour to Baxter's adhesive hard sphere model at high temperatures [87] (i.e., attraction only at contact) whilst a deeper lock with a low nanoparticle concentration would resemble the same model at lower temperatures (i.e., the standard hard sphere model). If this is true, one could also use the parametrised effective potential at an appropriate Baxter-like regime, to study percolating clusters that were observed by Ashton et al. [1] in lock and keys, and in a true Baxter potential system by Miller and Frenkel [88]. The idea would be to use observations from the Baxter hard sphere system that Miller and Frenkel studied to inform a more complicated lock and key system.

As for the sedimenting lock-only system, there is much scope for exploring the exact

nature of the liquid-solid phase transition. To help with this, we propose a future work based upon the novel event chain Monte Carlo scheme due to Bernard et al. [89]. We believe that this will be a helpful simulation tool as it was used to solve the nature of the liquid-hexatic-solid phase transitions [84].

Appendix A

Exclusion Volume of Lock and Key

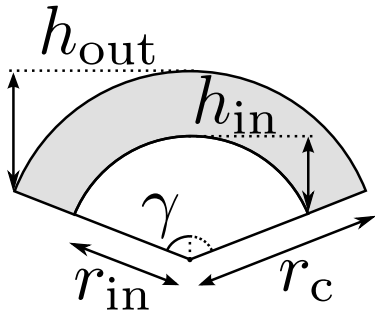

Figure A.1: A more detailed version of fig. 3.4(b)ii), where we note that γ is given by the geometric arguments shown in fig. A.2.

We can estimate the exclusion volume of fig. 3.4a) as approximately twice the volume of fig. 3.4(b)ii), i.e.,

$$\Delta V \approx 2V_{\text{b2}}. \tag{A.1}$$

Figure 3.4ii) is depicted more clearly in fig. A.1. Its volume is calculated through the subtraction of a smaller spherical cone [90, p. 106] (of height h_{in}) from a larger spherical cone (of height h_{out}), i.e.,

$$V_{\text{b2}} = \frac{2}{3}\pi(r_{\text{c}}^2 h_{\text{out}} - r_{\text{in}}^2 h_{\text{in}}), \tag{A.2}$$

noting that

$$h_{\text{out}} = r_{\text{c}} - r_{\text{c}}\cos\gamma \tag{A.3}$$

and

$$h_{\text{in}} = r_{\text{in}} - r_{\text{in}}\cos\gamma \tag{A.4}$$

where

$$r_{\text{in}} = r_{\text{c}} - r_{\text{n}}. \tag{A.5}$$

We also show fig. A.2 to demonstrate extra information that is helpful in calculating the explicit three-dimensional exclusion volume, ΔV.

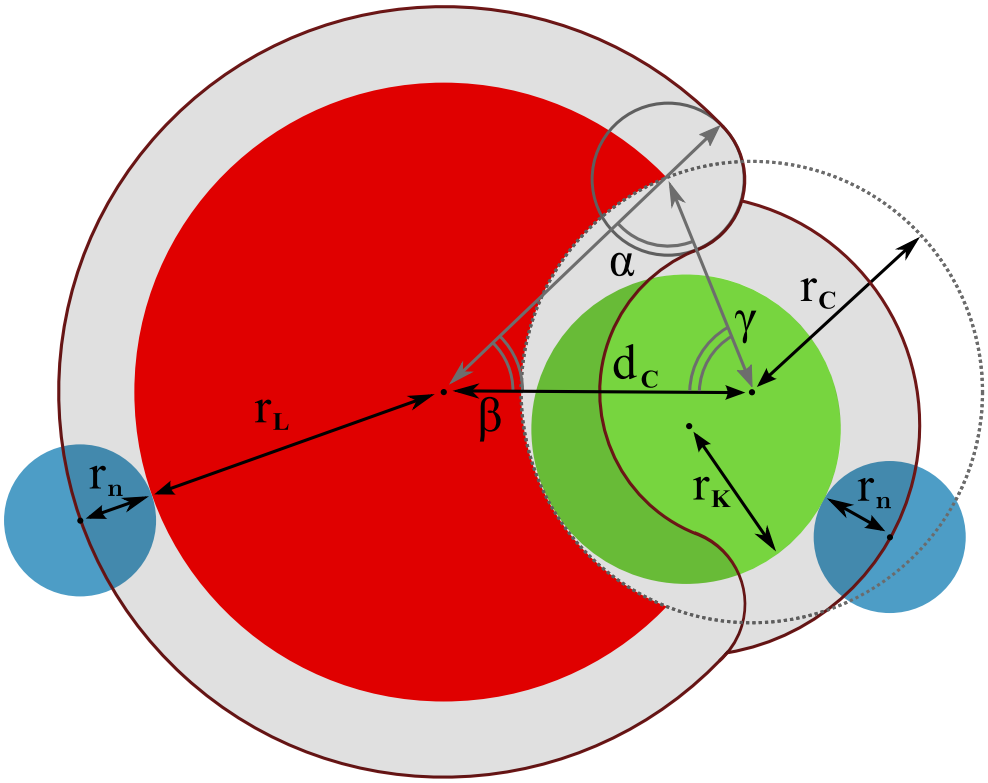

Figure A.2: A geometric argument for three important angles of a lock and key system, used to calculate the volume of the excluded volume, as shown pictorially in fig. 3.4. Note in this picture that $r_{\mathrm{L}} \neq r_{\mathrm{c}} \neq r_{\mathrm{K}} \neq d_{\mathrm{c}}$.

Appendix B

Equilibrium Constant from Partition Function

The chemical equation for a multiple lock key system is given as

$$\mathrm{L} + \mathrm{K} \leftrightharpoons \mathrm{LK}. \tag{B.1}$$

The equilibrium constant for this system is given as

$$\mathcal{K}_{\mathrm{B}} = \frac{\rho_{\mathrm{LK}}}{\rho_{\mathrm{L}}\rho_{\mathrm{K}}} \tag{B.2}$$

where ρ_{LK}, ρ_{L} and ρ_{K} are the number densities of lock-key bound pairs, locks and keys, respectively. We assert that $\mathcal{K}_{\mathrm{B}}$ can be approximated[1] as

$$\mathcal{K}_{\mathrm{B}} \approx \int_0^{r_{\mathrm{B}}} 4\pi r^2 g(r) \mathrm{d}r. \tag{B.3}$$

B.1 Proof

For the following arguments, we are in a dilute system where the box that our lock and key system inhabits is infinitely large, such that there are a vanishingly small number densities of locks and keys. The single key partition function can be written as

$$q_{\mathrm{K}} \equiv \int_V \mathrm{d}^3 r = V, \tag{B.4}$$

where we integrate over all space that our single key can inhabit. It should be clear that this is the volume of the whole system. The single lock partition function can be written as

$$q_{\mathrm{L}} \equiv \int_S \int_V \mathrm{d}^3 r \mathrm{d}^2 \Omega = (4\pi) V, \tag{B.5}$$

[1] Approximate as we have not accounted for overlapping locks or overlapping keys.

where we integrate over all space that our single lock can inhabit, but also over the whole surface that its director can point. It should be clear that the angular integral over a unit sphere is 4π. The two particle bound lock-key pair partition function can be written as

$$q_{\mathrm{LK}} \equiv \int_S \int_{V_\mathrm{B}} \int_V \exp(-\beta W(r_1, r_2)) \mathrm{d}^3 r \mathrm{d}^3 r_1 \mathrm{d}^2\Omega, \tag{B.6}$$

where we integrate over: all space that our lock-pair can inhabit, all space in which the key, denominated as 1, is counted as bound, and over the whole surface in which the director of our lock, denominated by 1, can point. We note that the effective potential, $W(r_1, r_2)$, between the lock and key means that the Boltzmann factor in our partition function no longer evaluates to 0.

For a dilute system, the total partition function of a N-body lock key system, $\mathbb{Q}$, can approximated as

$$\mathbb{Q} \approx \sum_{N_{\mathrm{LK}}} \frac{q_{\mathrm{LK}}^{N_{\mathrm{LK}}} q_{\mathrm{L}}^{N_{\mathrm{L}}} q_{\mathrm{K}}^{N_{\mathrm{K}}}}{N_{\mathrm{LK}}! N_{\mathrm{L}}! N_{\mathrm{K}}!} \tag{B.7}$$

where

$$N_{\mathrm{L}} = N_{\mathrm{L}}^{\mathrm{tot}} - N_{\mathrm{LK}} \tag{B.8}$$

and

$$N_{\mathrm{K}} = N_{\mathrm{K}}^{\mathrm{tot}} - N_{\mathrm{LK}}. \tag{B.9}$$

For each number of lock-key pair states, N_{LK}, we have the independent contributions of partition functions of all distinct states (eq. (B.1)), of which we over-count by a multiple of $N_{\mathrm{LK}}! N_{\mathrm{L}}! N_{\mathrm{K}}!$ due to the locks and keys being indistinguishable. More generally, we can write eq. (B.7) as

$$\mathbb{Q} \approx \sum_{N_{\mathrm{LK}}} \exp[-\beta A(N_{\mathrm{LK}}, N_{\mathrm{L}}, N_{\mathrm{K}})], \tag{B.10}$$

where

$$-\beta A(N_{\mathrm{LK}}, N_{\mathrm{L}}, N_{\mathrm{K}}) = \ln\left(\frac{q_{\mathrm{LK}}^{N_{\mathrm{LK}}} q_{\mathrm{L}}^{N_{\mathrm{L}}} q_{\mathrm{K}}^{N_{\mathrm{K}}}}{N_{\mathrm{LK}}! N_{\mathrm{L}}! N_{\mathrm{K}}!}\right) \tag{B.11}$$

where we recognise that $A(N_{\mathrm{LK}}, N_{\mathrm{L}}, N_{\mathrm{K}})$ is the Helmholtz free energy of the N-body lock and key system. We can minimise A with respect to the number of bound lock-key states, N_{LK}:

$$-\beta\left(\frac{\partial A}{\partial N_{\mathrm{LK}}}\right)_{N_{\mathrm{L}}^{\mathrm{tot}}, N_{\mathrm{K}}^{\mathrm{tot}}} = \ln\left(\frac{q_{\mathrm{LK}}}{q_{\mathrm{L}} q_{\mathrm{K}}}\right) + \ln\left(\frac{N_{\mathrm{L}} N_{\mathrm{K}}}{N_{\mathrm{LK}}}\right) = 0 \tag{B.12}$$

where we have exploited Stirling's approximation[2] to remove any factorials. Finally, we note that the exponential of eq. (B.12) is just a multiple of V away from the definition of the equilibrium constant in eq. (B.2):

$$\frac{q_{\mathrm{LK}}}{q_{\mathrm{L}} q_{\mathrm{K}}} V = \frac{N_{\mathrm{LK}}}{N_{\mathrm{L}} N_{\mathrm{K}}} V = \mathcal{K}_{\mathrm{B}}. \tag{B.13}$$

[2]Valid for a large number of particles

If we substitute the definitions of the single particle and bound lock-key partition into the LHS of eq. (B.13), we find

$$\mathcal{K}_{\mathrm{B}} \approx \frac{\iint_{V_{\mathrm{B}}\,V_{\mathrm{B}}} \exp(-\beta W(r_1, r_2))\mathrm{d}^3 r_1 \mathrm{d}^3 r_2}{\left(\int_V \mathrm{d}^3 r\right)^2} V \tag{B.14}$$

which can be recognised as the integral of the pair distribution function within the bound radial cut off, r_{B}:

$$\mathcal{K}_{\mathrm{B}} \approx \int_0^{r_{\mathrm{B}}} 4\pi r^2 g(r)\mathrm{d}r. \tag{B.15}$$

Appendix C

Constrained Fit

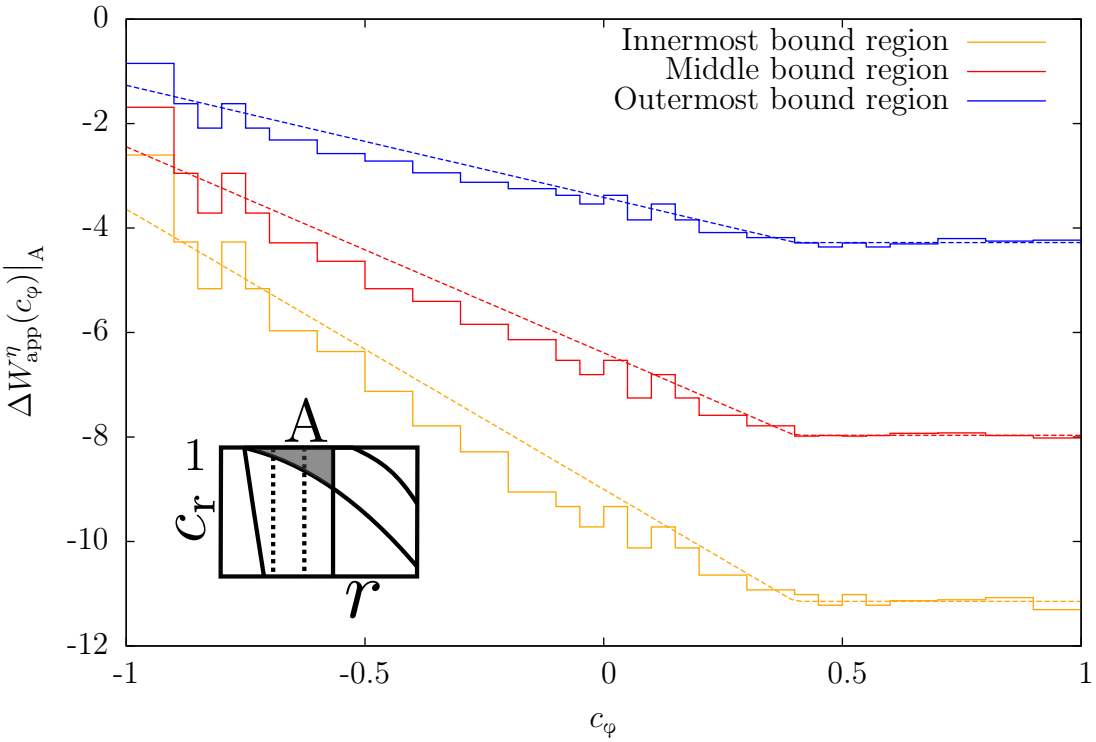

Figure C.1: 1D effective potential from computer simulation for exactly fitting 2 lock system in the bound region, $\Delta W^{\eta}_{\mathrm{app}}(c_\varphi)\big|_{\mathrm{A}}$. From bottom to top, we have the left-most to right most third of the bound region, as shown in the inset image.

One cannot simply perform a line of best fit on the angular $\Delta W^{\eta}_{\mathrm{app}}(c_\varphi)\big|_{\mathrm{A}}$ effective potential data in fig. C.1. One has to ensure that an (adjusted) integrated potential over the whole c_φ range in question, $\Delta W^{\eta}_{\mathrm{app}}\big|_{\mathrm{A}}$, is satisfied after parametrisation. Practically, one needs to ensure that the following expression is satisfied:

$$-\log\left[\frac{\exp\left(\Delta W^{\eta}(c_\varphi)\big|_{\mathrm{An}}\right)\iint\limits_{\mathrm{An}}\mathrm{d}r\mathrm{d}c_{\mathrm{r}}\int\limits_{-1}^{1}\mathrm{d}c_{\mathrm{i}}\mathrm{d}c_\varphi\mathbb{P}^{\eta=0}_{\mathrm{LL}}(r,c_{\mathrm{r}},c_{\mathrm{i}},c_\varphi)}{\iint\limits_{\mathrm{An}}\mathrm{d}r\mathrm{d}c_{\mathrm{r}}\int\limits_{-1}^{1}\mathrm{d}c_{\mathrm{i}}\mathrm{d}c_\varphi\mathbb{P}^{\eta}_{\mathrm{LL}}(r,c_{\mathrm{r}},c_{\mathrm{i}},c_\varphi)}\right]=\Delta W^{\eta}_{\mathrm{app}}\big|_{\mathrm{An}}\qquad(\mathrm{C}.1)$$

where we remember that

$$\Delta W_{\mathrm{A}}^{\eta} = -\log\left[\frac{\iiint\limits_{\mathrm{An}} \mathbb{P}_{\mathrm{LL}}^{\eta}\mathrm{d}r\mathrm{d}c_{\mathrm{r}}\mathrm{d}c_{\mathrm{i}}\mathrm{d}c_{\varphi}}{\iiint\limits_{\mathrm{An}} \mathbb{P}_{\mathrm{LL}}^{\eta=0}\mathrm{d}r\mathrm{d}c_{\mathrm{r}}\mathrm{d}c_{\mathrm{i}}\mathrm{d}c_{\varphi}}\right], \tag{C.2}$$

where the subscript n refers to the particular sub-region, i.e., 1 would refer to the innermost bound region, and $\mathbb{P}_{\mathrm{LL}}^{\eta} = \mathbb{P}_{\mathrm{LL}}^{\eta}(r, c_{\mathrm{r}}, c_{\mathrm{i}}, c_{\varphi})$ etc. for brevity. The lines of best fit in fig. C.1 are represented by $\Delta W^{\eta}(c_{\varphi})\big|_{\mathrm{An}}$ in eq. (C.1). We arrived at eq. (C.1) by considering a rearranged form of eq. (C.2),

$$\exp(\Delta W_{\mathrm{A}}^{\eta}) \iiint\limits_{\mathrm{An}} \mathbb{P}_{\mathrm{LL}}^{\eta=0}\mathrm{d}r\mathrm{d}c_{\mathrm{r}}\mathrm{d}c_{\mathrm{i}}\mathrm{d}c_{\varphi} = \iiint\limits_{\mathrm{An}} \mathbb{P}_{\mathrm{LL}}^{\eta}\mathrm{d}r\mathrm{d}c_{\mathrm{r}}\mathrm{d}c_{\mathrm{i}}\mathrm{d}c_{\varphi}. \tag{C.3}$$

The mathematical form of fig. C.1 can be written as

$$\exp\big(\Delta W^{\eta}(c_{\varphi})\big|_{\mathrm{An}}\big) \iint\limits_{\mathrm{An}} \mathbb{P}_{\mathrm{LL}}^{\eta=0}\mathrm{d}r\mathrm{d}c_{\mathrm{r}}\mathrm{d}c_{\mathrm{i}} = \iint\limits_{\mathrm{An}} \mathbb{P}_{\mathrm{LL}}^{\eta}\mathrm{d}r\mathrm{d}c_{\mathrm{r}}\mathrm{d}c_{\mathrm{i}}, \tag{C.4}$$

from which we can integrate with respect to c_{φ}, equate to eq. (C.3), and rearrange such that

$$\exp\big(-\Delta W_{\mathrm{app}}^{\eta}\big|_{\mathrm{An}}\big) = \frac{\iiint\limits_{\mathrm{An}} \mathbb{P}_{\mathrm{LL}}^{\eta}\mathrm{d}r\mathrm{d}c_{\mathrm{r}}\mathrm{d}c_{\mathrm{i}}\mathrm{d}c_{\varphi}}{\iiint\limits_{\mathrm{An}} \mathbb{P}_{\mathrm{LL}}^{\eta=0}\mathrm{d}r\mathrm{d}c_{\mathrm{r}}\mathrm{d}c_{\mathrm{i}}\mathrm{d}c_{\varphi}}, \tag{C.5}$$

which is just the exponential form of eq. (C.3).

A similar procedure can be performed for any region in fig. 5.3 that has a c_{φ} (or other coordinate) dependence.

Appendix D

Particle Suspended in Fluid with Gravitational Field

The potential difference for a particle at an initial and proposed, arbitrary, height in a fluid can be derived as follows.

A particle, suspended in a fluid may have two forces acting on it: a gravitational force, $\boldsymbol{F}_{\mathrm{g}} = m\boldsymbol{g}$, and a buoyant force exerted by the fluid against the weight of the particle, $\boldsymbol{F}_{\mathrm{b}} = -\rho V_{\mathrm{p}}\boldsymbol{g}$, where ρ is the density of the fluid and V_{p} is the volume displaced by our particle. Finding the net force on our particle is then simply

$$\boldsymbol{F} = g(\rho V_{\mathrm{p}} - m)\hat{\boldsymbol{z}} \tag{D.1}$$

if gravity is acting in the z-direction. At the particle's original position, z_{i}, the net potential energy is simply $E_{\mathrm{i}} = z_{\mathrm{i}}F$. It then follows that the energy potential difference after displacing this particle an arbitrary distance in the z direction is

$$\Delta E = g(\rho V_{\mathrm{p}} - m)(z_{\mathrm{f}} - z_{\mathrm{i}}). \tag{D.2}$$

D.1 Modified Metropolis Criterion

Knowing that the Metropolis criterion for Monte Carlo move acceptance takes the form

$$P_{\mathrm{acc}} = \begin{cases} 1 & \text{if } \Delta E \leq 0 \\ \exp(-\beta\Delta E) & \end{cases}$$

we multiply eq. (D.2) by the inverse thermal energy, β. If we also multiply eq. (D.2) on both sides by β, then

$$\beta\Delta E = \beta g(\rho V_{\mathrm{p}} - m)(z_{\mathrm{f}} - z_{\mathrm{i}}) \tag{D.3}$$

where $G = \beta m_0 g\sigma$ (the strength of gravity), σ is the length scale (or diameter) of a particle and $m_0 = \rho V_{\mathrm{p}} - m$ is a reduced mass. More simply, eq. (D.3) can become

$$\beta\Delta E_{\mathrm{g}}(z_{\mathrm{c}}) = \frac{G\big(z_{\mathrm{c,f}} - z_{\mathrm{c,i}}\big)}{\sigma}. \tag{D.4}$$

Bibliography

[1] D. J. Ashton, R. L. Jack, and N. B. Wilding, "Self-assembly of colloidal polymers via depletion-mediated lock and key binding," Soft Matter **9**, 9661 (2013).

[2] Z. Zhang, A. S. Keys, T. Chen, and S. C. Glotzer, "Self-assembly of patchy particles into diamond structures through molecular mimicry," Langmuir **21**, 11547 (2005).

[3] H. Kaeslin, *Digital Integrated Circuit Design: From VLSI Architectures to CMOS Fabrication* (Cambridge University Press, 2008).

[4] M. Boncheva and G. M. Whitesides, "Making things by self-assembly," MRS Bulletin **30**, 736 (2005).

[5] H. Huff, *Into The Nano Era: Moore's Law Beyond Planar Silicon CMOS*, Springer Series in Materials Science (Springer, 2008).

[6] N. Macias, S. Pandey, A. Deswandikar, C. Kothapalli, C. Yoon, D. Gracias, and C. Teuscher, in *Nanoscale Architectures (NANOARCH), 2013 IEEE/ACM International Symposium on* (2013), pp. 116–121.

[7] P. Fox and P. McSweeney, *Dairy Chemistry and Biochemistry* (Springer, 1998).

[8] M. Naught, A. Wilkinson, M. Nic, J. Jirat, B. Kosata, and A. Jenkins, "IUPAC. compendium of chemical terminology, 2nd ed. (the "Gold Book")," XML on-line corrected version: `http://goldbook.iupac.org` **10** (2006).

[9] R. G. Jones, E. S. Wilks, W. V. Metanomski, J. Kahovec, M. Hess, R. Stepto, and T. Kitayama, *Compendium of Polymer Terminology and Nomenclature, IUPAC Recommendations 2008* (RSC Publishing, 2008).

[10] P. Fox, *Cheese: General aspects*, no. v. 1 in Cheese: Chemistry, Physics and Microbiology. General Aspects (Elsevier, 2004).

[11] B. Derjaguin and L. Landau, "Theory of the stability of strongly charged lyophobic sols and of the adhesion of strongly charged particles in solutions of electrolytes," Acta Physico Chemica URSS **14**, 633 (1941).

[12] E. J. W. Verwey and J. T. G. Overbeek, *Theory of the Stability of Lyophobic Colloids* (Elsevier, 1948).

[13] S. Asakura and F. Oosawa, "On interaction between two bodies immersed in a solution of macromolecules," Journal of Chemical Physics **22**, 1255 (1954).

[14] S. C. Glotzer and M. J. Solomon, "Anisotropy of building blocks and their assembly into complex structures," Nat Mater **6**, 557 (2007).

[15] S. Sacanna, D. J. Pine, and G.-R. Yi, "Engineering shape: the novel geometries of colloidal self-assembly," Soft Matter pp. – (2013).

[16] M. P. Arciniegas, M. R. Kim, J. De Graaf, R. Brescia, S. Marras, K. Miszta, M. Dijkstra, R. van Roij, and L. Manna, "Self-assembly of octapod-shaped colloidal nanocrystals into a hexagonal ballerina network embedded in a thin polymer film," Nano Letters **14**, 1056 (2014).

[17] S. Chen, Z. L. Wang, J. Ballato, S. H. Foulger, and D. L. Carroll, "Monopod, bipod, tripod, and tetrapod gold nanocrystals," Journal of the American Chemical Society **125**, 16186 (2003).

[18] Y. Sun and Y. Xia, "Shape-controlled synthesis of gold and silver nanoparticles," Science **298**, 2176 (2002).

[19] D. Dendukuri, D. C. Pregibon, J. Collins, T. A. Hatton, and P. S. Doyle, "Continuous-flow lithography for high-throughput microparticle synthesis," Nature Materials **5**, 365 (2006).

[20] G.-R. Yi, D. J. Pine, and S. Sacanna, "Recent progress on patchy colloids and their self-assembly," Journal of Physics: Condensed Matter **25**, 193101 (2013).

[21] M. E. Leunissen, R. Dreyfus, F. C. Cheong, D. G. Grier, R. Sha, N. C. Seeman, and P. M. Chaikin, "Switchable self-protected attractions in DNA-functionalized colloids," Nature Materials **8**, 590 (2009).

[22] Y. Wang, Y. Wang, D. R. Breed, V. N. Manoharan, L. Feng, A. D. Hollingsworth, M. Weck, and D. J. Pine, "Colloids with valence and specific directional bonding," Nature **491**, 51 (2012).

[23] Q. Chen, J. K. Whitmer, S. Jiang, S. C. Bae, E. Luijten, and S. Granick, "Supracolloidal reaction kinetics of Janus spheres," Science **331**, 199 (2011).

[24] S. Jiang, Q. Chen, M. Tripathy, E. Luijten, K. S. Schweizer, and S. Granick, "Janus particle synthesis and assembly," Advanced Materials **22**, 1060 (2010).

[25] A. Walther and A. H. E. Müller, "Janus particles: Synthesis, self-assembly, physical properties, and applications," Chemical Reviews **113**, 5194 (2013).

[26] F. Smallenburg, L. Leibler, and F. Sciortino, "Patchy particle model for vitrimers," Physical Review Letters **111**, 188002 (2013).

[27] I. Saika-Voivod, F. Smallenburg, and F. Sciortino, "Understanding tetrahedral liquids through patchy colloids," The Journal of Chemical Physics **139**, 234901 (2013).

[28] A. W. Wilber, J. P. K. Doye, A. A. Louis, E. G. Noya, M. A. Miller, and P. Wong, "Reversible self-assembly of patchy particles into monodisperse icosahedral clusters," The Journal of Chemical Physics **127**, 085106 (2007).

[29] E. Bianchi, G. Doppelbauer, L. Filion, M. Dijkstra, and G. Kahl, "Predicting patchy particle crystals: Variable box shape simulations and evolutionary algorithms," The Journal of Chemical Physics **136**, 214102 (2012).

[30] J. A. Millan, D. Ortiz, G. van Anders, and S. C. Glotzer, "Self-assembly of archimedean tilings with enthalpically and entropically patchy polygons," ACS Nano **8**, 2918 (2014).

[31] L. Manna, D. J. Milliron, A. Meisel, E. C. Scher, and A. P. Alivisatos, "Controlled growth of tetrapod-branched inorganic nanocrystals," Nature Materials **2**, 382 (2003).

[32] P. M. Johnson, C. M. van Kats, and A. van Blaaderen, "Synthesis of colloidal silica dumbbells," Langmuir **21**, 11510 (2005).

[33] V. N. Manoharan, M. T. Elsesser, and D. J. Pine, "Dense packing and symmetry in small clusters of microspheres," Science **301**, 483 (2003).

[34] Yu, S.-S. Chang, C.-L. Lee, and C. R. C. Wang, "Gold nanorods: electrochemical synthesis and optical properties," Journal of Physical Chemistry B **101**, 6661 (1997).

[35] A. Mohraz and M. J. Solomon, "Direct visualization of colloidal rod assembly by confocal microscopy," Langmuir **21**, 5298 (2005).

[36] G. Zhang, D. Wang, and H. Möhwald, "Decoration of microspheres with gold nanodots - giving colloidal spheres valences," Angewandte Chemie International Edition **44**, 7767 (2005).

[37] O. Cayre, V. N. Paunov, and O. D. Velev, "Fabrication of asymmetrically coated colloid particles by microcontact printing techniques," Journal of Materials Chemistry **13**, 2445 (2003).

[38] S. Sacanna, W. T. M. Irvine, P. M. Chaikin, and D. J. Pine, "Lock and key colloids," Nature **464**, 575 (2010).

[39] R. Evans, *Density Functionals in the Theory of Non-Uniform Fluids* (Marcel Dekker, 1992), pp. 85 – 175.

[40] R. Roth, B. Götzelmann, and S. Dietrich, "Depletion forces near curved surfaces," Physical Review Letters **83**, 448 (1999).

[41] A. D. Dinsmore, D. T. Wong, P. Nelson, and A. G. Yodh, "Hard spheres in vesicles: Curvature-induced forces and particle-induced curvature," Physical Review Letters **80**, 409 (1998).

[42] M. Kinoshita and T. Oguni, "Depletion effects on the lock and key steric interactions between macromolecules," Chemical Physics Letters **351**, 79 (2002).

[43] J. S. Rowlinson, "The equation of state of dense systems," Reports on Progress in Physics **28**, 169 (1965).

[44] J. Hansen and I. McDonald, *Theory of Simple Liquids*, Academic Press (Elsevier Academic Press, 2006).

[45] P.-M. König, R. Roth, and S. Dietrich, "Lock and key model system," Europhysics Letters **84**, 68006 (2008).

[46] G. Odriozola, F. Jimenez-Angeles, and M. Lozada-Cassou, "Entropy driven key-lock assembly," Journal of Chemical Physics **129**, 111101 (2008).

[47] G. M. Whitesides and M. Boncheva, "Beyond molecules: self-assembly of mesoscopic and macroscopic components," Proceedings of the National Academy of Sciences **99**, 4769 (2002).

[48] R. L. Jack, M. F. Hagan, and D. Chandler, "Fluctuation-dissipation ratios in the dynamics of self-assembly," Physical Review E: Statistical, Nonlinear, and Soft Matter Physics **76**, 021119 (2007).

[49] D. C. Rapaport, "Role of reversibility in viral capsid growth: a paradigm for self-assembly," Physical Review Letters **101**, 186101 (2008).

[50] S. Whitelam, E. H. Feng, M. F. Hagan, and P. L. Geissler, "The role of collective motion in examples of coarsening and self-assembly," Soft Matter **5**, 1251 (2009).

[51] M. F. Hagan, O. M. Elrad, and R. L. Jack, "Mechanisms of kinetic trapping in self-assembly and phase transformation," The Journal of Chemical Physics **135**, 104115 (2011).

[52] D. Klotsa and R. L. Jack, "Predicting the self-assembly of a model colloidal crystal," Soft Matter **7**, 6294 (2011).

[53] J. Grant, R. L. Jack, and S. Whitelam, "Analyzing mechanisms and microscopic reversibility of self-assembly," Journal of Chemical Physics **135** (2011).

[54] I. Zhang, Ph.D. thesis, University of Bristol (2014).

[55] S. S. Datta, S.-H. Kim, J. Paulose, A. Abbaspourrad, D. R. Nelson, and D. A. Weitz, "Delayed buckling and guided folding of inhomogeneous capsules," Physical Review Letters **109**, 134302 (2012).

[56] S. Ma, J. Thiele, X. Liu, Y. Bai, C. Abell, and W. T. S. Huck, "Fabrication of microgel particles with complex shape via selective polymerization of aqueous two-phase systems," Small **8**, 2356 (2012).

[57] S. J. Ivell, R. P. A. Dullens, S. Sacanna, and D. G. A. L. Aarts, "Emerging structural disorder in a suspension of uniformly dimpled colloidal particles," Soft Matter **9**, 9361 (2013).

[58] E. Newman and G. Barkema, *Monte Carlo Methods in Statistical Physics* (Oxford University Press, USA, 1999).

[59] S. Blundell and K. Blundell, *Concepts in Thermal Physics* (OUP Oxford, 2009).

[60] C. Dress and W. Krauth, "Cluster algorithm for hard spheres and related systems," Journal of Physics A: Mathematical and General **28**, L597 (1995).

[61] B. Alder and T. Wainwright, "Phase transition for a hard sphere system," Journal of Chemical Physics **27**, 1208 (1957).

[62] J. Liu and E. Luijten, "Rejection-free geometric cluster algorithm for complex fluids," Physical Review Letters **92**, 035504 (2004).

[63] U. Wolff, "Collective Monte Carlo updating for spin systems," Physical Review Letters **62**, 361 (1989).

[64] R. H. Swendsen and J.-S. Wang, "Nonuniversal critical dynamics in Monte Carlo simulations," Physical Review Letters **58**, 86 (1987).

[65] J. Liu and E. Luijten, "Generalized geometric cluster algorithm for fluid simulation," Physical Review E: Statistical, Nonlinear, and Soft Matter Physics **71**, 066701 (2005).

[66] D. W. Sinkovits, S. A. Barr, and E. Luijten, "Rejection-free Monte Carlo scheme for anisotropic particles," Journal of Chemical Physics **136**, 144111 (2012).

[67] D. Landau and K. Binder, *A Guide to Monte Carlo Simulations in Statistical Physics* (Cambridge University Press, 2009).

[68] D. J. Ashton, N. B. Wilding, R. Roth, and R. Evans, "Depletion potentials in highly size-asymmetric binary hard-sphere mixtures: Comparison of simulation results with theory," Physical Review E: Statistical, Nonlinear, and Soft Matter Physics **84**, 061136 (2011).

[69] D. J. Ashton and N. B. Wilding, "Three-body effects in complex fluids: virial coefficients from simulation finite-size effects," arXiv:1403.3368v2 (2014).

[70] H. Lekkerkerker and R. Tuinier, *Colloids and the Depletion Interaction*, vol. 833 of *Lecture Notes in Physics* (Springer, 2011).

[71] D. Chandler, *Introduction to Modern Statistical Mechanics* (Oxford University Press, 1987).

[72] M. G. Noro and D. Frenkel, "Extended corresponding-states behavior for particles with variable range attractions," The Journal of Chemical Physics **113**, 2941 (2000).

[73] S. Sacanna, W. T. M. Irvine, L. Rossi, and D. J. Pine, "Lock and key colloids through polymerization-induced buckling of monodisperse silicon oil droplets," Soft Matter **7**, (2011).

[74] F. F. Abraham and Y. Singh, "The structure of a hard-sphere fluid in contact with a soft repulsive wall," The Journal of Chemical Physics **67**, 2384 (1977).

[75] J. E. Jones, "On the determination of molecular fields. II. from the equation of state of a gas," Proceedings of the Royal Society of London. Series A **106**, 463 (1924).

[76] J.-L. Barrat and J.-P. Hansen, *Basic concepts for simple and complex liquids* (Cambridge University Press, 2003).

[77] R. Kimmich, *Principles of Soft-Matter Dynamics: Basic Theories, Non-invasive Methods, Mesoscopic Aspects*, SpringerLink : Bücher (Springer, 2012).

[78] P. Debye, "Polar molecules," Journal of the Society of Chemical Industry **48**, 1036 (1929).

[79] D. R. Nelson and B. Halperin, "Dislocation-mediated melting in two dimensions," Physical Review B **19**, 2457 (1979).

[80] T. Biben, R. Ohnesorge, and H. Löwen, "Crystallization in sedimentation profiles of hard spheres," Europhysics Letters **28**, 665 (1994).

[81] A. Mori, S. ichiro Yanagiya, Y. Suzuki, T. Sawada, and K. Ito, "Crystal structure of hard spheres under gravity by Monte Carlo simulation," Science and Technology of Advanced Materials **7**, 296 (2006).

[82] M. Marechal and M. Dijkstra, "Crystallization of colloidal hard spheres under gravity," Physical Review E: Statistical, Nonlinear, and Soft Matter Physics **75**, 061404 (2007).

[83] U. Gasser, C. Eisenmann, G. Maret, and P. Keim, "Melting of crystals in two dimensions," ChemPhysChem **11**, 963 (2010).

[84] E. P. Bernard and W. Krauth, "Two-step melting in two dimensions: First-order liquid-hexatic transition," Physical Review Letters **107**, 155704 (2011).

[85] D. Frydel and S. A. Rice, "Phase diagram of a quasi-two-dimensional colloid assembly," Physical Review E: Statistical, Nonlinear, and Soft Matter Physics **68**, 061405 (2003).

[86] T. Pöschel and T. Schwager, in *Computational Granular Dynamics* (Springer Berlin Heidelberg, 2005), pp. 135–189.

[87] R. J. Baxter, "Percus-Yevick equation for hard spheres with surface adhesion," The Journal of Chemical Physics **49**, 2770 (1968).

[88] M. A. Miller and D. Frenkel, "Simulating colloids with Baxter's adhesive hard sphere model," Journal of Physics: Condensed Matter **16**, S4901 (2004).

[89] E. P. Bernard, W. Krauth, and D. B. Wilson, "Event-chain Monte Carlo algorithms for hard-sphere systems," Physical Review E: Statistical, Nonlinear, and Soft Matter Physics **80**, 056704 (2009).

[90] J. Harris and H. Stocker, *Handbook of Mathematics and Computational Science* (Springer-Verlag New York, 1998).